UCGE Report
Number 20270

Department of Geomatics Engineering

Tightly Coupled MEMS INS/GPS Integration with INS Aided Receiver Tracking Loops

(URL: http://www.geomatics.ucalgary.ca/research/publications/GradTheses.html)

by

Yong Yang

May 2008

THE UNIVERSITY OF CALGARY

Tightly Coupled MEMS INS/GPS Integration with INS Aided Receiver Tracking Loops

by

Yong Yang

A DISSERTATION

SUBMITTED TO THE FACULTY OF GRADUATE STUDIES

IN PARTIAL FULFILLMENT OF THE REQUIREMENTS

FOR THE DEGREE OF DOCTOR OF PHILOSOPHY

DEPARTMENT OF GEOMATICS ENGINEERING

CALGARY, ALBERTA

May, 2008

Abstract

Global Positioning System (GPS) receiver positioning capabilities are being challenged by increasing requirements on positioning and navigation under environments with GPS attenuated signal. This dissertation focuses on the performance enhancement of MEMS INS/GPS integrated navigation systems in signal-attenuated environments. MEMS INS/GPS tightly coupled integration with INS Doppler aided carrier tracking loops is studied in this dissertation.

Based on an analysis of the conventional carrier tracking loop, carrier tracking capability is enhanced by using INS Doppler aiding. INS aided tracking is implemented by adding INS Doppler estimates to the receiver NCO. To theoretically analyze the performance of aided tracking loop, an INS signal simulator is developed. With helps from the simulator, the analysis concludes that INS aiding can effectively improve a standard GPS receiver tracking performance in weak signals and high dynamics environments.

An EKF based MEMS INS/GPS tight integration scheme is used to control aiding errors from a MEMS based INS to the tracking loop. The tightly coupled INS/GPS can work well under the environment of fewer than four satellites. By using non-holonomic constraints for land vehicle applications, the position accuracy can be improved by around 60%. Furthermore, a novel pseudo-signal generation method is proposed to fulfill one gyro and 2 accelerometers (1G2A) suboptimal INS configuration. The proposed suboptimal INS/GPS tight integration can maintain the system positioning error within

7m, 27m, 38m, or 40m during 30s GPS signal outages, with 3, 2, 1 or 0 satellite(s) in-view, respectively.

With the error control by an EKF with INS/GPS tight scheme, MEMS INS Doppler aiding can achieve an additional $3dB-Hz$ margin for the receiver signal tracking, allowing signals with power as weak as $24dB-Hz$. Furthermore, compared with the conventional tight integration, the position accuracy of the tight INS/GPS integration with aided tracking loops is improved under attenuated signal environments.

Acknowledgements

First of all, I would like to express my appreciation to my supervisor, Dr. Naser El-Sheimy. His valuable supervision and continuous encouragement and support make it possible to accomplish this work.

I am grateful to the members of my examining committee for their efforts in reading through this thesis. I would like to extend my appreciation to members of MMSS group, namely Xiaoji Niu, Sameh Nassar, Chris Goodall, Zainab Syed, Bruce Wright, Priyanka Aggarwal, Dongqing Gu, Mahmoud El-Gizawy, Taher Abbas, for their help in various ways, during my studies. This research was supported in part by the research grants from Natural Science and Engineering Research Council of Canada (NSERC) and Geomatics for Informed Decisions (GEOIDE) Network Centers of Excellence (NCE) to Dr. Naser El-Sheimy.

Table of Contents

Abstract iii

Acknowledgements v

Table of Contents vi

List of Tables x

List of Figures xi

List of Abbreviations and Symbols xv

Chapter 1 Introduction 1

- 1.1 Backgrounds 1
- 1.2 Objectives and Contributions 9
- 1.3 Dissertation Outline 12

Chapter 2 INS Signal Software Simulator 15

- 2.1 Reference Frames 15
- 2.2 Theoretical Principle of the Simulator 19
- 2.3 Inertial Sensor Error Models in the Simulator 26

2.4 Simulator Performance Tests and Analyses 30

2.5 Summary 46

Chapter 3 MEMS Based INS/GPS Tightly Coupled Integration 47

3.1 Overview of INS/GPS Integration 48

3.2 MEMS Inertial Sensors 54

3.3 Discrete-Time EKF 57

3.4 EKF Design for Tight Integration 62

3.4.1 INS Dynamic Error Models 62

3.4.2 INS Doppler Measurement and Pseudorange Measurement 66

3.4.3 State Vector and Observables for EKF 69

3.5 Performance Tests and Analysis 75

3.6 Using Non-holonomic Constraint 80

3.7 Sub-optimal Tightly Coupled 85

3.8 Summary 92

Chapter 4 GPS Receiver Tracking Loop and Its Parameters 94

4.1 GPS Receiver Signal Processing 94

4.1.1 GPS L1 Signals 94

4.1.2 GPS Receiver Technology 96

4.1.3 Front-End 98

4.1.4 IF Signal Processing 99

4.1.5 Navigation Solution 106

4.1.6 Receiver Oscillator 107

4.2 Tracking Loops 109

4.2.1 Accumulation and Dump 109

4.2.2 Discriminator 111

4.2.3 Loop Filter 116

4.3 PLL Performance and Its Parameters 118

4.4 Summary 131

Chapter 5 INS Doppler Aided Receiver Tracking Loop 132

5.1 INS Aided Tracking Loop 132

5.1.1 Implementation of IPLL 132

5.1.2 Effect of INS Doppler Accuracy 136

5.2 EKF based MEMS INS Aided Tracking Loop 140

5.2.1 EKF based IPLL 140

5.2.2 Performance Tests and Analyses.. 142

5.3 Summary... 156

Chapter 6 Conclusions and Recommendations... 157

6.1 Summary... 157

6.2 Conclusions.. 158

6.3 Recommendation for Future Work 160

REFERENCES 162

Dynamics Matrix for INS/GPS Tight Couple EKF 174

INS Direct Aiding – Second Simulation Example... 178

Performance Test of EKF based IPLL – Second Data Period 180

List of Tables

Table 2.1: Mathematical models for various random processes 27

Table 2.2: Error models and parameters in INS simulator.. 29

Table 2.3: Parameters for sensor errors used in MEMS INS simulation 42

Table 3.1: Comparison of characteristics of INS and GPS 49

Table 3.2: Individual errors during 10 GPS signal outage periods 79

Table 3.3: Errors comparison of different numbers of satellites being tracked 80

Table 3.4: Navigation errors and their improvement by using non-holonomic 85

Table 3.5: Errors comparison in 1G2A INS configuration with using non-holonomic 92

Table 4.1: DLL Discriminator...114

Table 4.2: PLL Discriminator 116

Table 4.3: Characteristics of loop filters 117

Table 4.4: Tracking errors of different parameters 131

Table 5.1: Tracking error with different grade INS aiding 140

List of Figures

Figure 2.1: The Earth frame and the navigation frame 17

Figure 2.2: Principle of the Simulator 24

Figure 2.3: Heading error behaviours by using simulated data from the simulator 31

Figure 2.4: Simulated trajectories 32

Figure 2.5: Attitude changes 33

Figure 2.6: Velocities on ENU l-frame 33

Figure 2.7: Signals from simulator with error-free 34

Figure 2.8: INS signals with ARW ($3\deg/\sqrt{hr}$) and VRW ($0.66 m/s/\sqrt{hr}$) 36

Figure 2.9: INS signals with SF errors 37

Figure 2.10: INS signal difference due to SF errors 38

Figure 2.11: INS signals with vibration 39

Figure 2.12: INS signals with vibration – 1s zoomed-in 40

Figure 2.13: INS signals with combined errors 41

Figure 2.14: Field test trajectory 43

Figure 2.15: Comparison of INS signals between simulation and field test 43

Figure 2.16: Simulated trajectory with outage periods 45

Figure 3.1: INS/GPS loosely coupled integration 50

Figure 3.2: INS/GPS tightly coupled integration.. 51

Figure 3.3: INS/GPS deeply coupled integration 53

Figure 3.4: EKF algorithm flow chart 58

Figure 3.5: Field test setup.. 75

Figure 3.6: Vehicle's trajectory and motions 76

Figure 3.7: PVA errors for 2 satellites case... 78

Figure 3.8: Clock errors for 2 satellites case 79

Figure 3.9: PVA errors for 2 satellites case by using non-holonomic constraint............. 83

Figure 3.10: 1G2A sub-optimal INS configuration 86

Figure 3.11: Flow chart of 1G2A INS/GPS using INS pseudo-signals 89

Figure 3.12: PVA errors for 2 satellites case (1G2A, non-holonomic)............................ 91

Figure 4.1: Generic diagram of a software based GPS receiver...................................... 98

Figure 4.2: Downconvert RF to IF and IF to baseband 99

Figure 4.3: Block diagram of tracking Loops.. 103

Figure 4.4: Code mismatch vs. early, prompt, and late correlations...............................113

Figure 4.5: DLL discriminator comparisons...114

Figure 4.6: PLL discriminator comparisons 116

Figure 4.7: Block diagrams of 2nd order loop filter...118

Figure 4.8: Simplified PLL...119

Figure 4.9: Linearized discrete model for a PLL.. 120

Figure 4.10: Simulated trajectories and zoom-in 20s of interest 124

Figure 4.11: Simulated velocities of 20s... 124

Figure 4.12: Calculated reference Doppler shift... 125

Figure 4.13: An example of 2nd order PLL behaviour of the simulation case 126

Figure 4.14: In-phase and quadrature-phase components 127

Figure 4.15: C/N_0 estimation 128

Figure 4.16: PLL lock detector behaviour with strong signal (40dB-Hz) 130

Figure 5.1: Phase errors due to signal strength and clock drift vs. bandwidth 134

Figure 5.2: Restructured NCO in IPLL 134

Figure 5.3: Phase errors vs. C/N_0 and B_n with error-free aiding information............. 135

Figure 5.4: IPLL behaviour of the simulation case 136

Figure 5.5: Aiding Doppler and errors with different grade INSs 139

Figure 5.6: Proposed system configuration of INS/GPS integration with IPLL 141

Figure 5.7: Module comparison of the conventional and INS-aided receivers 142

Figure 5.8: ADI MEMS IMU and NordNav Front-end 143

Figure 5.9: Satellites tracked in the field test 146

Figure 5.10: The signal strength during the test y-axis should C/N 146

Figure 5.11: 20s trajectories and signal strength of interest 147

Figure 5.12: Lock detector output of conventional PLL with $C/N_0 = 26dB - Hz$ 148

Figure 5.13: Aiding Doppler to IPLL 149

Figure 5.14: Outputs of IPLL discriminator and loop filter 150

Figure 5.15: Lock detector output and C/N_0 estimation from IPLL 151

Figure 5.16: Output of IPLL lock detector vs. different signal strength 152

Figure5.17: Output of IPLL lock detector vs. different bandwidth 153

Figure 5.18: Comparison of navigation errors by using PLL and IPLL 154

List of Abbreviations and Symbols

List of Abbreviations

AGPS	Assisted Global Positioning System
AOA	Angle of Arrival
ASIC	Application-Specific Integrated Circuit
ARW	Angular Rate Random Walk
BOC	Binary Offset Carrier
C/A	GPS Coarse/Acquisition code
COH	Coherent
DCM	Direction Cosine Matrix
DLL	Delay Lock Loop
DOD	Department of Defense
DR	Dead Reckoning
DSP	Digital Signal Processor
ECEF	Earth-Centred-Earth-Fixed
EKF	Extended Kalman Filter
ENU	East-North-Up
EU	European Union
FCC	Federal Communications Commission
FE	Front End

FFT	Fast Fourier Transform
FLL	Frequency Lock Loop
GM	Gauss-Markov
GNSS	Global Navigation Satellite System
GPS	Global Positioning System
NCO	Numerically Controlled Oscillator
HSGPS	High Sensitivity GPS
IF	Intermediate Frequency
IMU	Inertial Measurement Unit
INS	Inertial Navigation System
IPLL	INS Doppler Aided Phase Lock Loop
KF	Kalman Filter
LLF	Local Level Frame
LNA	Low Noise Amplifier
LO	Local Oscillator
LOS	Line Of Sight
MEMS	Micro-Electro-Mechanical System
OCXO	Oven Controlled Crystal Oscillator
OSC	OSCillator
PDF	Probability Density Function

PIT	Pre-detection Integration Time
PLL	Phase Lock Loop
PRN	Pseudorandom Noise
P(Y)	GPS Precise (encrypted) code
PSD	Power Spectrum Density
PVA	Position, Velocity and Attitude
RF	Radio Frequency
SNR	Signal to Noise Ratio
SF	Scale Factor
SPS	Standard Positioning Service
TCXO	Temperature Controlled Crystal Oscillator
TDOA	Time Difference of Arrival
3D	Three-Dimension
TOA	Time of Arrival
VRW	Velocity Random Walk
WGS	World Geodetic System

List of Symbols

$\dot{\bullet}$	Time derivative
$\hat{\bullet}$	Estimated or computed values
$\bar{\bullet}$	Mean
δ	Error of
$\delta(\cdot)$	Dirac delta function
$\bullet^{-1}$	Inverse of matrix
$\bullet^{T}$	Transpose of matrix
$\times$	Cross product
$E(\cdot)$	Expectation of
$R(\cdot)$	Cross-correlation function
$\sum(\cdot)$	Summation
A	Heading angle
$\bar{A}$	GPS L1 signal amplitude
B_L	Loop bandwidth (Single-sided)
B_n	Equivalent noise bandwidth of the loop
$\mathbf{b}$	Bias vector
β	Correlation time in the 1st order GM
C	Speed of light
C/N_0	Carrier to noise density ratio

$C(t)$	C/A PRN code
$D(t)$	GPS navigation message
$D(z)$	Loop filter's transfer function in z-domain
δt_u	Receiver clock bias
δt_{ru}	Receiver clock drift
ΔT	Temperature change
$\boldsymbol{\varepsilon}$	Attitude error vector
$\mathbf{e}$	Unit vector along LOS
e	First eccentricity of the ellipsoid
f	Frequency
f_d, f_{dopp}	Doppler frequency
$\mathbf{f}$	Specific force vector
$\mathbf{F}$	Dynamics matrix
ϕ	Phase
φ	Geodetic latitude
$\mathbf{\Phi}$	Transition matrix
$g,\mathbf{g}$	Gravity
$\mathbf{H}$	Design matrix
$H(f)$	Loop transfer function
$H_n(f)$	Loop noise transfer function

h	Geodetic altitude
$\mathbf{I}$	Identity matrix
I	In-phase components
$\mathbf{K}$	Kalman gain matrix
λ	Geodetic longitude
λ_{L1}	Wave length of L1 carrier
M_E	Number of samples per COH accumulation
$\mathbf{n}$	Measurement noise vector
N_0	Noise power density
$\boldsymbol{\omega}$	Angular velocity vector
ω_0	Tracking loop's nature frequency
$\mathbf{\Omega}$	Skew-matrix corresponding to an angular velocity vector
ω_d	Angular Doppler frequency
ω_e	The Earth rotation rate
p	Pitch angle
$\mathbf{P}$	Covariance matrix of state vector
Q	Quadrature-phase component
$\mathbf{Q}$	Covariance matrix of system noise vector
$\mathbf{r}$	Position vector
r	Roll angle

R_N	Prime vertical radius of curvature
R_M	Meridian radius of curvature
$\ddot{R}$	Maximum LOS acceleration
$\mathbf{R}$	Covariance matrix of measurement error vector
$\mathbf{R}_x^y$	Rotation matrix from x-frame to y-frame
ρ	Pseudorange
$s(t)$	Waveform of L1 C/A signal from one satellite
S	Signal power within the bandwidth of B_n
θ_e	Tracking loop's dynamics stress error
θ_A	Allan deviation oscillator phase noise
σ	Standard deviation
T_{COH}	COH accumulation interval
τ	Code delay
$\mathbf{U}$	Output vector of inertial sensor triad
$\mathbf{V}$	Position vector
$\mathbf{w}$	System noise vector
$\mathbf{x}$	State vector
$\mathbf{z}, \mathbf{Z}$	Measurement vector

Chapter 1 Introduction

Many technologies exist in positioning and navigation systems, out of which two are used most commonly (Titterton and Weston, 2004). The first is Inertial Navigation Systems (INS), which are self-contained Dead Reckoning (DR) navigation systems provide dynamic information through direct measurements from an Inertial Measurement Unit (IMU) (Savage, 2000). The GPS that relies on the radio-frequency (RF) signals for positioning has been established as a dominant technology to provide location and navigation capabilities with a high reliability and accuracy (Kaplan, 1996). The INS/GPS integrated system takes advantage of the complementary attributes of both systems to yield a system that outperforms either single system operating alone.

1.1 Backgrounds

The last decade has witness an increasing demand for small-sized and low-cost INS for use in many applications such as aviation, personal navigation, car navigation, and consumer products (Shin, 2005). An INS has the advantage of being independent of external electromagnetic signals, and it can operate in any environment. This allows an INS to provide a continuous navigation position, velocity and attitude (PVA) solution. The performance of an INS is characterized by a time-dependent drift in the accuracy of PVA. The INS suffers from time-dependent error growth which causes a drift in the solution, thus compromising the long term accuracy of the system. The rate at which navigation errors grow over time is governed predominantly by the accuracy of the initial alignment, errors in inertial sensors and the dynamics of the trajectory followed (Titterton and Weston, 2004). Although improved accuracy can be achieved through the use of high quality INS, the high cost and government regulations prevent the wider application of high quality INS in commercial navigation systems.

Recently the progress in micro-electro-mechanical systems (MEMS) technology enables a complete inertial unit to be built on a chip, composed of multiple integrated MEMS accelerometers and gyroscopes (El-Sheimy and Niu, 2007). The characteristics of MEMS, immediate start-up time, low power consumption, light weight and low cost, meet the specifications and requirements needed for commercial applications, such as car navigation. However, due to relative lack of maturity of this technology, the performance of these sensors is limited (Shin, 2005). The performance of current MEMS IMU based INS does not meet the accuracy requirement of many navigation applications (Poh et al., 2002; Ford et al., 2004). It therefore becomes necessary to provide a MEMS based INS with regular updates in order to bound its errors to an acceptable level.

Over the years, the consumer market is being fueled by inexpensive, single-chip GPS receivers, which are being increasingly used in an array of consumer products: cellular phones, personal digital assistants, and security devices for personal possessions ranging from cars to computers (Misra and Enge, 2001). The primary advantage of using GPS includes its availability of absolute navigation information, and the long term accuracy in the solution. Although the current standard GPS technologies have met most positioning requirements for line-of-sight (LOS) navigation, they display limits to fulfill the requirements of continuity and reliability in many situations (Godha, 2006).

The combination of GPS and INS not only offers the accuracy and continuity in the solution, but also enhances the reliability of the system (Rogers, 2000). GPS, when combined with INS, can restrict INS error growth over time, and allows for online estimation of the sensor errors, while the INS can enhance the reliability and integrity of the system (Brenner, 1995). It can bridge the position and velocity estimates when there is no GPS signal reception or can assist GPS receiver operation when GPS signal is degraded. Ultimately, the navigation solution derived from an INS/GPS system is better than either standalone solution. As MEMS INS/GPS systems constitute an increasingly attractive low cost option, it is of significant importance to research their performance.

Typically, three strategies are used for GPS and INS integration, namely loose integration, tight integration, and ultra-tight (or deep) integration. Studies involving low performance MEMS INS which have been conducted over the last few years have mainly concentrated on the loosely coupled integration approach (Shin, 2005; Godha, 2006). Under the conventional definition of tightly coupled, there is no local GPS filter. The only one estimator is to fuse the pseudorange and pseudorange rate measurement from both INS and GPS. Tight integration provides a more accurate solution than loose integration (Petovello, 2003a; Hide, 2003; Brown et al, 2004; Syed et al, 2007). It continues to generate integrated navigation solution even if fewer than four satellites are being tracked. For both loosely and or tightly coupled under the conventional definition, GPS is just used to control the INS error drift. GPS measurement still depends on the GPS signal and the GPS receiver operation. Therefore, these two classes of integrated systems are considered as GPS aided INS.

However, in order to meet the rapidly increasing requirements for GPS applications, the new definition of tight INS/GPS integration appears. In some researchers' description of tight integration, the INS information is fed into the GPS receiver to improve the sensitivity and robustness of GPS signal tracking so as to augment the availability and continuity of GPS (Gebre-Egziabher et al., 2007; Chiou et al, 2004; Gebre-Egziabher, 2003). Such a tight integration scheme can be considered as INS aided GPS.

Various emerging applications require users' location information in challenging environments where typical GPS receivers suffer degraded performance or complete signal outages. The Enhanced 911 (E911) Mandate by Federal Communications Commission (FCC) is one of the most important new applications. It requires the wireless carrier to provide automatic location identification of the emergency caller, based on which the public-safety answering point then dispatches the rescue team (FCC, 2003). Solely cellular-based positioning technology has difficulties providing the level of accuracy required in a cost effective manner. In order to meet the requirements for weak signal positioning in E911, high sensitivity GPS (HSGPS), assisted GPS (AGPS), and cellular network-based solutions which use cellular phone signals, have been developed in recent years (Carver, 2005; Klukas et al., 2004). HSGPS receivers are a class of receivers that display significantly higher acquisition/tracking sensitivity in comparison to standard receivers. Typical HSGPS receivers are designed for weak signal acquisition/tracking using coherent and non-coherent integration, over periods longer than 20 ms in the latter case (Watson, 2005). Due to the squaring processing loss, non-coherent integration for weak signal acquisition/tracking is not as effective as coherent integration (Lachapelle, 2005). As a result, assisted-GPS has been developed to enable the use of long coherent integration by providing the navigation message, timing information, almanac, and approximate position through alternate communications channels. This assistance allows coherent integration intervals longer than 20 ms (Karunanayake et al., 2004). Cellular network based solutions including time of arrival (TOA), time difference of arrival (TDOA) and angle of arrival (AOA) methods are similar to GPS in terms of positioning methodology (Klukas and Fattouche, 1998). The positioning solutions of cellular network-based method are not accurate in both urban canyons and indoor environments due to non-line-of-sight errors (Ma, 2003).

Beyond E911, rising consumers' demands require the enhancement of stand-alone GPS to continuously offer positioning information in environments where the signal is greatly attenuated or severely corrupted by strong interference (Lachapelle 2005; Pany and Eissfeller, 2006; Julien, 2005). The challenge is to acquire and track the attenuated signals under foliage areas, in urban canyons areas, and indoors. The environments in urban canyons are characterized by signal masking, multipath, and echo-only signals due to the presence of skyscrapers and other high-rise buildings (Lachapelle, 2005; Gao, 2007). In these environments, signal attenuation and strong specular reflections constitute various sources of signal degradation. Environmental variables such as height of buildings, reflective characteristics of buildings' walls, orientation of city streets, and construction material used for skyscrapers can attenuate GPS signals by 10-30dB (Gao, 2007). For auto navigation in downtowns, multipath and echo-only signals are the sources of interference. They change quickly and behave randomly due to the movement of vehicles (MacGougan, 2003).

Attenuation and interference degrade the ability of GPS to acquire and track signals effectively. To extend and improve the availability, reliability and accuracy of GPS, innovative receiver algorithms for signal acquisition and tracking are required.

Generally speaking, for positioning purposes, a GPS receiver needs to fulfill several tasks to derive the raw measurements from the GPS RF signals transmitted by the satellites. A GPS receiver must create the pseudorandom noise (PRN) code and carrier frequency plus Doppler frequency using a delay lock loop (DLL) and a phase lock loop (PLL) to track the incoming signals by synchronizing its local carrier and code with the incoming signals (Kaplan, 1996; Lian, 2004). The pseudorange measurement and the carrier phase measurement are from the DLL and the PLL, respectively. Compared with the DLL, the carrier tracking loop is more vulnerable to loss of lock and it is the weaker part in the operation of a GPS receiver because (1) the same LOS motion leads to a larger carrier Doppler variation as opposed to the code timing, and (2) the DLL is usually aided by LOS motion estimate from the carrier tracking loop (Raquet, 2006).

The PLL tracking performance and measurement accuracy are affected by a number of factors, such as signal-to-noise power ratio, Doppler frequency shift, the GPS receiver's jitter caused by vibration, and the Allan deviation (Kaplan, 1996). Among these factors, the thermal noise and Doppler shift are the most predominant and have a large influence on the design of the PLL. It is difficult for a pure (without INS aiding) PLL to continuously maintain signal tracking under weak signals and high dynamic situations. GPS receiver enhancement with external aiding information, namely using Doppler, has been proposed recently to meet positioning and navigation requirements in degraded GPS signal environments (Titterton and Weston, 2004; Gebre-Egziabher et al. 2005). By aiding signal tracking loops in receivers with external INS information, receivers can track incoming weak signals of low power that can't be tracked by standard technologies. In an INS-assisted GPS receiver, external INS information is used to provide receiver dynamics information so as to allow the GPS receiver to track a weaker than normal incoming signal (Petovello et al, 2007; Yang and El-Sheimy, 2006; Pany et al., 2005; Gebre-Egziabher et al., 2005; Babu and Wang, 2005; Soloviev et al., 2004; Beser et al., 2002). Furthermore, even when there are no external aiding sensors available, a similar method derived from external sensor-aided GPS receiver can be used to improve receiver tracking sensitivity. This class of technology regularly is referred to as optimal estimator based GPS receiver (Gustafson et al., 2000; Psiaki and Jung, 2002). In this class of receivers, optimal estimators are used to fuse all channel measurements and then estimate code phase, carrier phase, Doppler shift, rate of change of Doppler shift, data bit sign, etc. The estimator, typical being a Kalman filter, adopts a soft-mode to deal with the bit sign uncertainty and adjusts the bandwidth to minimize the mean square carrier tracking error (Yu, 2006).

The basic concept of the Doppler aiding is to use external Doppler information to adjust the numerically controlled oscillator (NCO) frequency and therefore reduce, or cancel the effect of dynamic stress (Petovello et al, 2003b; Gebre-Egziabher et al, 2003). In an INS aided tracking loop, the NCO is driven not only by the output from loop filter but also by the aiding Doppler information derived from the INS navigation data. The INS derived Doppler removes the LOS dynamics from a receiver's tracking loop so as to keep the GPS signals in lock. An INS-assisted GPS receiver offers the greatest potential for meeting GPS navigation and positioning requirements under attenuated signals. It will provide INS/GPS integrated system with better tracking capability, higher positioning accuracy, and greater availability.

However, due to the inertial sensor errors, the external INS derived Doppler estimates are not always accurate. The disadvantage of INS derived Doppler aided tracking is that the quality of the INS aiding Doppler heavily affects the receiver's tracking capability (Yang and El-Sheimy, 2006; Babu and Wang, 2005). For closed carrier loop operation, the bandwidth of the loop is usually so narrow that the aiding must be very precise with little or no latency.

The topic of INS aided tracking loops is relatively new, especially for low cost MEMS INS aiding. In an unaided GPS receiver, frequency lock loop (FLL) assisted PLL and the Kalman filter based PLL (Psiaki et al., 2002) are mainly used to improve the tracking loop performance. However, under high dynamic situations, the two techniques can not work well due to the measurement accuracy deterioration or the filter divergence (Lian, 2004). Kreye et al. (2000) claimed that an INS with gyro drift of less than $1^0/hr$ is necessary to keep the phase tracking in lock. However, the cost of such INS limits the use of this technique. Soloviev et al. (2004) uses a low cost and small size INS, with gyro in-run bias of $360^0 / hr$ and accelerometer in-run bias of $2mg$, to aid tracking the loops with successful continuous tracking of $15dB - Hz$ GPS signal. Alban et al. (2003) uses an automotive INS and blended GPS/INS solution to aid the tracking loop. In his research, Alban uses the velocity estimate from a loosely couple integration scheme as the aiding source. Because the tracking loop can not discriminate the Doppler shift and the clock frequency drift, the receiver clock frequency has to be calculated by the estimated GPS velocity. A blended GPS/INS for aiding both Doppler and clock error estimates can be found in Chiou's (2005) work in which a tactical-grad INS was recommended to fulfill the external inertial aiding. Gebre-Egziabher et al. (2005) presents a methodology for analyzing the effect of Doppler aiding in terms of phase jitter on the output of the carrier tracking loop.

For aiding with low-cost, low-accuracy MEMS INS, as used in this dissertation, the tightly coupled INS/GPS integration scheme is used to provide the system navigation solutions as well as the controlled MEMS INS Doppler estimates.

1.2 Objectives and Contributions

This dissertation focuses on the enhancement of the INS/GPS navigation system in attenuated GPS signal environments. The aim of this dissertation is to develop, test and analyze the tight INS/GPS integration with INS aided GPS receiver tracking loops. This major objective includes the following research goals:

1. **To develop and verify an INS signal software simulator.** The simulator provides an easy and flexible tool for the research of various INS/GPS integration strategies and algorithms. The concept of INS simulator is also used for the sub-

optimal INS/GPS tightly coupled integration. The simulator is helpful for the investigation of methodologies of INS aided receiver tracking loops.

2. **To develop and test an extended Kalman filter (EKF) based INS/GPS tight integration software.** The tightly coupled INS/GPS uses the pseudorange and Doppler measurements from both GPS and INS. It can continue to provide useful navigation information in situations where fewer than four satellites are visible. The tightly coupled integration filter is also used for the error controls of INS aiding Doppler and the receiver clock drift, both of which are fed into the receiver tracking loops. To minimize the size of the INS so as to be further integrated with GPS on a single chip, a sub-optimal INS configuration with one gyroscope and two accelerometers is developed based on the concept of INS signal simulator, i.e. an inverse process of INS mechanization.
3. **To investigate the GPS receiver tracking loop and its parameters.** Following a review of the process of GPS receiver signal processing, this research examines the PLL behavior in the presence of the main error sources including thermal noise and dynamics stress. The narrower bandwidth is helpful to the reduction of the tracking errors.
4. **To implement the algorithm of INS Doppler aided GPS receiver tracking loop.** INS aided tracking is implemented by adding both INS Doppler and the receiver clock drift estimate to the NCO. The reconstructed NCO is driven by both the output of the loop filter and the aiding information. The INS Doppler aided PLL (IPLL) only needs to track the residual dynamics after aiding. Owing to the removal of the loop’s dynamic stress, the weaker signal can be tracked. The

performance of IPLL not only is associated with its parameters but also heavily depends on the quality of the aiding Doppler from INS. Therefore, for MEMS INS, an EKF based navigation solution is used for INS Doppler error control.

The organization of the dissertation is determined by the nature of these four research goals, and the tasks required to meet these goals, as described in Section 1.3.

The major contributions of this dissertation are given as follows:

- Development of an INS signal software simulator. Compared with using hardware, the simulator is an effective and flexible tool for inertial system related research, such as INS/GPS integration and evaluation of inertial sensors;
- Development of a 23-state EKF based MEMS grade INS/GPS tightly couple integration software, which combines the pseudorange and Doppler measurements from both INS and GPS. Description of the details of INS error model, GPS error model of the INS Doppler calculation and the EKF design;
- Proposing a novel pseudo-signal generation method of the sub-optimal INS configuration for INS/GPS tight integration. The method derives from the inverse process of INS mechanization;
- A detailed analysis of critical parameters involved in GPS receiver tracking loop design for weak signal tracking; Characterization of the benefits and limitations of INS aided receiver tracking loop by using INSs of different qualities under weak signal and high dynamics environments;

- Development and implementation of INS aided receiver carrier tracking algorithm, which minimizes the phase tracking errors under weak signal and/or high dynamics environments.

1.3 Dissertation Outline

This dissertation consists of six chapters.

Chapter 1 presents a short overview of INS, GPS, and the need for their integration. It then addresses the challenges for continuous signal tracking by GPS receivers. To meet these challenges, the dissertation aims to develop, test and analyze the INS/GPS tightly coupled integration with INS aided receiver tracking loops. Next, this chapter presents the methodology and limitations of this topic. Finally, the current research related to INS-aided GPS receivers is discussed and this is followed by the research objectives and research contributions of this dissertation.

Chapter 2 develops and validates a software-based INS signal simulator. The generation of simulated signal of inertial sensors is an inverse process of INS mechanization. The benchmarks of an inertial system, i.e. references frames, are defined firstly. Then, an inverse INS mechanization based on the reference frames is proposed. The INS simulator is a methodical combination of the inverse INS mechanization and various inertial sensor errors applied in the simulator. The concepts of the INS simulator are used in the pseudo-signal generation of the sub-optimal INS configuration for INS/GPS tight integration, presented in Chapter 3. The outputs of INS simulator are also used in Chapter 5 to analyze the performances of unaided PLL and aided PLL by different quality INSs under weak signal environment, respectively.

Chapter 3 starts with an investigation of different integration schemes and an introduction to MEMS-based INS. An INS/GPS tight integration algorithm based on an EKF of 23 states is built, along with the details of the error models of INS and GPS, the mathematical expression of INS pseudorange and Doppler measurements, and the error states and observables for the EKF. Specially, to minimize the size of the INS so as to be integrated with GPS on a signal chip, the integration method of a sub-optimal INS configuration with one heading gyro and two horizontal accelerometers is proposed and tested. The tightly coupled algorithm and the sub-optimal INS configuration are employed in Chapter 5 to implement the INS aided GPS receiver carrier tracking loop.

Chapter 4 investigates the operation of GPS tracking loop and the effects of its parameters on the tracking performance. The beginning of this Chapter describes the GPS receiver signal processing technology with ambition, which involves GPS signals, receiver front-end (FE), acquisition, tracking, measurement derivation, and navigation solution. Throughout the introduction, the received signal flow with mathematical expression from RF to baseband is presented. Then, the Chapter focuses on the operation of GPS receiver tracking loops including accumulator, discriminator, and loop filter. Finally the tracking capabilities of a second order PLL are analyzed.

Chapter 5 discusses the method of INS Doppler aiding PLL. The aiding Doppler error effects and the performance of the aiding by using different quality INSs under weak signal environment are analyzed. An EKF-based INS Doppler aided tracking loop is implemented. The aiding performances are presented and analyzed on both GPS receiver tracking loop level and INS/GPS integrated system navigation solution level.

Chapter 6 summarizes the main conclusions of this dissertation and presents the recommendations for future work.

Chapter 2 INS Signal Software Simulator

This chapter develops and validates a software-based INS signal simulator. The generation of simulated signals of inertial sensors is an inverse process of INS navigation mechanization. Compared with using hardware, using an INS simulator saves time for research work and is flexible when developing new integration algorithms as it does not impose experimental limitations. The correctness and effectiveness of the simulator has been verified not only in theory, but also in practice by comparing the results from the INS simulator to those from a real hardware INS using field test data. Section 2.1 defines the reference frames used in this dissertation. Section 2.2, begins with reviewing the principle of the simulator, and then presents the generation of the error free output of the inertial sensors based on inverse INS mechanization equations. Section 2.3 describes the mathematical models of the inertial sensor errors applied in the simulator. In section 2.4 several examples are given to demonstrate the correctness and effectiveness of the simulator. Concepts and results of the INS simulator generated in this chapter will be used in the sequent chapters.

2.1 Reference Frames

Reference frames are benchmarks in INS related technology. The frames defined in this section will also be used in other parts of this dissertation. Each frame is an orthogonal, right-handed Cartesian coordinate frame or axis set. There are four reference frames (Titterton and Weston, 2004; Shin, 2005) frequently used in this dissertation.

The inertial frame (i-frame) is an ideal frame of reference in which the inertial sensors comply with Sir Isaac Newton's 1st and 2nd laws of motion. However, since it is hard to construct a strict i-frame, a quasi-inertial frame is typically used in practice. This frame has its origin at the center of the Earth and axes which are non-rotating with respect to distant galaxies. Its z-axis is parallel to the spin axis of the Earth; its x-axis points towards to the mean vernal equinox, and its y-axis completes a right-handed orthogonal frame. The vernal equinox is the ascending node between the celestial equator and the ecliptic.

The Earth centered Earth fixed frame (ECEF, abbreviated as e-frame) has its origin at the center of the Earth and axes that are fixed with respect to the Earth with the x-axis pointing toward the mean meridian of Greenwich in the equatorial plane and y-axis perpendicular to the x-axis in the equatorial plane. Its z-axis is parallel to the mean spin axis of the Earth. This dissertation takes the frame defined by World Geodetic System in 1984 (WGS-84) standard as the e-frame. The rotation rate vector of the e-frame with respect to the i-frame projected to the e-frame is given as

$$\boldsymbol{\omega}_{ie}^{e} = \begin{bmatrix} 0 & 0 & \omega_e \end{bmatrix}^T \tag{2.1}$$

where ω_e is the magnitude of the rotation rate of the Earth. For WGS-84 Earth ellipsoid model, ω_e is equal to $15.04108\deg/hr$ (Schwarz and Wei, 2000). The position vector in the e-frame by Cartesian coordinates (x, y, z) can be expressed in terms of the geodetic longitude (λ), latitude (φ) and altitude (h) as follows

$$\begin{bmatrix} x \\ y \\ z \end{bmatrix} = \begin{bmatrix} (R_N + h)\cos\varphi\cos\lambda \\ (R_N + h)\cos\varphi\sin\lambda \\ [R_N(1-e^2) + h]\sin\varphi \end{bmatrix} \tag{2.2}$$

where

e is the first eccentricity of the ellipsoid, and

R_N is the radius of curvature in the prime vertical.

The navigation frame (n-frame) is a local geodetic frame, or local level frame (LLF) which has its origin at the location of the INS. The INS mechanization is implemented on the n-frame. In this dissertation the axes of n-frame align with the directions of the WGS-84 Earth ellipsoid east, north and up, respectively. The east-north-up LLF is typically abbreviated as ENU l-frame. Figure 2.1 shows the relations between the n-frame and the e-frame.

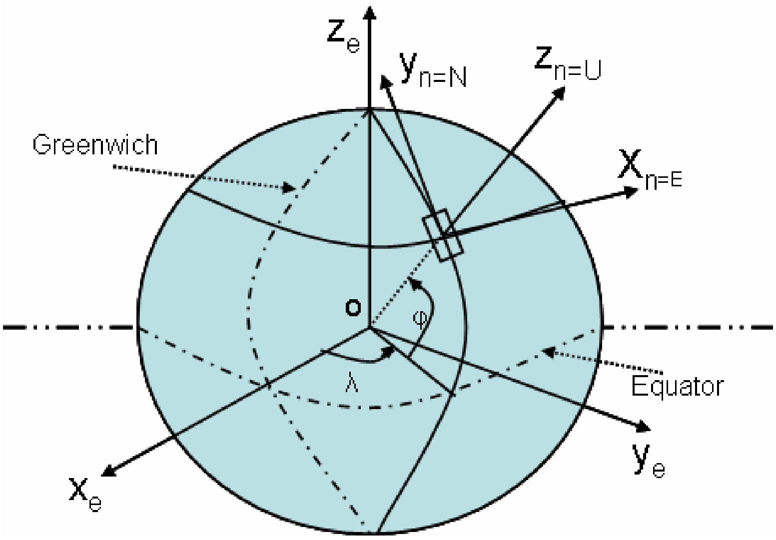

Figure 2.1: The Earth frame and the navigation frame

The transformation from the ENU l-frame to the e-frame can be expressed by a rotation matrix $\mathbf{R}_l^e$ as follows

$$\mathbf{R}_l^e = \begin{bmatrix} -\sin\lambda & -\sin\varphi\cos\lambda & \cos\varphi\cos\lambda \\ \cos\lambda & -\sin\varphi\sin\lambda & \cos\varphi\sin\lambda \\ 0 & \cos\varphi & \sin\varphi \end{bmatrix} \tag{2.3}$$

Therefore, the Earth rotation rate projected in l-frame can be written as

$$\boldsymbol{\omega}_{ie}^{l} = \mathbf{R}_{e}^{l}\boldsymbol{\omega}_{ie}^{e} = \begin{bmatrix} 0 & \omega_e \cos\varphi & \omega_e \sin\varphi \end{bmatrix}^T \tag{2.4}$$

where $\mathbf{R}_{e}^{l} = (\mathbf{R}_{l}^{e})^T$.

The rotation rate of the l-frame with respect to the e-frame is called the transport rate, which can be expressed in terms of the rate of changes of latitude and longitude as (Titterton and Weston, 2004; El-Sheimy, 2006),

$$\boldsymbol{\omega}_{el}^{l} = \begin{bmatrix} -\dot{\varphi} & \dot{\lambda}\cos\varphi & \dot{\lambda}\sin\varphi \end{bmatrix}^T \tag{2.5}$$

The body frame (b-frame) has its origin at the center of the accelerometer triad, which is made coincident with the axes of the vehicle in which the INS is mounted. The x-y-z axes are aligned with the pitch, roll and heading axes of the vehicle, i.e. right-forward-vertical in this dissertation, respectively.

The transformation from the b-frame to the l-frame can be described by a rotation matrix $\mathbf{R}_{b}^{l}$. This rotation matrix can be obtained through an Euler rotation sequence (Savage, 2000), which is associated with the vehicle's attitude (pitch, roll and heading). In this dissertation, the heading angle, pitch angle and roll angle are defined as positive if they are eastward, rightward and upward, respectively. Therefore, the transformation can be carried out as three successive rotations as follows:

Rotate through heading angle (A) about the z axis of the b-frame

$$\mathbf{R}_3(A) = \begin{bmatrix} \cos A & \sin A & 0 \\ -\sin A & \cos A & 0 \\ 0 & 0 & 1 \end{bmatrix} \tag{2.6}$$

Rotate through roll angle (r) about the new y axis of the b-frame

$$\mathbf{R}_2(r) = \begin{bmatrix} \cos r & 0 & \sin r \\ 0 & 1 & 0 \\ -\sin r & 0 & \cos r \end{bmatrix} \tag{2.7}$$

Rotate through pitch angle (p) about the new x axis of the b-frame

$$\mathbf{R}_1(p) = \begin{bmatrix} 1 & 0 & 0 \\ 0 & \cos p & -\sin p \\ 0 & \sin p & \cos p \end{bmatrix} \tag{2.8}$$

$$\mathbf{R}_b^l = \mathbf{R}_3(A)\mathbf{R}_2(r)\mathbf{R}_1(p)$$

$$= \begin{bmatrix} \cos A \cos r + \sin A \sin p \sin r & \sin A \cos p & \cos A \sin r - \sin A \sin p \cos r \\ -\sin A \cos r + \cos A \sin p \sin r & \cos A \cos p & -\sin A \sin r - \cos A \sin p \cos r \\ -\cos p \sin r & \sin p & \cos p \cos r \end{bmatrix} \tag{2.9}$$

$\mathbf{R}_b^l$ is typically named the direction cosine matrix (DCM) or strap-down matrix in the strap-down inertial navigation system. The DCM plays an important role in the implementation of either INS mechanization or the inverse process of mechanization, which is used in the simulator.

2.2 Theoretical Principle of the Simulator

Given the ability to measure the acceleration by accelerometers, it would be possible to calculate the change in velocity and position by performing successive mathematical integrations with respect to time. Meanwhile, in order to navigate with respect to the inertial reference frame, it is necessary to keep track of the direction in which the accelerometers are pointing. Rotational motion of the body with respect to the inertial reference frame is sensed using gyroscopes which determine the orientation of the accelerometers at all times (Titterton and Weston, 2004). Hence, by combining these two sets of measurements, it is possible to define the translational and rotational motions of the vehicle within an inertial reference frame. The above position, velocity and attitude calculation are possible using a specific navigation integration algorithm, called mechanization equations, by using only the signals from the inertial gyroscopes and accelerometers. The INS mechanization equations in the ENU l-frame are given directly as follows (El-Sheimy, 2006).

Position mechanization

$$\dot{\mathbf{r}}^l = \begin{bmatrix} \dot{\varphi} \\ \dot{\lambda} \\ \dot{h} \end{bmatrix} = \mathbf{D}^{-1}\mathbf{V}^l \tag{2.10}$$

Velocity mechanization

$$\dot{\mathbf{V}}^l = \mathbf{R}_b^l \mathbf{f}_{ib}^b - (2\mathbf{\Omega}_{ie}^l + \mathbf{\Omega}_{el}^l)\mathbf{V}^l + \mathbf{g}^l \tag{2.11}$$

Attitude mechanization

$$\dot{\mathbf{R}}_b^l = \mathbf{R}_b^l (\mathbf{\Omega}_{ib}^b - \mathbf{\Omega}_{ie}^b - \mathbf{\Omega}_{el}^b) \tag{2.12}$$

In above equations,

$$\mathbf{D}^{-1} = \begin{bmatrix} 0 & 1/[(R_N + h)\cos\varphi] & 0 \\ 1/(R_M + h) & 0 & 0 \\ 0 & 0 & 1 \end{bmatrix} \tag{2.13}$$

where,

R_M is the meridian radius of the curvature;

$\mathbf{V}^l$	is the vehicle's velocity vector in the l-frame. According to the definition of the l-frame, this velocity can be expressed by three components along the east direction V^E, north direction V^N, and up direction V^U, as $\mathbf{V}^l = \begin{bmatrix} V^E & V^N & V^U \end{bmatrix}^T$;
$\mathbf{f}_{ib}^b$	represents the specific force vector along the three axes of the body frame, which is measured by the accelerometer triad. The notation of $\mathbf{f}_{ib}^b$ means the specific force on the b-frame with respect to the i-frame as observed in the b-frame;
$\mathbf{g}^l$	is the Earth's local gravity vector, which is written as $\mathbf{g}^l = \begin{bmatrix} 0 & 0 & -g \end{bmatrix}^T$, where g is obtained from the well-known normal gravity model (Schwarz and Wei, 2000), $g = a_1(1 + a_2 \sin^2 \varphi + a_3 \sin^4 \varphi) + (a_4 + a_5 \sin^2 \varphi)h + a_6 h^2$ and a_1 to a_6 are constant values, referred to El-Sheimy (2006) for details;
$\mathbf{\Omega}$	denotes a skew-symmetric matrix corresponding to an angular velocity vector $\boldsymbol{\omega}$; $\mathbf{\Omega} = \begin{bmatrix} 0 & -\omega_z & \omega_y \\ \omega_z & 0 & -\omega_x \\ -\omega_y & \omega_x & 0 \end{bmatrix}$ if $\boldsymbol{\omega} = \begin{bmatrix} \omega_x & \omega_y & \omega_z \end{bmatrix}^T$.
$\boldsymbol{\omega}_{ie}^l$	is the Earth rotation rate projected on the l-frame, which is given in equation (2.4);
$\boldsymbol{\omega}_{el}^l$	is the transport rate, which refers to the change of orientation of the l-frame with respect to the Earth. Its expression is shown in

Equation (2.5), which can be further written as a function of velocity on the l-frame, position and the Earth's reference ellipsoid as

$$\boldsymbol{\omega}_{el}^{l} = \begin{bmatrix} -\frac{V^{N}}{R_{M}+h} & \frac{V^{E}}{R_{N}+h} & \frac{V^{E}\tan\varphi}{R_{N}+h} \end{bmatrix}^{T} \qquad (2.14);$$

$\boldsymbol{\omega}_{ib}^{b}$ represents the angular rate vector along the three axes of the body frame, which is measured by the gyroscope triad;

$\boldsymbol{\omega}_{ie}^{b}$ is equal to $\mathbf{R}_{l}^{b}\boldsymbol{\omega}_{ie}^{l}$, where $\mathbf{R}_{l}^{b} = (\mathbf{R}_{b}^{l})^{T}$;

$\boldsymbol{\omega}_{el}^{b}$ is equal to $\mathbf{R}_{l}^{b}\boldsymbol{\omega}_{el}^{l}$.

Generally speaking, the principle of an INS simulator is an inverse process of INS mechanization. Inertial sensor outputs can be derived from the vehicle's PVA information which is obtained from real test data or through a user's design. Although the implementation of the simulator herein is based on a strapdown inertial system with the configuration of three gyros and three accelerometers, the proposed simulation method is instructive for pseudo-signal generation of a suboptimal INS configuration in very low-cost INS based integrated navigation systems, as will be presented in Chapter 3.

The implementation process of the simulator is to apply Newton's 1st and 2nd laws of motion in the i-frame in order to generate the INS inertial sensor measurements in the b-frame by means of an inverse INS mechanization and by combining external parameters, such as the Earth rotation rate, normal gravity and the vehicle's initial PVA information.

The main function of the INS simulator is to generate the raw measurements of any grade of INS such as navigation grade, tactical grade, and consumer grade systems according to a user-given application (such as airborne, land, drilling, pipeline geo-pig applications, etc.). It can simulate a variety of sensor errors such as the bias instability, random walk, scale factor errors, sensor errors due to thermal drift, g-sensitivity, non-orthogonalities, misalignment, and their combinations (Yang and El-Sheimy, 2007).

Both user designed vehicle trajectories and injected external trajectories are acceptable in the simulator. The simulator can generate raw measurements based on user defined vehicle dynamics, such as straight lines, accelerations, turns, U-turns, surface disturbances, constant velocities, static periods as well as varying attitudes, and their combinations. It accepts external vehicle dynamics input from a real world test to generate INS data as well. The simulator can also simulate different motion dynamics of the vehicle in the e-frame.

The conceptual principle of the simulator is shown in Figure 2.2. Differentiation of the position and velocity information derives the acceleration when gravity is added. However, such acceleration is only a transitory quantity on the navigation frame with respect to the inertial frame. Frame rotation information is necessary to transform the acceleration to the body frame, in which the accelerometers measure the vehicle's translational motions with respect to the inertial frame. Frame rotation can be computed from the attitude when the Earth rotation is combined. Frame rotation information indirectly provides the vehicle's rotational motions on the body frame with respect to the inertial frame, which are measured by gyroscopes. Translational and rotational motions plus various sensor errors form the inertial sensor outputs form the inertial sensor outputs form the inertial sensor outputs.

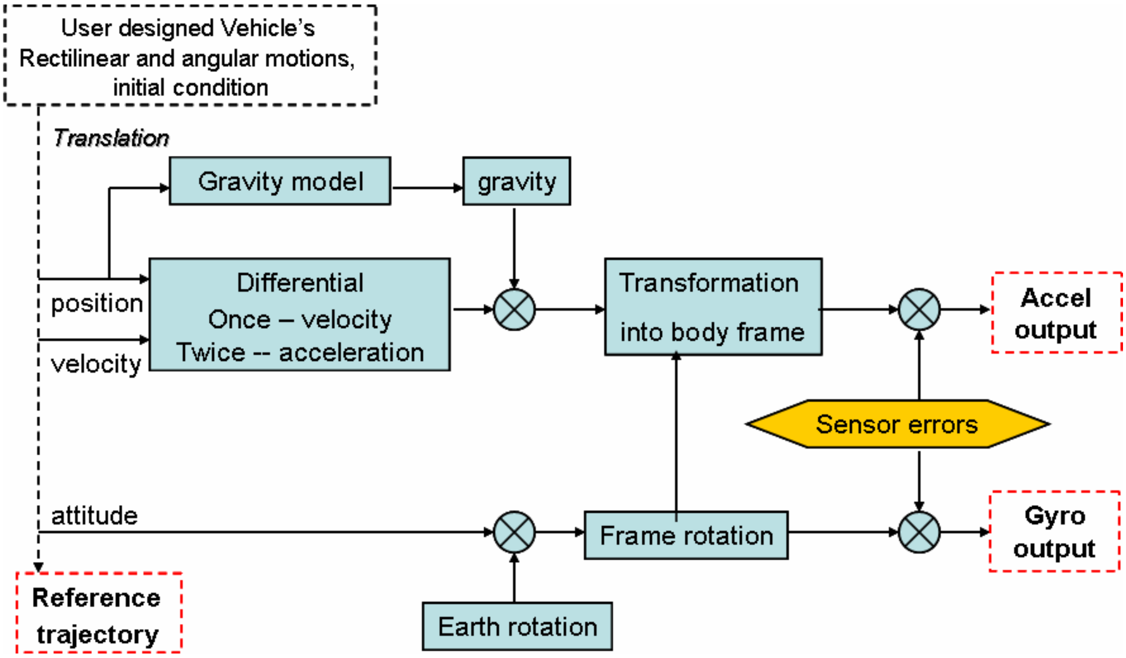

Figure 2.2: Principle of the Simulator

Applying the INS velocity l-frame mechanization equation (2.11) and considering an inverse process in simulation reveal the following,

$$\mathbf{f}_{ib}^{b} = \mathbf{R}_{l}^{b}[\dot{\mathbf{V}}^{l} + (2\boldsymbol{\omega}_{ie}^{l} + \boldsymbol{\omega}_{el}^{l}) \times \mathbf{V}^{l} - \mathbf{g}^{l}] + \delta\mathbf{f}_{ib}^{b} \tag{2.15}$$

In the implementation of the simulator through equation (2.15), if the PVA is from the injected information, $\mathbf{V}^{l}$ is one of the directly injected inputs or can be acquired through a single differentiation of position (as depicted in equation (2.16)),

$$\mathbf{V}^{l} = \frac{Position_{next} - Position_{current}}{time\ \ \mathrm{int}\,erval} \tag{2.16}$$

Alternatively, if the inputs to the simulator are the user designed trajectory and motions, $\mathbf{V}^l$ can be calculated by

$$\mathbf{V}^l = \mathbf{R}_b^l \mathbf{V}^b = \mathbf{R}_b^l \begin{bmatrix} 0 \\ V \\ 0 \end{bmatrix} = \begin{bmatrix} V\cos p \sin A \\ V\cos p \cos A \\ V\sin p \end{bmatrix} \tag{2.17}$$

where V is the user designed vehicle's forward speed during one motion, which is determined by the initial forward speed V_0, the acceleration $\dot{V}$ and time interval t during this motion period. V_0, $\dot{V}$ and t are all user designed parameters.

$$V = V_0 + \dot{V} \cdot t \tag{2.18}$$

In equation (2.15), $\dot{\mathbf{V}}^l$ is the vehicle's acceleration on the l-frame, which is the first difference of the velocity in the l-frame. It can be calculated through a double differentiation of position or single differentiation of velocity

$$\dot{\mathbf{V}}^l = \frac{Velocity_{next} - Velocity_{current}}{time\ \text{int}\,erval} \tag{2.19}$$

or alternatively, through the following equation

$$\dot{\mathbf{V}}^l = \frac{d}{dt}\begin{bmatrix} V\cos p \sin A \\ V\cos p \cos A \\ V\sin p \end{bmatrix} = \begin{bmatrix} \dot{V}\cos p \sin A - \dot{p}V\sin p \sin A + \dot{A}V\cos p \cos A \\ \dot{V}\cos p \cos A - \dot{p}V\sin p \cos A - \dot{A}V\cos p \sin A \\ \dot{V}\sin p + \dot{p}\cos p \end{bmatrix} \tag{2.20}$$

where $\dot{p}$ and $\dot{A}$ are pitch angle change rate and heading angle change rate, respectively, both of which are user-designed parameters. In equation (2.15), $\delta \mathbf{f}_{ib}^b$ represents the accelerometer errors. The errors depend on the error model assumptions, which will be discussed in the next section.

Applying the INS attitude l-frame mechanization equation (2.12) and considering an inverse process in simulation, the output of the gyroscope triad from the simulator $\boldsymbol{\omega}_{ib}^{b}$ can be written as

$$\boldsymbol{\omega}_{ib}^{b} = \mathbf{R}_{l}^{b}(\boldsymbol{\omega}_{ie}^{l} + \boldsymbol{\omega}_{el}^{l}) + \boldsymbol{\omega}_{lb}^{b} + \delta\boldsymbol{\omega}_{ib}^{b} \tag{2.21}$$

where,

$\delta\boldsymbol{\omega}_{ib}^{b}$ represents the gyroscope errors, and

$\boldsymbol{\omega}_{lb}^{b}$ is the mathematical gimbals' rate for a strap-down inertial system, which has components related to the vehicle's attitude and attitude change rate (Titterton and Weston, 2004).

$$\boldsymbol{\omega}_{lb}^{b} = \begin{bmatrix} 0 \\ \dot{r} \\ 0 \end{bmatrix} + \mathbf{R}_{2}^{T}(r)\begin{bmatrix} \dot{p} \\ 0 \\ 0 \end{bmatrix} + \mathbf{R}_{2}^{T}(r)\mathbf{R}_{1}^{T}(p)\begin{bmatrix} 0 \\ 0 \\ \dot{A} \end{bmatrix}$$

i.e.

$$\boldsymbol{\omega}_{lb}^{b} = \begin{bmatrix} \cos r & 0 & \cos p \sin r \\ 0 & 1 & \sin p \\ \sin r & 0 & \cos p \cos r \end{bmatrix}\begin{bmatrix} \dot{p} \\ \dot{r} \\ \dot{A} \end{bmatrix} \tag{2.22}$$

Equations (2.15) and (2.21) show that the inertial sensor outputs consist of two parts: error-free values and sensor errors than are then added to the error free values.

2.3 Inertial Sensor Error Models in the Simulator

The INS simulator can simulate inertial sensor errors both on an individual basis and as a combination to analyze multiple error effects. Inertial sensor errors are generally divided into two parts: deterministic and stochastic (El-Sheimy, 2006). For a high-grade INS, the manufacturer typically calibrates the INS extensively and stores the compensation parameters inside the INS processor and therefore only small random errors remain. For a low performance INS, like the MEMS based INS, there are many additional error sources. This section uses a MEMS grade INS as an example to describe many of the sensor errors modeled in the simulator. For a MEMS inertial sensor, the deterministic part of the errors includes bias offset, scale factor (SF) error, gyro g-sensitivity, non-orthogonality, and SF non-linearity which can be roughly estimated by lab calibrations or manufacturer specifications (Titterton and Weston, 2004; El-Sheimy, 2006; Yang et al, 2007). These errors should be compensated before the INS data are used in the mechanization algorithms. The stochastic part of MEMS inertial sensor errors includes angular random walk (ARW), velocity random walk (VRW), SF changes due to temperature and short term instabilities of the sensors errors. The random constant, the random walk and the first-order Gauss-Markov models are typically used in modeling the inertial sensor errors (Shin, 2005). These random models (Gelb, 1974; Brown and Hwang, 1997) are described in Table 2.1.

Table 2.1: Mathematical models for various random processes

Random process $x(t)$	Continues-time equation	Discrete-time equation	Parameters
Random constant	$\dot{x}(t) = 0$	$x_{k+1} = x_k$	none
Random walk	$\dot{x}(t) = w(t)$	$x_{k+1} = x_k + w_k$	w_k driving white noise
1st order Gauss-Markov	$\dot{x}(t) = -\frac{1}{\beta} x(t) + w(t)$	$x_{k+1} = e^{\frac{\Delta t_{k+1}}{\beta}} x_x + w_k$	w_k driving white noise β correlation time Δt_{k+1} time interval

For a general case, the output of a gyro $\mathbf{U}_g$ and accelerometer $\mathbf{U}_a$ can be modeled as follows, respectively,

$$\mathbf{U}_g = (\mathbf{I} + \mathbf{S}_{gL} + \mathbf{S}_{gLC} \cdot \Delta T)\boldsymbol{\omega} + \mathbf{S}_{gNL}\boldsymbol{\omega}^2 + \mathbf{N}_g\boldsymbol{\omega} + \mathbf{b}_g + \mathbf{b}_{gM} + \mathbf{b}_{gC} + \mathbf{N}_{gG}\mathbf{f} + \mathbf{n}_g \qquad (2.23)$$

$$\mathbf{U}_a = (\mathbf{I} + \mathbf{S}_{aL} + \mathbf{S}_{aLC} \cdot \Delta T)\mathbf{f} + \mathbf{S}_{aNL}\mathbf{f}^2 + \mathbf{N}_a\mathbf{f} + \mathbf{b}_a + \mathbf{b}_{aM} + \mathbf{b}_{aC} + \mathbf{n}_a \qquad (2.24)$$

where,

g (the subscript)	represents the gyro related parameters;
a (the subscript)	represents accelerometer related parameters;
$\mathbf{f}$	is the error-free accelerometer outputs which is calculated based on the equation (2.15). $\mathbf{f}$ is denoted as $\mathbf{f}_{ib}^b$ in that equation;
$\boldsymbol{\omega}$	is the error-free gyro outputs which is calculated based on the equation (2.21). $\boldsymbol{\omega}$ is denoted as $\boldsymbol{\omega}_{ib}^b$ in that equation;
$\mathbf{S}_L$	represents the SF linear error vector along three axes caused by imperfect manufacturing;
$\mathbf{S}_{LC}$	represents the SF linear error vector along three axes caused by the environment temperature change during INS operation;
$\mathbf{S}_{NL}$	represents the SF non-linear error vector along three axes caused by the environment temperature change during INS operation;
ΔT	is the temperature change of the environment during INS operation;
$\mathbf{N}$	is a matrix with random Gaussian distributed components representing the nonorthogonality of the sensor triad;

$\mathbf{N}_g$ is the gyro g-sensitivity matrix with random Gauss distributed components;

$\mathbf{b}$ is the inertial sensor's turn-on bias;

$\mathbf{b}_M$ is the bias in-run instability;

$\mathbf{b}_C$ is the bias due to thermal drift;

$\mathbf{n}$ is the white noise which drives the ARW or VRW.

According to equations (2.23) and (2.24), the IMUS can simulate a variety of inertial sensor errors. Table 2.2 summarizes the error models implemented in the IMUS.

Table 2.2: Error models and parameters in INS simulator

Error	Model	Parameters and Unit	
b_g	random constant		$--\deg/hr$
b_{gM}	1st Gauss-Markov	standard deviation $(1-\sigma)$	$--\deg/hr$
		correlation time	$--hr$
n_g	white noise	ARW spectral density	$--\deg/\sqrt{hr}$
		bandwidth	$--Hz$
b_a	random constant		$--\mu g$
b_{aM}	1st Gauss-Markov	$1-\sigma$	$--\mu g$
		correlation time	$--hr$
n_a	white noise	VRW spectral density	$--m/s/\sqrt{hr}$
		bandwidth	$--Hz$
ΔT	1st Gauss-Markov	$6-\sigma$	$--{}^0C$
		correlation time	$--hr$
S_{gL}	Constant		$--ppm$
S_{gLC}	Constant		$--ppm/{}^0C$
S_{gNL}	Constant	best fit straight line	$--ppm$
		measurement full scale	$--\deg/s$
b_{gC}	Constant		$--\deg/s/{}^0C$

Table 2.2: Error models and parameters in INS simulator (cont.)

Error	Model	Parameters and Unit	
$\mathbf{N}_g$	random constant	$1-\sigma$ of matrix	$--rad$
$\mathbf{N}_{gG}$	random constant	$1-\sigma$ of matrix	$--\deg/hr/g$
S_{aL}	Constant		$--ppm$
S_{aLC}	Constant		$--ppm/{}^0C$
S_{aNL}	Constant	best fit straight line	$--ppm$
		measurement full scale	$--g$
b_{aC}	Constant		$--\mu g/{}^0C$
N_a	random constant	$1-\sigma$ of matrix	$--rad$

2.4 Simulator Performance Tests and Analyses

The correctness and efficiency of the simulator were verified at four levels. First, the basic principles of the simulator were verified by comparing against standard INS mechanization. Second, the individual inertial sensor errors and their combinations were verified. Third, the simulated signals were compared with real hardware INS signals collected in a field test.

Furthermore, in most civil applications, an INS is often integrated with GPS to provide both long and short-term navigation accuracy. Integrated INS/GPS systems provide an enhanced navigation solution that has superior performance in comparison to either standalone system. To work for the inertial based integrated navigation system, the optional GPS signals (position/velocity information with lever arm), odometer signals, and magnetic heading signals are also simulated. Beyond the raw signal level verifications in both theory and practice, the correctness of the INS simulator is also validated at the INS/GPS integration level. In the fourth level test, both simulated signals and the real hardware signals were processed through AINS® tool box (Shin and El-

Sheimy, 2002) to check the simulator performance. This software package processes the aided inertial navigation system using INS/GPS data in a loosely coupled architecture.

I. Principle level verification

To verify the correctness of the simulator, an INS data set for a static case was simulated and sent into INS mechanization. Since the simulation is an inverse process of mechanization, the navigation error propagation should be the same as the INS behaviour when the simulated data are sent to INS mechanization. The most typical behaviour of an INS is that the distribution of the navigation errors should include the Schuler period (84.4 min), Foucault period (34hr) and Earth's rotation rate (24hr) (Titterton and Weston, 2004). Figure 2.3 is an example of the heading error of navigation over 45 hours with a gyro bias of $0.01^0 / hr$ under a static environment using simulated data.

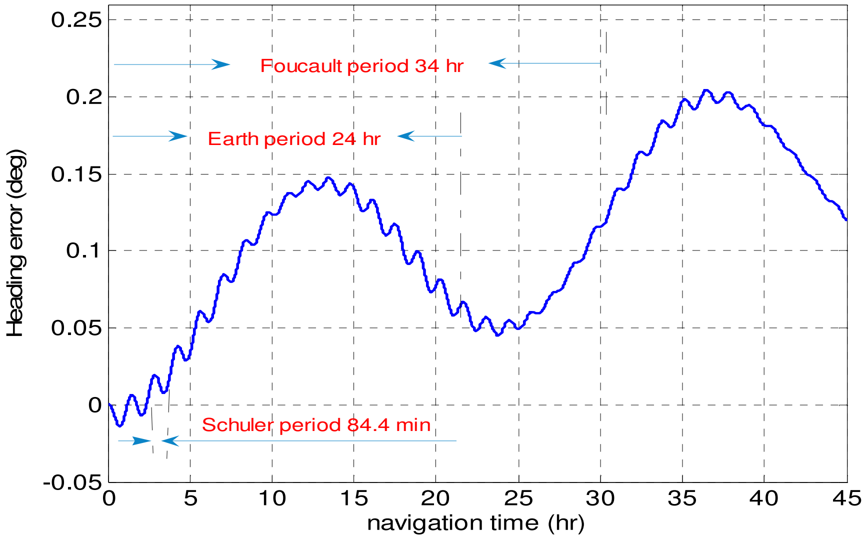

Figure 2.3: Heading error behaviours by using simulated data from the simulator

There are three periods clearly shown in the Figure 2.3. They have the correct periods as expected. These three periods are very basic characteristics for any inertial system, which indicates the correct operation of the basic principles of the simulator.

II. Individual errors and their combinations

To complete the verification of the individual errors and their combinations from the simulator, a set of vehicle trajectories and motions was designed. The designed data set involved over 4400 seconds and included most of the vehicle's dynamics, such as accelerations, decelerations, static periods, turns, U-turns, tilts, and so on, as show in Figures 2.4 to 2.6.

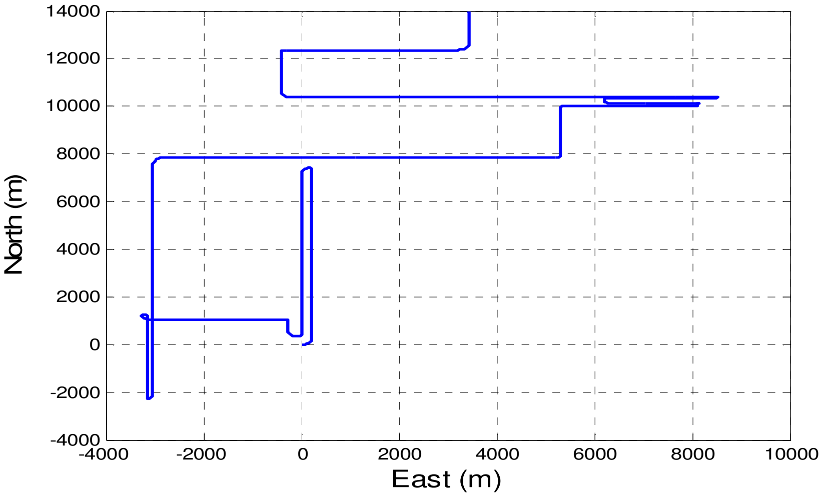

Figure 2.4: Simulated trajectories

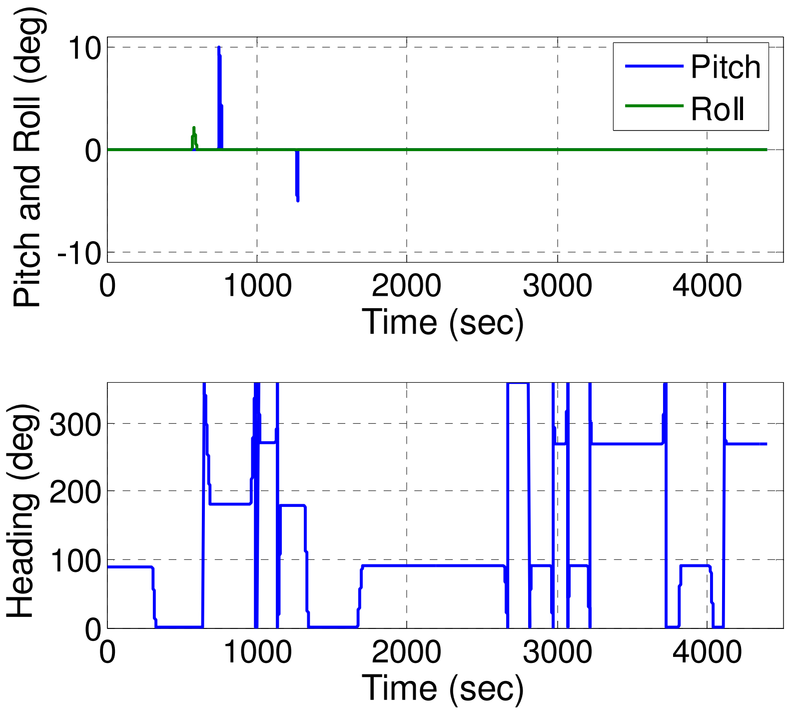

Figure 2.5: Attitude changes

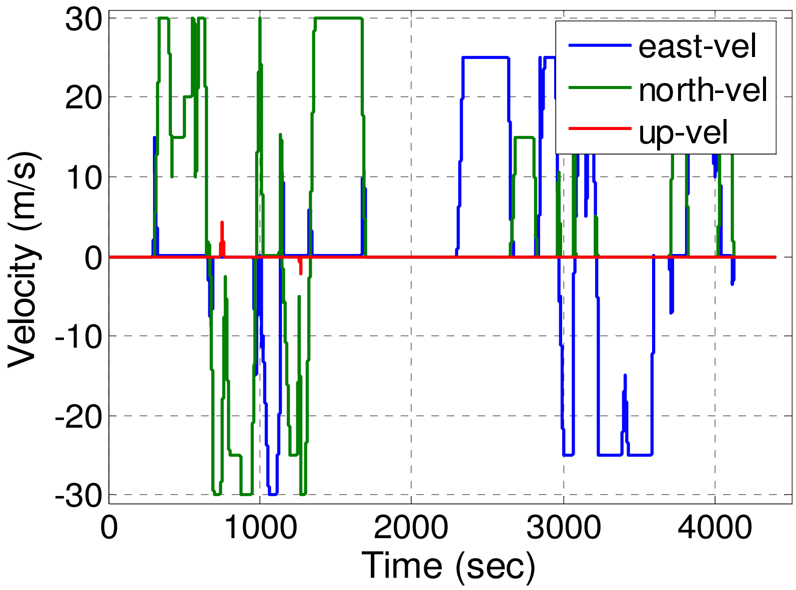

Figure 2.6: Velocities on ENU l-frame

Figure 2.7 shows of the error-free outputs of the inertial sensors (gyro and accelerometer) based on the above vehicle motions.

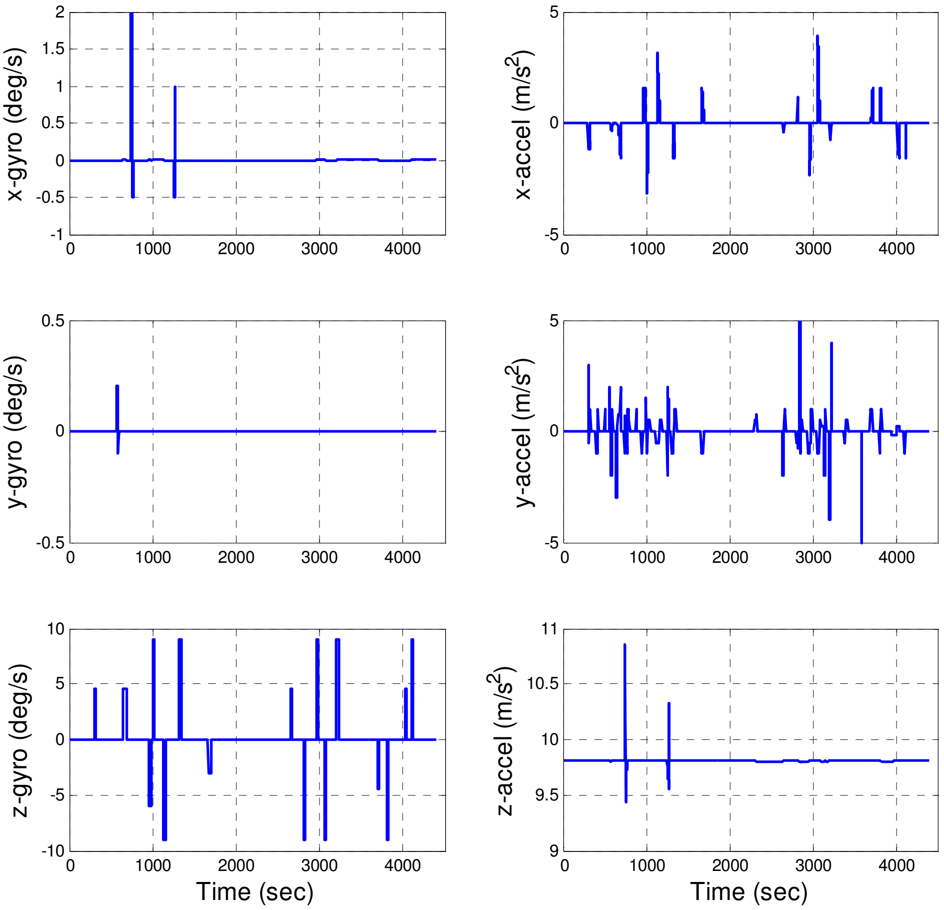

Figure 2.7: Signals from simulator with error-free

By analyzing the motions, it is obvious that the inertial sensors correctly sense the rectilinear and angular movement of the vehicle. For example, the x-axis gyro should sense the pitch angle rotation. The designed pitch angle changes around 750s and 1250s as shown in Figure 2.5.

To show individual errors and their combinations from the simulator, some INS errors were added to the error-free output through an ASCII file with a defined format to the simulator. These errors were obtained from the manufacturer specifications and lab calibrations of a hardware INS. Figure 2.8 to Figure 2.12 show examples of the simulated MEMS grade INS signals with individual error sources, ARW/VRW, SF error, and vibration, respectively. Figure 2.8 shows the simulated gyro triad signal and accelerometer triad signal along three axes with a $3\deg/\sqrt{hr}$ ARW and a $0.66m/s/\sqrt{hr}$ VRW, both based on the designed vehicle motions.

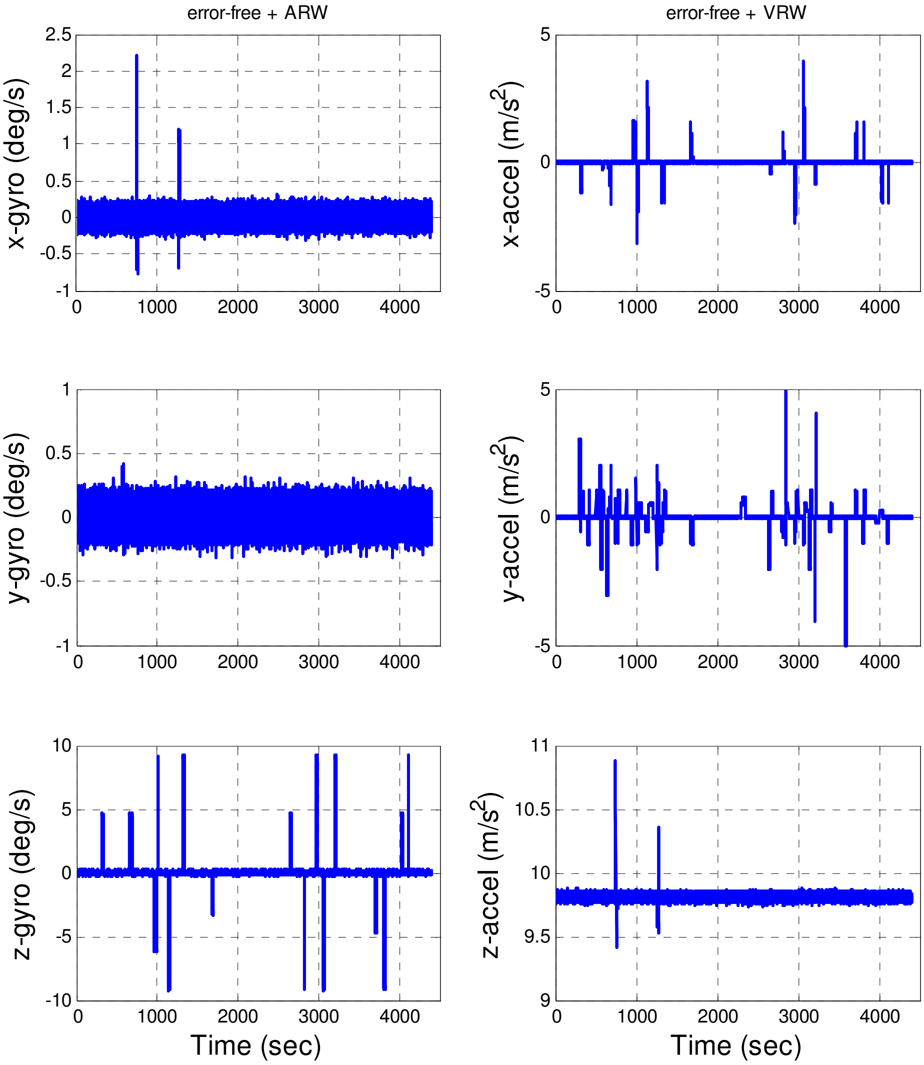

Figure 2.8: INS signals with ARW ($3\deg/\sqrt{hr}$) and VRW ($0.66 m/s/\sqrt{hr}$)

Figure 2.9 shows the gyro triad signal with a SF non-linear error of about $1000 ppm$ of the full scale $150\deg/s$ and the accelerometer triad signal with a SF non-linear error of $2000 ppm$ of the full scale $5g$.

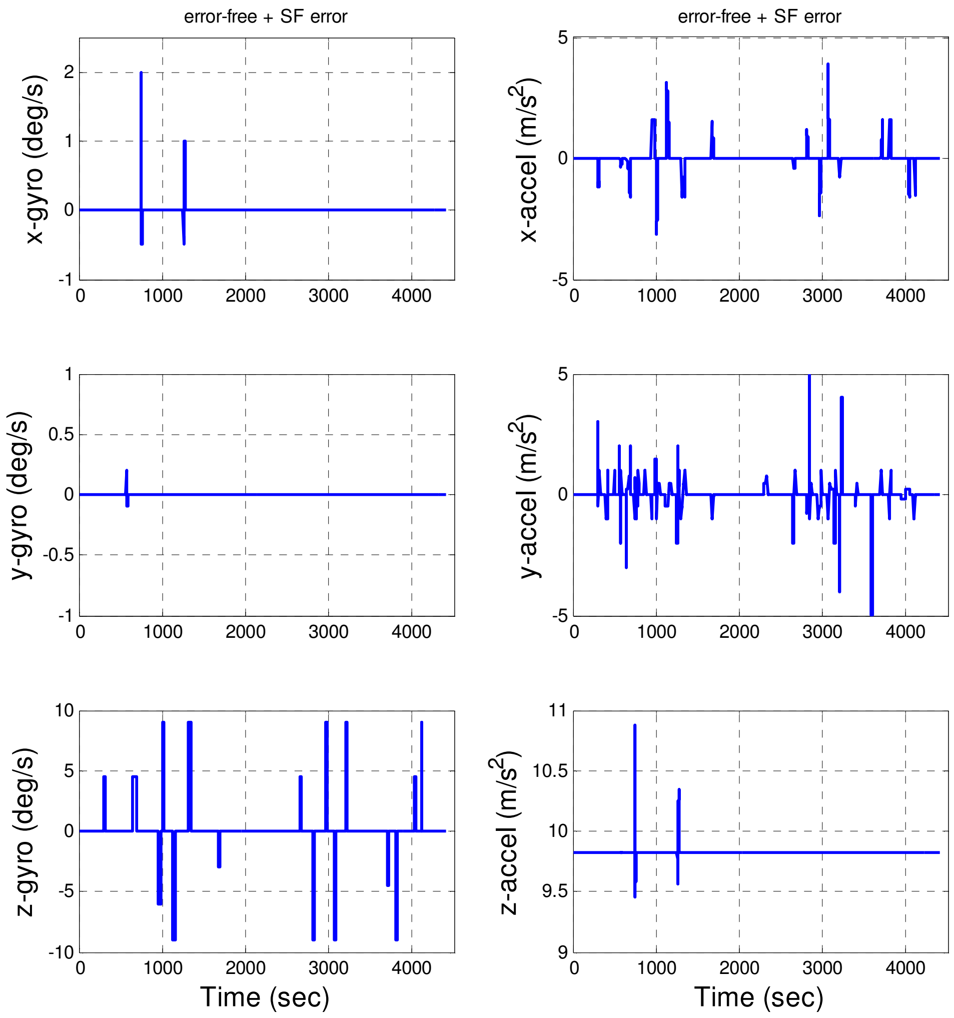

Figure 2.9: INS signals with SF errors

Figure 2.10 compares the difference between the error-free output and the actual output with SF errors. It is also clear that the quantity of this individual error source matches well to what it should be.

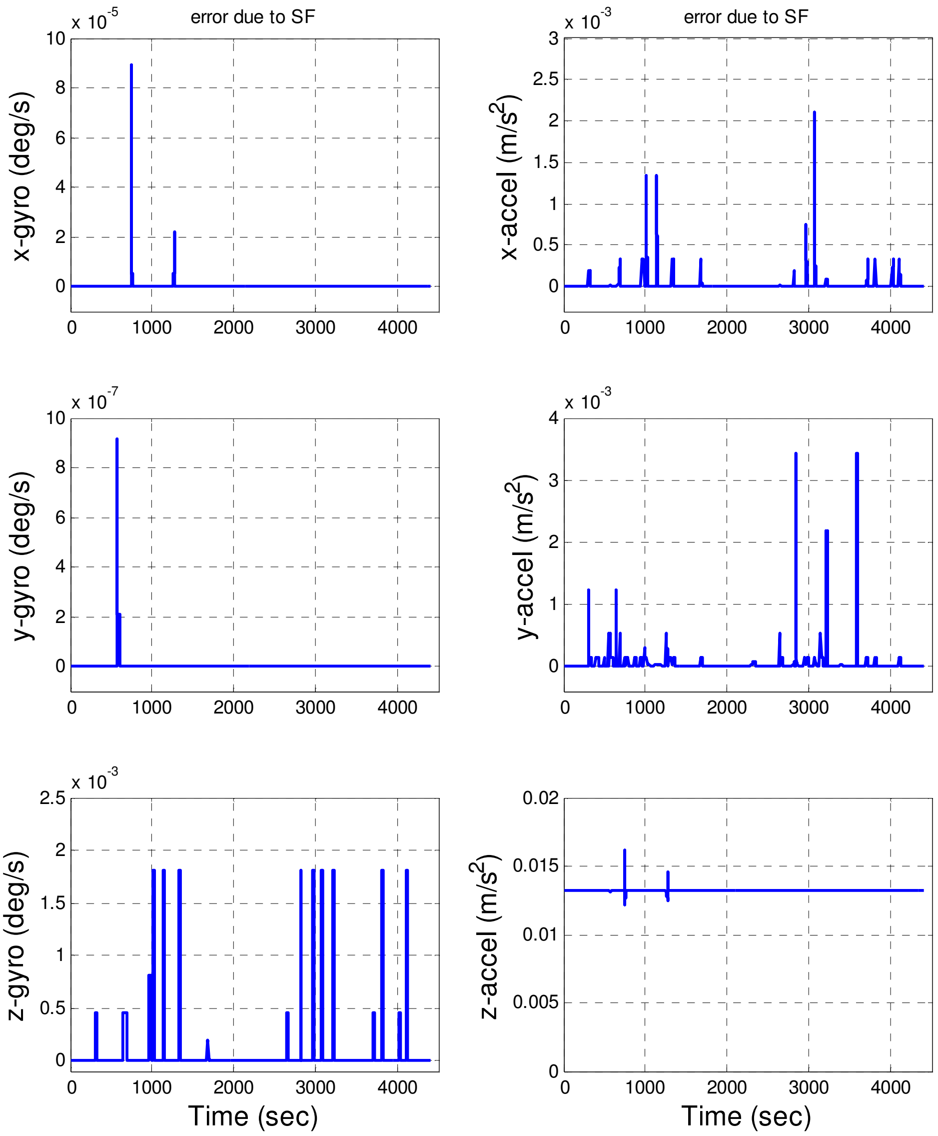

Figure 2.10: INS signal difference due to SF errors

Figure 2.11 shows the IMU signals with a vibration on the pitch angle channel during its operation. The parameters for the vibration are amplitude $0.1\deg/s$ and frequency 10Hz. A zoomed-in Figure 2.12 shows 1s zoomed-in signals. The figure indicates that the quantity of the vibration matches well to the defined parameters.

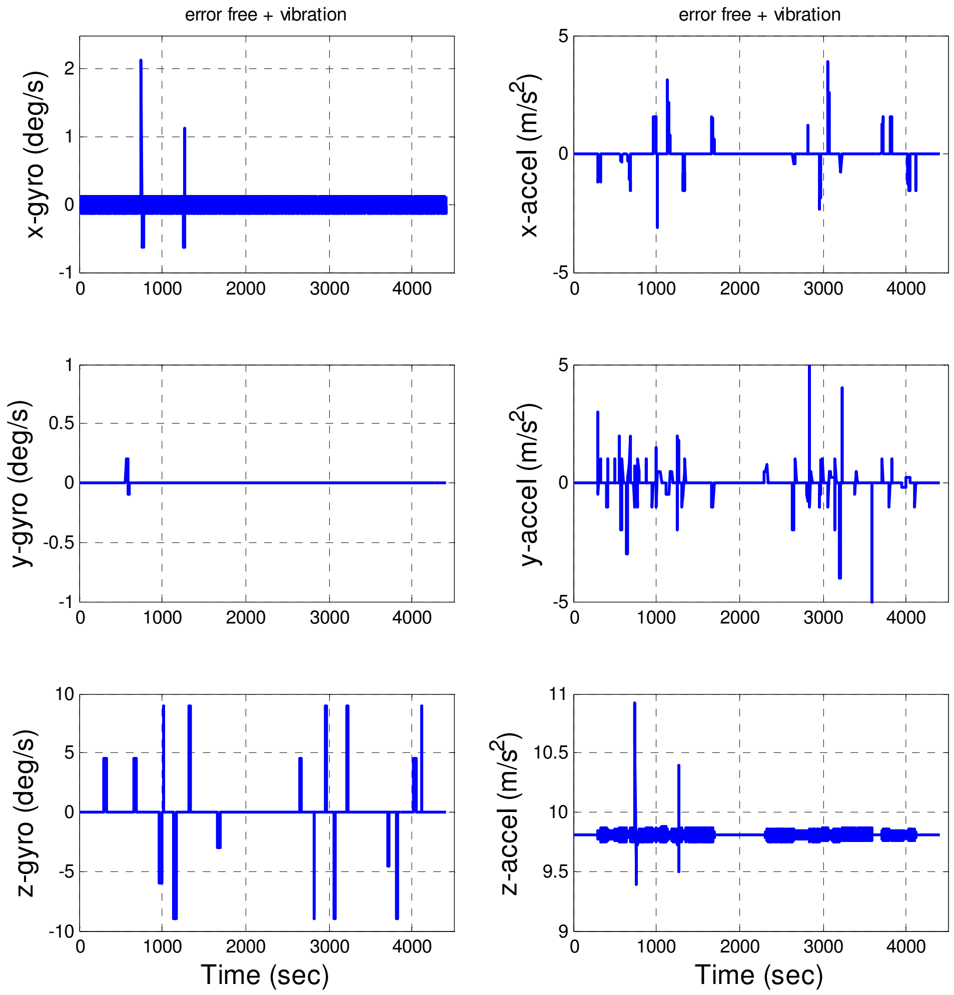

Figure 2.11: INS signals with vibration

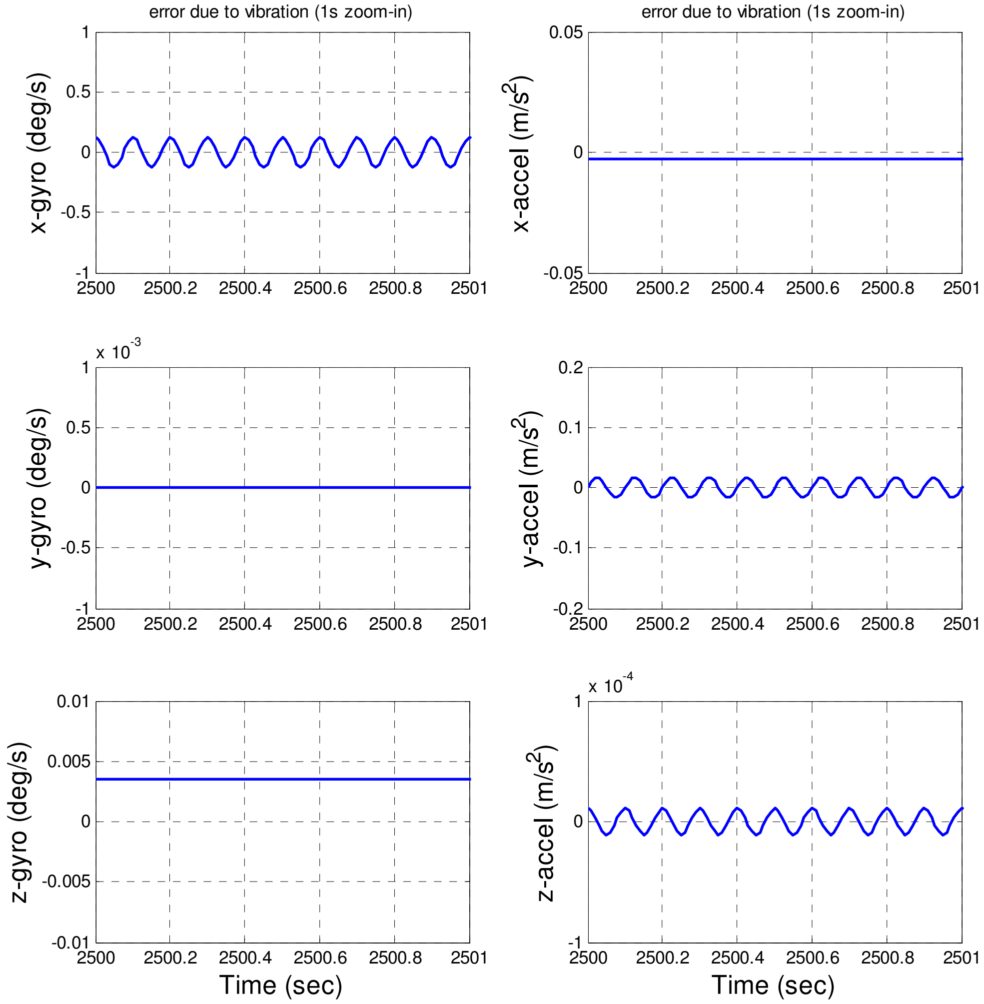

Figure 2.12: INS signals with vibration – 1s zoomed-in

Figure 2.13 shows the simulated MEMS grade INS signals with all error sources and compares this case with the error-free output. The parameters used in this simulated data set are listed in Table 2.3. This output and the outputs from the other axes of the simulator are used in the level IV (INS/GPS loose integration level) test.

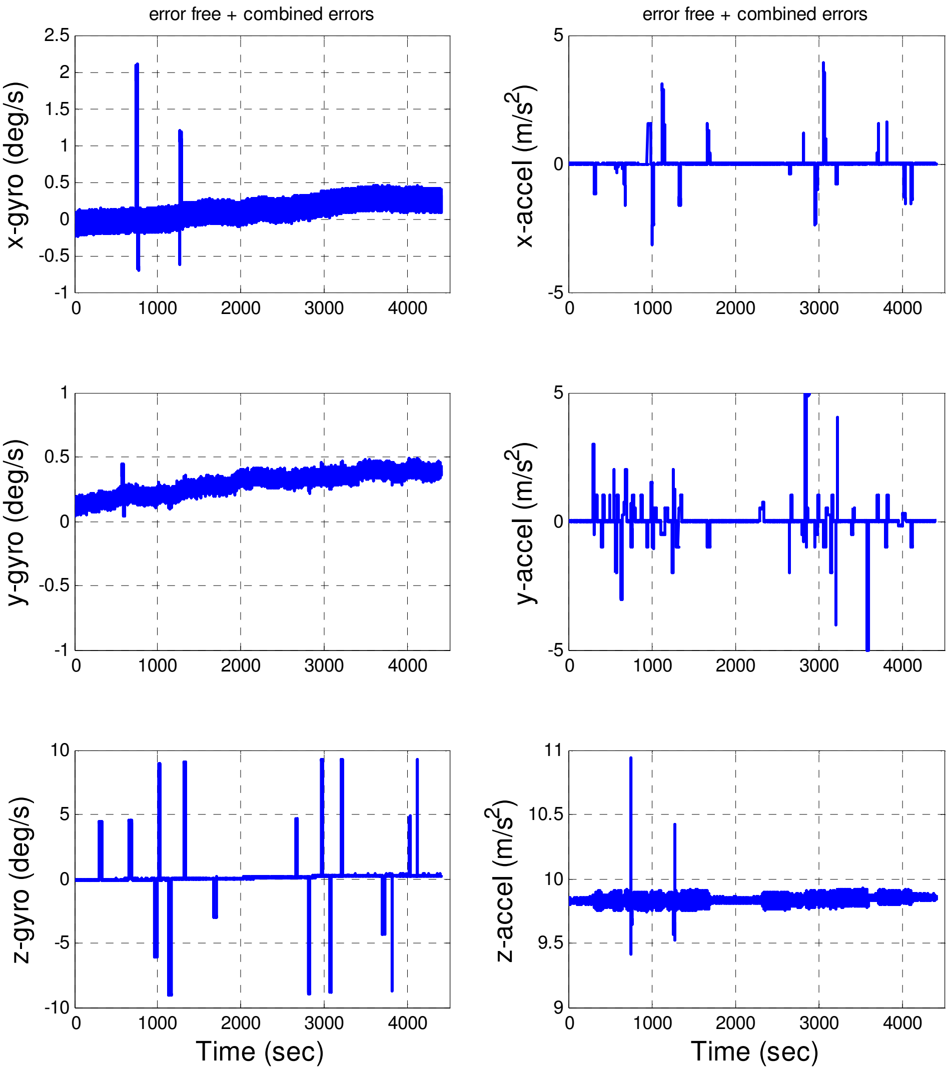

Figure 2.13: INS signals with combined errors

Table 2.3: Parameters for sensor errors used in MEMS INS simulation

Error	Value		Error	Value
b_{gM}	$200\deg/hr$		b_{aM}	$800\mu g$
n_g	$3\deg/\sqrt{hr}$		n_a	$0.66m/s/\sqrt{hr}$
S_{gNL}	$1000ppm$ of $150\deg/s$		S_{aNL}	$2000ppm$ of $5g$
b_{gC}	$0.02\deg/s/^0C$		b_{aC}	$600\mu g/^0C$
$\mathbf{N}_g$	$0.04rad$		$\mathbf{N}_a$	$0.04rad$
$\mathbf{N}_{gG}$	$180\deg/hr/g$		ΔT	$10\ ^0C$

III. Comparison to a real INS signal at the raw signal level

Verification of the simulator at this raw signal level is performed based on an ADI MEMS grade INS and its parameters. The hardware ADI INS is a very low-cost (<$100) MEMS INS, developed by the mobile-multi-sensor-system (MMSS) research group at the University of Calgary (Niu and El-Sheimy, 2005). The ADI INS integrates surface micromachining MEMS gyroscopes (ADXRS150) and accelerometers (ADXL105) developed by Analog Devices Inc. To compare simulated signals with those of the ADI INS, a field test was conducted around Springbank, Alberta in December 2005. Figure 2.14 shows the test trajectory of the car. The trajectory was recorded by a tactical grade LN200 INS and differential GPS, which is accurate enough as the reference (true values) for the MEMS INS. The simulated INS signal of the x-axis gyroscope is compared with that of the field test data, as shown in Figure 2.15.

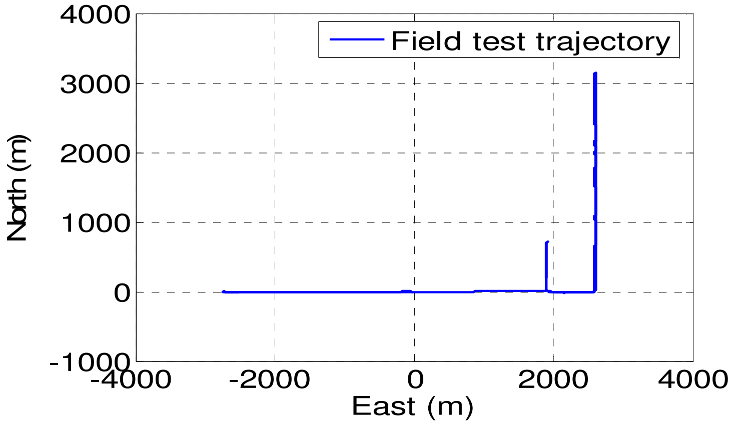

Figure 2.14: Field test trajectory

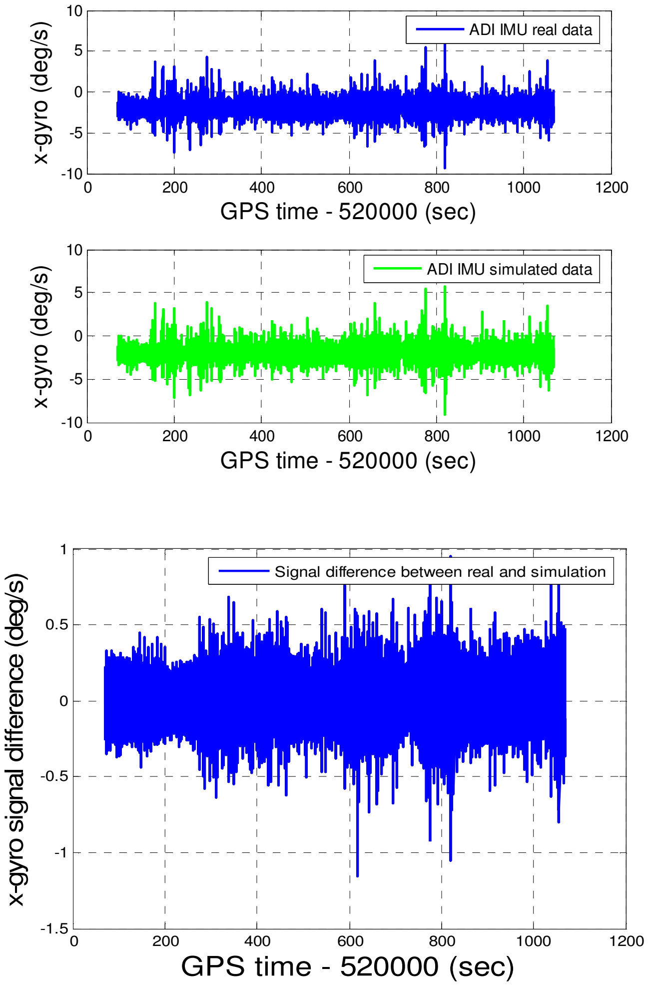

Figure 2.15: Comparison of INS signals between simulation and field test

From the Figure 2.15, it is obvious that the simulated INS signals have a good agreement with the real test signals. The mean error of the x-gyro differences is $0.01 \deg / s$ and the standard deviation is $0.12 \deg / s$, which is highly related to time synchronization of the recorded vehicle's PVA information and the accuracy of the error model.

IV. Comparison with real INS signals of an INS/GPS integrated system

At this level of verification, the simulated signals and the real hardware signals are compared using a loosely coupled INS/GPS navigation algorithm. Both simulation data and real hardware data are processed through the AINS® software. To be compatible with a loosely coupled INS/GPS integrated system, the GPS signals (i.e. Position and Velocity information) were also simulated in the simulator by defining the GPS data rate and the horizontal and vertical position/velocity standard deviations (10m/7m in this case). The field test data set was taken from the ADI hardware INS with standalone GPS solutions from a NovAtel OEM4 receiver. Both the simulated data and the field test data sets were processed in AINS® and their average position drifts during GPS blockages were compared. Figure 2.16 gives the simulated trajectory with the GPS outage periods. These outages cover a variety of dynamics including constant velocities, accelerations, decelerations, and turns. Figure 2.17 shows the position, velocity and attitude errors for defined outages based on simulated data from the simulator.

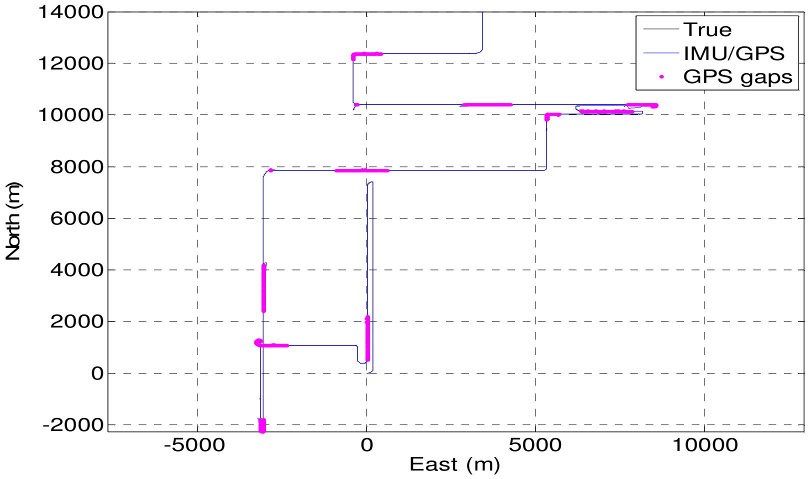

Figure 2.16: Simulated trajectory with outage periods

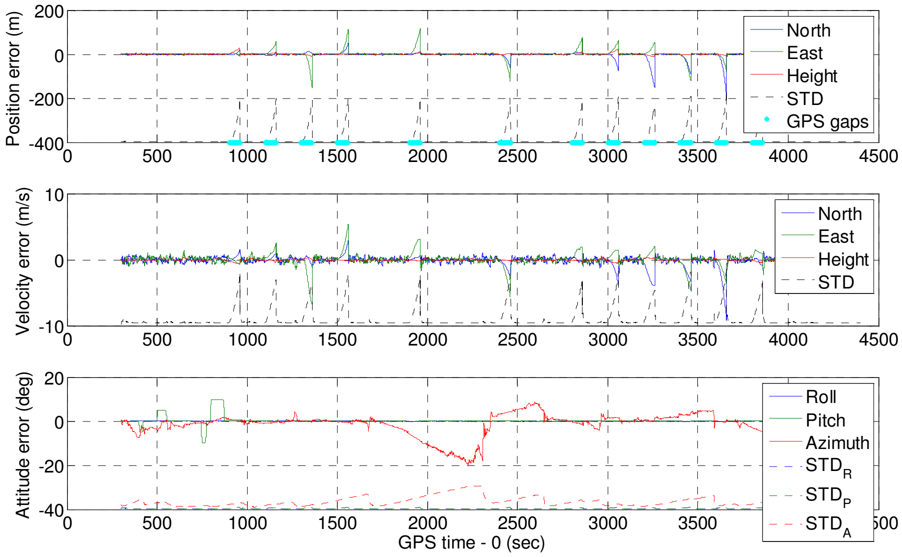

Figure 2.17: PVA error results with simulated ADI INS

The average position drift for the simulation data, which contain 12 outage periods each lasting 60 seconds, was approximately 115 meters. The largest drift was 219 meters and the smallest was 35 meters. This corresponds well to the hardware ADI INS field test results (Nasser et al, 2006) which typically averaged out to around 120 meters.

2.5 Summary

This Chapter describes a software method based INS signal simulator in details. The implementation of INS simulator is a methodical combination of an inverse process of INS mechanization and inertial sensor error models. The function of the INS simulator presented in this Chapter can generate the raw measurements of any INS such as navigation grade, tactical grade, and consumer grade systems according to a user-given application (such as airborne, land, drilling, pipeline geo-pig applications, etc.). It can simulate a variety of sensor errors such as the bias instability, random walk, scale factor errors, sensor errors due to thermal drift, g-sensitivity, nonorthogonalities, misalignment, and their combinations.

The simulator was verified through four distinct tests, involving basic principles, individual error sources, raw signals, and INS/GPS integration outputs. Performance test results show that the simulator can provide similar INS signals to that of a hardware INS.

The INS simulator is an effective, economical and flexible tool for INS related research. It can be used efficiently when choosing or designing the required hardware characteristics for a given application. It is also a fast and effective method for evaluating new sensors using datasheet characteristics provided by manufacturers or lab tests and for conducting error budgets for INS based integrated navigation system.

Chapter 3 MEMS Based INS/GPS Tightly Coupled Integration

The INS/GPS integrated system takes advantage of the complementary attributes of two systems to yield a system that provides greater precision than either of the component systems operating alone. Tightly coupled INS/GPS can continue to provide useful navigation information in situations where fewer than four GPS satellites are visible. Section 3.1 presents an overview of INS/GPS integration schemes including loose, tight (with INS aiding receiver tracking loop) and deep integration. Section 3.2 briefly introduces MEMS inertial sensors and MEMS based INSs. Section 3.3 gives mathematic expression of the extended Kalman filter, which is widely used in INS/GPS integration systems. Several implementation details are also described. Section 3.4 builds a 23-state EKF for INS/GPS tightly coupled integration and tests the developed software. First, the INS dynamic models are derived and the errors of the inertial sensors are modeled. Second, the INS pseudorange and Doppler measurements are given mathematically. Third, the tightly coupled system state vector including 23 error states and the observables are set up. Section 3.5 presents test results and analyses of MEMS based INS/GPS tight integration. To improve the navigation accuracy for a land vehicle application, a non-holonomic constraint principle and its test results are discussed in Section 3.6. Furthermore, to reduce the cost as well as the size of the physical unit of the INS/GPS integration, the integration of a GPS and a sub-optimal INS configuration with one heading gyro and two horizontal accelerometers is discussed in Section 3.7. The idea of the pseudo-signal generation in this configuration comes from INS signal software simulator described in the Chapter 2. This integration configuration will be used in the Chapter 5.

3.1 Overview of INS/GPS Integration

An INS is self-contained system that can provide a PVA solution continuously. An INS is a combination of the IMU, navigation algorithm, and the computer which hosts the algorithm. The sensors used in an INS are a triad of gyros and accelerometers. The INS algorithm is actually an integrating process that first detects acceleration then integrates it to derive velocity and displacement (Titterton and Weston, 2004). The progress in MEMS technology enables complete inertial units on a chip, composed of multiple integrated MEMS accelerometers and gyroscopes. In addition to their compact and portable size, the price of MEMS-based INS is far less than high quality INS.

An alternative navigation approach is to use GPS. A GPS receiver provides measurements of position and velocity, and/or more specifically pseudorange, carrier phase, and Doppler. The accuracy of these measurements is time-independent, i.e. with bounded errors, which is totally different from INS estimates. However, the GPS measurement accuracy is limited as a result of low signal strength, the length of the PRN code and errors in the tracking loop (Titterton and Weston, 2004). Other GPS errors arise as a result of multi-path, variations in the satellite geometry and receiver clock instability. Furthermore, with the increasing application demands, the conventional GPS positioning is challenged at the environments such as under foliage areas, urban canyons and indoors. The main characteristics of an INS and GPS in terms of their respective advantages and disadvantages are compared in Table 3.1, which indicates that they are complementary.

Table 3.1: Comparison of characteristics of INS and GPS

System	INS	GPS
Advantages	--Immune to RF --High data rate --PVA information --High accuracy in short-term --Works well under all environments	--Errors time-independent (bounded) --no pre-information needed --time standard (GPST)
disadvantages	--Errors time-dependent --Need initial alignment --no time standard	--Sensitive to RF interference --Low data rate --No attitude information

Integrated INS/GPS system provides an enhanced navigation system that has superior performance in comparison with either a stand-alone system as it can overcome each of their limitations. The integrated system presents the features of both long-term and short-term accuracy, improved availability and greater integrity (Gao, 2007). Typically, there are three strategies for the integration of GPS and INS, which are normally classified as loose coupled, tight coupled and deep coupled.

The loosely coupled integration is the simplest method of coupling. Its architecture is shown in Figure 3.1 (El-Sheimy, 2006). In this scheme, the INS and GPS receiver generate navigation solutions independently. The information from them is blended using an estimator to form a third navigation solution. Normally, an EKF is used to accomplish the blending even though currently some interest in using other non-linear estimators such as the unscented Kalman filter or particle filters has arisen (Shin, 2005).

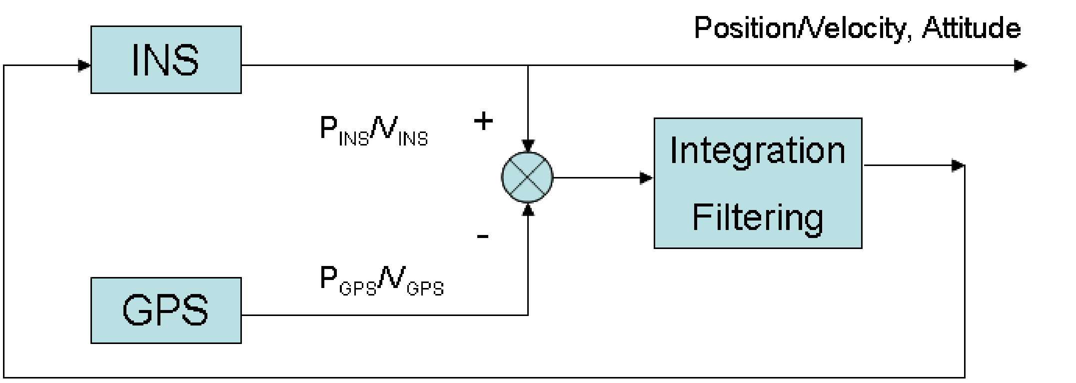

Figure 3.1: INS/GPS loosely coupled integration

The features of this scheme are that 1) GPS bounds INS error drifts; 2) INS bridges GPS momentary outages; 3) inertial sensors are calibrated on-line; 4) there is a solution backup due to two independent systems and two separated estimators.

A fundamental feature of this scheme is that it requires at least four GPS satellites in view. Its applications are limited under some environments such as vehicle navigation in urban canyons or indoor positioning where visible satellites may be fewer than four. Furthermore, this scheme has best implementation result with a higher quality INS if a receiver loses signal lock frequently and with long period, since the performance of the integrated system heavily depends on that of INS during GPS outages. Lower quality INSs, e.g. MEMS based INS, are only suited for applications where GPS outages are infrequent and short in duration.

Figure 3.2 shows architecture of the tightly coupled integration, also referred to as centralized integration (El-Sheimy, 2006). In this scheme, there is no separated GPS navigation solution filter. A single integration filter is employed to fuse INS and GPS measurements (Petovello, 2003a). The raw pseudorange and Doppler measurements from GPS tracking loop output and those from INS prediction are combined to form the input of the centralized integration filter. The filter directly accepts their differences to obtain the INS error estimates (Knight, 1999).

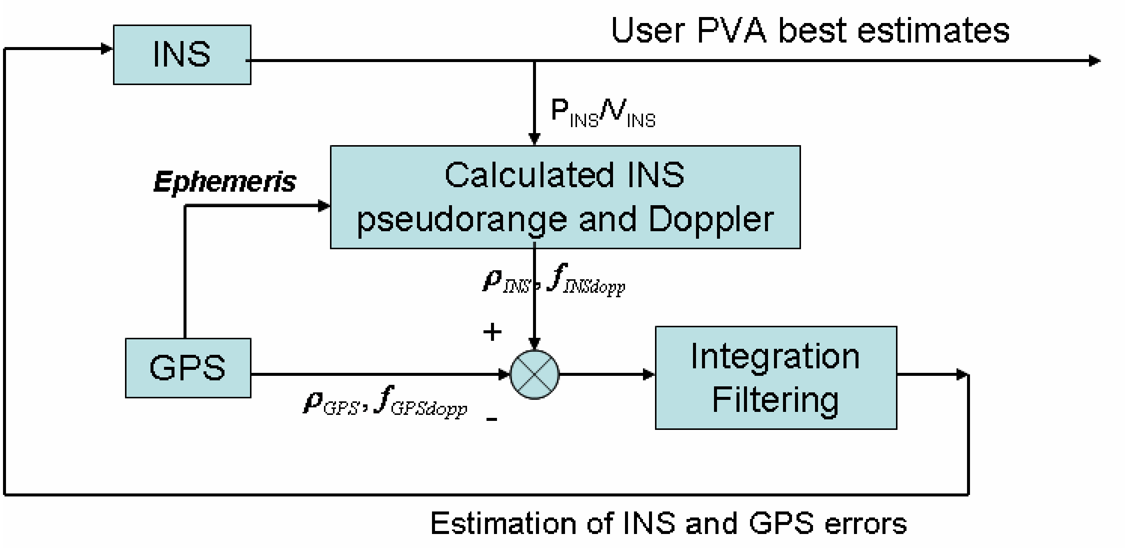

Figure 3.2: INS/GPS tightly coupled integration

This scheme provides a more accurate solution than loose integration because the basic GPS observables (pseudorange and Doppler) used in the blending process are not as correlated as the position and velocity solutions used in loose couple (Alban et al., 2003). It can continue to generate integrated navigation solution even when fewer than four satellites are being tracked. Therefore, this integration strategy is a preferred approach in urban canyons. In addition, tightly coupled leads to superior GPS fault detection and exclusion (Petovello, 2003a). Applications where output of carrier phase measurements is required especially benefit from tight integration because integer ambiguities can be recovered and verified quickly (Alban et al., 2003), which is beyond the studies of this dissertation. In general, this integration strategy is typically a preferred approach given its better performance in terms of both accuracy and system robustness, especially in urban canyon environments.

A further definition of tightly coupled appears in recent years. In the further definition, information from the integration filter is fed back to the receiver to enhance its performance (Gebre-Egziabher et al., 2007). Specifically, the INS derived velocity/Doppler information is used to aid the code and carrier tracking loop in the receiver, known as INS aiding to GPS signal tracking. This allows the receiver to remain in lock with reducing measurement noise in high-dynamic maneuvers and some extent of weak signal conditions (Petovello et al, 2007). Chapter 4 and 5 will discuss the principle, methods and implementations of such an aiding in details.

The deep integration, also known as ultra-tightly, combines GPS signal tracking and INS/GPS integration into a single Kalman filter, as illustrated in Figure 3.3 (Gebre-Egziabher et al., 2007). In this scheme, by tracking the GPS signals together, instead of using independent tracking loops, the tracking of each signal is aided by the others and by inertial data.

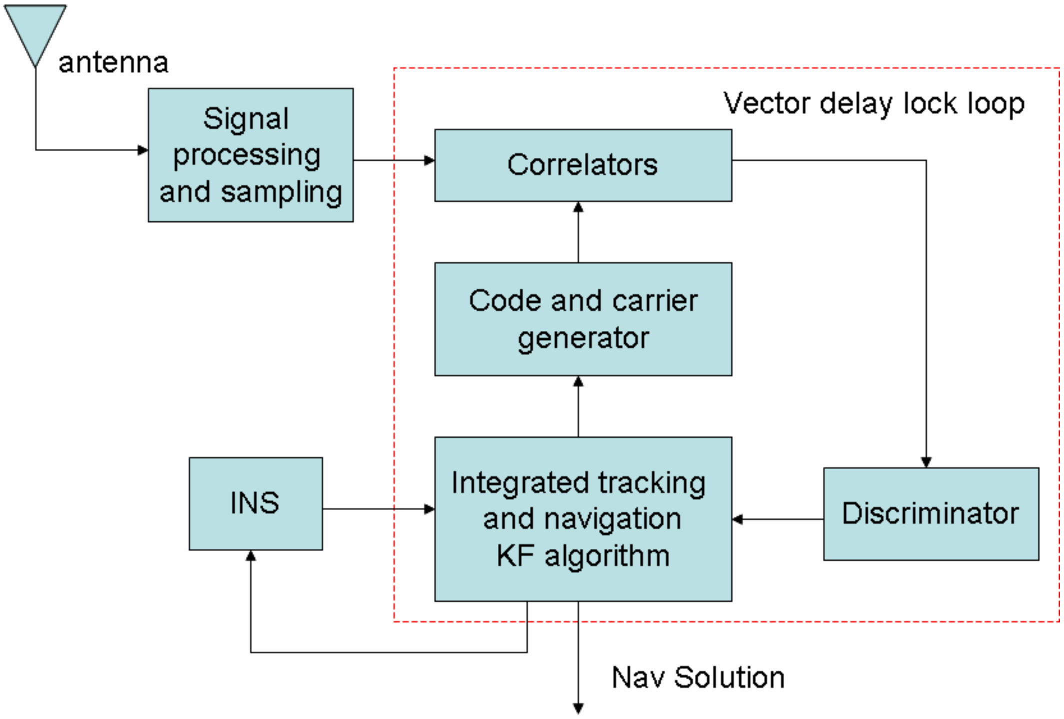

Figure 3.3: INS/GPS deeply coupled integration

In deep integration scheme, a single vector delay lock loop (VDLL) is used to fulfill the signal tracking function, which is completed by a batch of independent code and carrier tracking loops in a conventional receiver (Pany and Eissfeller, 2006; Petovello et al, 2006). The receiver is no longer an independent navigator since its operation is also partly dependent of INS information. The deep integration represents an optimal fusion of the information from an INS and a GPS receiver (Gebre-Egziabher, et al., 2007; Kim et al., 2003). However, the potential benefits described here may be achieved at the expense of greatly increased complexity, increased computational load and tight time synchronization requirements (Gebre-Egziabher, et al., 2007; Titterton and Weston, 2004).

3.2 MEMS Inertial Sensors

MEMS technology is one of the most exciting developments in inertial sensor in last twenty years. The need to maintain reasonable cost levels when integrating an INS with GPS for consumer applications is driving the technology development for MEMS inertial sensors (Barbour and Schmidt, 2001). MEMS sensor technology makes direct use of the chemical etching and batch processing techniques used by the electronics integrated circuit industry. The properties of the resulting MEMS based inertial sensors are small size, low weight, rugged construction, low power consumption, low cost as a result of high volume manufacturing, low maintenance, and compatible with operation in hostile environments (Titterton and Weston, 2004). So far, MEMS inertial sensors are the lowest cost inertial sensors available for use in commercial applications, such as land navigation (Hide, 2003). These sensors, based on their performance levels and intended applications, are often categorized under automotive grade sensors (El-Sheimy and Niu, 2007; Godha, 2006). MEMS research on inertial sensors has focused primarily on accelerometers and gyroscopes (Park, 2004).

Initial MEMS sensor developments focused on the generation of miniature accelerometers, the system and performance requirements of which were driven by the demands of the automobile industry. An accelerometer is used to measure the specific force being applied to an input axis. MEMS accelerometers may be divided into two distinct classes (Titterton and Weston, 2004): 1) the displacement of a proof mass supported by a hinge or flexure in the presence of an applied acceleration; 2) the change in frequency of a vibrating element caused by the change in tension in the element when the element is subjected to acceleration. There are four types of MEMS accelerometers named as pendulous mass, resonant (vibrating beam), tunneling, and electro-statically levitated MEMS accelerometers, referred to Titterton and Weston (2004) for details.

MEMS gyroscopes are non-rotating devices and use the Coriolis acceleration effect on a vibrating proof mass to detect inertial angular rotation. These gyros consist of a sensing element vibrating with constant amplitude controlled by a vibrating motor that maintains the oscillation at constant amplitude. When this system is rotated around any axis other than the axis of its internal in-plane vibration, the Coriolis force causes the element to oscillate out of the plane (Faulkner et al., 2002). This oscillation is picked-up by the sensing capacitors and is used to provide a measure of angular rate. There are many practical sensor configurations based upon this principle. They generally fall into one of the following three categories: simple oscillators, balanced oscillators (e.g. tuning fork MEMS gyroscope), shell resonators (e.g. resonant ring MEMS gyroscope).

As mentioned in Chapter 2, the inertial sensor errors can be divided into two parts, deterministic errors and stochastic errors. For a high-grade INS, only small random errors remain. By contrast, both deterministic part and stochastic part errors are remained in a MEMS inertial sensors based INS. The kinds of error sources are described and summarized in Equations (2.23) and (2.24). In order to integrate MEMS inertial sensors with GPS and to provide a continuous and reliable navigation solution, the calibration process is necessary. The calibration process is to understand the characteristics of different error sources and the variability of these errors. Calibration is defined as the process of comparing instrument outputs with known reference information and determining coefficients that force the output to agree with the reference information over a range of output values (Chartield, 1997). To accurately determine parameters related to deterministic errors, special calibration devices such as turn tables or special techniques are needed, such as LLF calibration, Six-position static acceleration test and angle rate tests, referred to El-Sheimy (2006) for details. The Allan variance method is a popular one to be used in determining the parameters related to random errors (Hou, 2003). Shin (2001) developed a multi-position method to determine the non-orthogonality for a sensor triad, in addition to the bias and the SF. Combining the above methods, excluding LLF calibration, we can determine both deterministic part and stochastic part errors of the gyro triad and the accelerometer triad in an IMU. The errors include bias offset, SF error, gyro g-sensitivity, non-orthogonality, SF non-linearity, ARW, VRW, SF changes due to temperature and short term instabilities. One calibration example for MEMS based INS made of ADI inertial sensors was given in Table 2.3, Chapter 2.

The process of computing the initial parameter of the DCM $\mathbf{R}_b^l$ is called the INS alignment procedure. For navigation-grade and high-end tactical grade INSs, the analytical coarse alignment method followed by fine alignment can be applied to estimate the initial attitude parameters (Farrell and Barth, 2001). However, for MEMS based INSs, these methods often fail owing to large sensor errors. The heading alignment cannot be accomplished (Noureldin et al, 2003; Godha, 2006). Another practical problem in using conventional static alignment methods is that the system is slated to be used in a consumer vehicle; hence, the user cannot be expected to wait until the sensor alignment is finished (Shin and El-Sheimy, 2004).

3.3 Discrete-Time EKF

Kalman filter is one the most popular techniques to integrate the INS and GPS. This optimal estimation technique was developed in 1960s and has been developed accompanying with the development of the modern control theory. Detailed documentations about the Kalman filter can be found in Gelb (1974), Brown and Hwang (1997), and Grewal and Andrews (2001). For a linear system with zero mean, Gaussian noise, the KF is an optimal tool to do the estimation since its covariance of state error is minimum. If the system is nonlinear or if the noise is not Gaussian, the KF is no longer an optimal choice. In this case, we can extend the use KF in such a nonlinear system through a linearization. If the linearization is around the predicted state vector, the corresponding KF is so-called extended Kalman filter. The EKF applies the Taylor series expansion for the nonlinear system and observation equations, and takes the first order terms to apply the well-developed linear Kalman filter theory, where the probability density function (PDF) is approximated by a Gaussian model (Gordon et al., 1993, Maybeck, 1994).

Inertial navigation system typically is a nonlinear dynamic system; however, its error propagation is typically done in a linear manner. The error state of the Kalman filter can be considered as the EKF, especially for the INS error control feedback loop (Shin, 2005). That is because the EKF can be used to estimate a state vector consisting of PVA and INS error states with the error states being reset to zero (ie expansion around the predicted state vector value) at each new update. The EKF has long been used in such a nonlinear system (Grewal and Andrews, 1993; Rogers, 2000; Schwarz and Wei, 2000). This section will develop the EKF algorithm for INS/GPS integration to get more accurate INS velocity measurement on the LLF. The EKF algorithm is a sequential recursive algorithm for an optimal least-mean variance estimation of the error states (Gelb, 1974). Figure 3.4 shows the flow chart of the EKF algorithm (El-Sheimy, 2006).

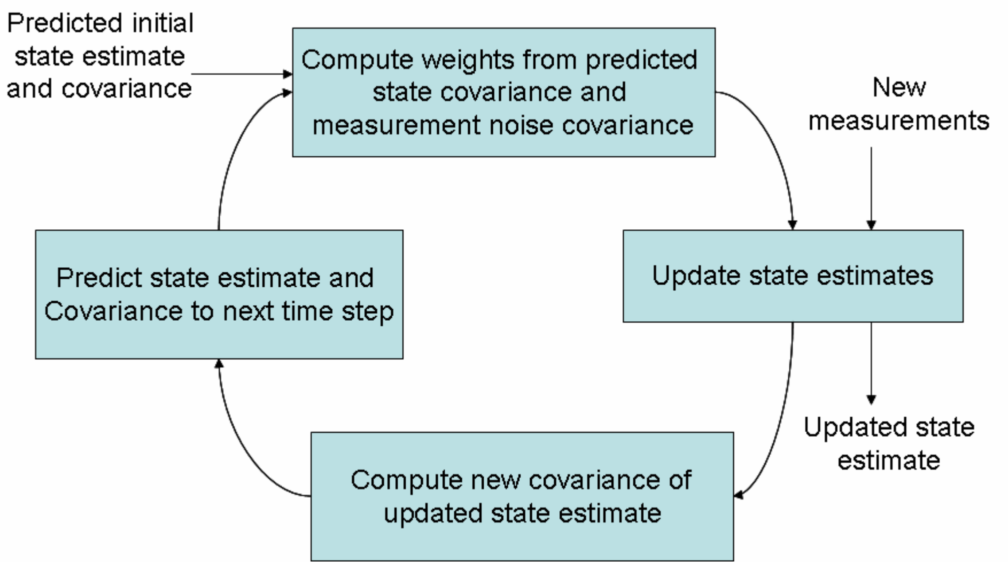

Figure 3.4: EKF algorithm flow chart

Given that a linear continuous-time (CT) system is described by the followed 1st order error state equation (Scherzinger, 2004)

$$\delta\dot{\mathbf{x}}(t) = \mathbf{F}(t)\delta\mathbf{x}(t) + \mathbf{G}(t)\mathbf{w}(t) \tag{3.1}$$

where,

$\mathbf{F}(t)$ is the system dynamics matrix;

$\delta\mathbf{x}(t)$ is the error state vector;

$\mathbf{G}(t)$ is a noise disturbance mapping matrix;

$\mathbf{w}(t)$ is a noise vector, assumed as zero-mean and Gaussian distribution. Its covariance matrix is given by $E\left[\mathbf{w}(t)\mathbf{w}(t)^T\right] = \mathbf{Q}(t)\delta(\cdot)$, where $\mathbf{Q}(t)$ is the spectral density matrix of $\mathbf{w}(t)$ and the operator $\delta(t)$ denotes the Dirac delta function whose expression is $\delta(t) = \begin{cases} 1 & t = 0 \\ 0 & t \neq 0 \end{cases}$.

Because inertial systems are usually implemented with high-rate sampled data, the CT system dynamic equations are to be transformed to their corresponding discrete-time (DT) form:

$$\delta\mathbf{x}(t_k) = \mathbf{\Phi}(t_k, t_{k-1})\delta\mathbf{x}(t_k) + \int_{t_{k-1}}^{t_k} \mathbf{\Phi}(t_k, \tau)\mathbf{G}(\tau)\mathbf{w}(\tau)d\tau \tag{3.2}$$

or in abbreviated notation as

$$\delta\mathbf{x}_k = \mathbf{\Phi}_{k,k-1}\delta\mathbf{x}_{k-1} + \mathbf{G}_{k-1}\mathbf{w}_{k-1} \tag{3.3}$$

where

$\delta\mathbf{x}_k$ is the system error state vector at t_k epoch;

$\mathbf{w}_{k-1}$ is the driven response at t_k due to the presence of the input white noise during the time interval (t_{k-1}, t_k) (Brown and Hwang, 1997). Its covariance matrix is given as $E[\mathbf{w}_k \mathbf{w}_j^T] = \begin{cases} \mathbf{Q}_k & k = j \\ \mathbf{0} & k \neq j \end{cases}$.

$\mathbf{G}_{k-1}$ is the noise coefficient matrix;

$\mathbf{\Phi}_{k,k-1}$ is the transition matrix. If the time interval $\Delta t_k = (t_{k-1}, t_k)$ is small enough or $\mathbf{F}(t)$ is approximately constant over this interval, the relation between the transition matrix and the system dynamic matrix can be written as, with an assumption of equal interval $\Delta t_k = \Delta t_{k-1}$,

$$\mathbf{\Phi}_{k,k-1} = e^{\mathbf{F}(t_{k-1})\Delta t_k} \approx \mathbf{I} + \mathbf{F}(t_{k-1})\Delta t_k + \frac{1}{2!}\mathbf{F}^2(t_{k-1})\Delta t_{k-1}^2 + \cdots \tag{3.4}$$

Considering the system's measurement is described by the following discrete-time equation

$$\delta\mathbf{Z}_k = \mathbf{H}_k \delta\mathbf{x}_k + \mathbf{n}_k \tag{3.5}$$

where

$\delta\mathbf{Z}_k$ is the measurement error vector. It is a linear combination of the error state vector $\delta\mathbf{x}_k$ and the measurement noise disturbance $\mathbf{n}_k$;

$\mathbf{H}_k$ is the design matrix, which is defined as

$\mathbf{H}_k = \left.\frac{\partial \mathbf{h}[\mathbf{x}]}{\partial \mathbf{x}}\right|_{x=\hat{x}_{k,k-1}}$, where $\mathbf{h}[\mathbf{x}]$ is the non-linear vector measurement function of the error states;

$\mathbf{n}_k$ is the DT measurement noise. Its covariance matrix is given as $E[\mathbf{n}_k \mathbf{n}_j^T] = \begin{cases} \mathbf{R}_k & k = j \\ \mathbf{0} & k \neq j \end{cases}$.

In Equations (3.3) and (3.5), the system noise and the measurement noise are assumed to be uncorrelated, i.e. $E[\mathbf{w}_k \mathbf{n}_i^T] = \mathbf{0}$ for all i, k. The covariance matrix of the error state vector is defined as $E[(\delta\hat{\mathbf{x}}_k - \delta\mathbf{x}_k)(\delta\hat{\mathbf{x}}_k - \delta\mathbf{x}_k)^T] = \mathbf{P}_k$.

The following equations are the discrete-time EKF algorithm mathematical implementation. The implementation of the EKF can be divided into two stages: measurement update and prediction. In the prediction stage, also called “time-update”, the estimate and its error covariance are as

$$\delta\hat{\mathbf{x}}_{k,k-1} = \mathbf{\Phi}_{k,k-1}\delta\hat{\mathbf{x}}_{k-1} \tag{3.6}$$

$$\mathbf{P}_{k,k-1} = \mathbf{\Phi}_{k,k-1}\mathbf{P}_{k-1}\mathbf{\Phi}^{T}_{k,k-1} + \mathbf{G}_{k-1}\mathbf{Q}_{k-1}\mathbf{G}^{T}_{k-1} \tag{3.7}$$

In the measurement update, the Kalman gain matrix $\mathbf{K}_k$, is computed first, then the state and the covariance are updated using the predicted estimate $\delta\hat{\mathbf{x}}_{k-1}$ and its covariance $\mathbf{P}_{k,k-1}$, as follows

$$\mathbf{K}_k = \mathbf{P}_{k,k-1}\mathbf{H}^{T}_{k}[\mathbf{H}_k\mathbf{P}_{k,k-1}\mathbf{H}^{T}_{k} + \mathbf{R}_k]^{-1} \tag{3.8}$$

$$\delta\hat{\mathbf{x}}_k = \delta\hat{\mathbf{x}}_{k,k-1} + \mathbf{K}_k[\delta\mathbf{Z}_k - \mathbf{H}_k\delta\hat{\mathbf{x}}_{k,k-1}] \tag{3.9}$$

$$\mathbf{P}_k = [\mathbf{I} - \mathbf{K}_k\mathbf{H}_k]\mathbf{P}_{k,k-1}[\mathbf{I} - \mathbf{K}_k\mathbf{H}_k]^{T} + \mathbf{K}_k\mathbf{R}_k\mathbf{K}^{T}_{k} \tag{3.10}$$

Typically, the frequency of the prediction loop and the update loop that are described by Equations (3.6) to (3.10) is different (Grewal and Andrews, 1993; El-Sheimy, 2006).

In the implementation of EKF, $\mathbf{Q}_k$ normally is not calculated separately. $\mathbf{G}_{k-1}\mathbf{Q}_{k-1}\mathbf{G}^{T}_{k-1}$ is often calculated together as one item from the CT system $\mathbf{G}(t)\mathbf{Q}(t)\mathbf{G}^{T}(t)$ directly (Kalman, 1963)

$$\overline{\mathbf{Q}}_k = \overline{\mathbf{Q}}(t)\Delta t_k + [\mathbf{F}(t_k) + (\mathbf{F}(t_{k-1})\overline{\mathbf{Q}}(t))^{T}]\frac{\Delta t^{2}_{k-1}}{2!} + \cdots \tag{3.11}$$

or written as following if the calculation time interval Δt_k is small enough

$$\overline{\mathbf{Q}}_k = [\overline{\mathbf{Q}}(t) + \mathbf{\Phi}_{k+1,k}\overline{\mathbf{Q}}(t)\mathbf{\Phi}^{T}_{k+1,k}]\frac{\Delta t_k}{2} \tag{3.12}$$

In above two equations, we define $\overline{\mathbf{Q}}_k$ and $\overline{\mathbf{Q}}(t)$ as

$$\overline{\mathbf{Q}}_k = \mathbf{G}_k\mathbf{Q}_k\mathbf{G}_k^T \text{ and } \overline{\mathbf{Q}}(t) = \mathbf{G}(t)\mathbf{Q}(t)\mathbf{G}^T(t) \tag{3.13}$$

3.4 EKF Design for Tight Integration

3.4.1 INS Dynamic Error Models

To formulate an EKF to fuse INS and GPS, it is necessary to develop a linear dynamic model of the errors that are to be estimated. Linearization of the INS non-linear dynamic system is the most common approach to derive a set of linear differential equations that define the INS error states.

Applying Taylor series expansion to the position mechanization equation, i.e. Equation (2.10), linearization and neglecting higher order terms, i.e. using a 1st order approximation, we have:

The position error differential equation as:

$$\delta\dot{\mathbf{r}}^l = \mathbf{D}^{-1}\delta\mathbf{V}^l - \mathbf{D}^{-1}\mathbf{D}_r\delta\mathbf{r} \tag{3.14}$$

where, $\mathbf{D}^{-1}$ is shown in Equation (2.13), and

$$\mathbf{D}_r = \begin{bmatrix} -\dot{\lambda}(R_N + h)\cos\varphi & 0 & \dot{\lambda}\cos\varphi \\ 0 & 0 & \dot{\varphi} \\ 0 & 0 & 0 \end{bmatrix}$$

$\delta\mathbf{r} = \begin{bmatrix}\delta\varphi & \delta\lambda & \delta h\end{bmatrix}^T$ is the position errors expressed by geodetic coordinates.

The velocity error differential equation as:

$$\delta\dot{\mathbf{V}}^l = \delta\mathbf{R}_b^l\mathbf{f}_{ib}^b + \mathbf{R}_b^l\delta\mathbf{f}_{ib}^b - (2\boldsymbol{\Omega}_{ie}^l + \boldsymbol{\Omega}_{el}^l)\delta\mathbf{V}^l - (2\delta\boldsymbol{\Omega}_{ie}^l + \delta\boldsymbol{\Omega}_{el}^l)\mathbf{V}^l + \delta\mathbf{g}^l$$

$$= \mathbf{V}^l \times (2\delta\boldsymbol{\omega}_{ie}^l + \delta\boldsymbol{\omega}_{el}^l) - (2\boldsymbol{\omega}_{ie}^l + \boldsymbol{\omega}_{el}^l) \times \delta\mathbf{V}^l - \mathbf{f}_{ib}^l \times \boldsymbol{\varepsilon} + \mathbf{R}_b^l \delta\mathbf{f}_{ib}^b + \delta\mathbf{g}^l \qquad (3.15)$$

In the above equation,

$\delta\mathbf{V}^l = [\delta v_E \quad \delta v_N \quad \delta v_U]^T$	is the velocity errors along ENU;
×	denotes the cross-product operation for two vectors;
$\delta\boldsymbol{\omega}_{ie}^l$	is the error of Earth rotation rate projected on l-frame, which is equal to $\delta\boldsymbol{\omega}_{ie}^l = [0 \quad -\omega_e \sin\varphi \cdot \delta\varphi \quad \omega_e \cos\varphi \cdot \delta\varphi]$;
$\delta\boldsymbol{\omega}_{ie}^l$	is the error of the transport rate, which is equal to (neglecting higher order terms) $\delta\boldsymbol{\omega}_{ie}^l = \begin{bmatrix} \dfrac{-\delta v_N}{R_M + h} & \dfrac{\delta v_E}{R_N + h} & \dfrac{\delta v_E \tan\varphi}{R_N + h} \end{bmatrix}$;
$\delta\mathbf{g}^l$	is the gravity error. It is always assumed as **0** for a vehicle near the Earth surface;
$\boldsymbol{\varepsilon}$	is the attitude error vector. The pitch error δp, the roll error δr and the heading error δA are expressed as a vector $\boldsymbol{\varepsilon} = [\delta p \quad \delta r \quad \delta A]^T$. The corresponding skew-symmetric matrix of $\boldsymbol{\varepsilon}$ can be written as $\mathbf{E} = \begin{bmatrix} 0 & -\delta A & \delta r \\ \delta A & 0 & -\delta p \\ -\delta r & \delta p & 0 \end{bmatrix}^T$;
$\mathbf{f}_{ib}^l$	is the specific force projected on l-frame, which is equal to $\mathbf{R}_b^l \mathbf{f}_{ib}^b$;
$\delta\mathbf{f}_{ib}^b$	is the error of specific force measure by the accelerometer triad. A stochastic model is necessary to describe it mathematically.

To derive the attitude error differential equation, we firstly have the error of DCM $\mathbf{R}_b^l$ is given as $\delta\mathbf{R}_b^l = \mathbf{E}\mathbf{R}_b^l$ and the computed $\hat{\mathbf{R}}_b^l$ is given as:

$$\hat{\mathbf{R}}_b^l = \mathbf{R}_b^l - \delta\mathbf{R}_b^l = (\mathbf{I} - \mathbf{E})\mathbf{R}_b^l \tag{3.16}$$

Differentiating Equation (3.16)

$$\begin{aligned}\dot{\hat{\mathbf{R}}}_b^l &= \dot{\mathbf{R}}_b^l - \dot{\mathbf{E}}\mathbf{R}_b^l - \mathbf{E}\dot{\mathbf{R}}_b^l \\ &= \mathbf{R}_b^l\mathbf{\Omega}_{lb}^b - \dot{\mathbf{E}}\mathbf{R}_b^l - \mathbf{E}\mathbf{R}_b^l\mathbf{\Omega}_{lb}^b\end{aligned} \tag{3.17}$$

On the other hand, based on the attitude mechanization Equation (2.12), we have

$$\begin{aligned}\dot{\hat{\mathbf{R}}}_b^l &= (\mathbf{I} - \mathbf{E})\mathbf{R}_b^l(\mathbf{\Omega}_{lb}^b + \delta\mathbf{\Omega}_{lb}^b) \\ &= \mathbf{R}_b^l\mathbf{\Omega}_{lb}^b + \mathbf{R}_b^l\delta\mathbf{\Omega}_{lb}^b - \mathbf{E}\mathbf{R}_b^l\mathbf{\Omega}_{lb}^b - \delta\mathbf{R}_b^l\delta\mathbf{\Omega}_{lb}^b\end{aligned} \tag{3.18}$$

Comparing Equation (3.17) and (3.18), and neglecting 2nd order term, we have

$$\dot{\mathbf{E}} = -\mathbf{R}_b^l\delta\mathbf{\Omega}_{lb}^b\mathbf{R}_l^b \text{ , i.e. } \dot{\boldsymbol{\varepsilon}} = -\mathbf{R}_b^l\delta\boldsymbol{\omega}_{lb}^b \tag{3.19}$$

In addition,

$$\begin{aligned}\boldsymbol{\omega}_{lb}^b &= \boldsymbol{\omega}_{ib}^b - \mathbf{R}_l^b(\boldsymbol{\omega}_{ie}^l + \boldsymbol{\omega}_{el}^l) \\ \delta\boldsymbol{\omega}_{lb}^b &= \delta\boldsymbol{\omega}_{ib}^b - \mathbf{R}_l^b\mathbf{E}(\boldsymbol{\omega}_{ie}^l + \boldsymbol{\omega}_{el}^l) - \mathbf{R}_l^b(\delta\boldsymbol{\omega}_{ie}^l + \delta\boldsymbol{\omega}_{el}^l)\end{aligned} \tag{3.20}$$

Substituting (3.20) into (3.19), we have the attitude error differential equation as:

$$\dot{\boldsymbol{\varepsilon}} = (\delta\boldsymbol{\omega}_{ie}^l + \delta\boldsymbol{\omega}_{el}^l) - (\boldsymbol{\omega}_{ie}^l + \boldsymbol{\omega}_{el}^l) \times \boldsymbol{\varepsilon} - \mathbf{R}_b^l\delta\boldsymbol{\omega}_{ib}^b \tag{3.21}$$

where $\delta\boldsymbol{\omega}_{ib}^b$ is the error of angular rate measured by the gyro triad. A stochastic model is necessary to describe it mathematically.

In theory, the inertial sensor errors $\delta\mathbf{f}_{ib}^{b}$ and $\delta\boldsymbol{\omega}_{ib}^{b}$ should be modeled as Equation (2.23) and (2.24). However, after compensation for the deterministic part errors and consideration of the computation burden, the inertial sensor can be modeled with sufficient accuracy using random processes such as random constant (random bias), random walk, or a Gauss-Markov (GM) process. Details of these stochastic models could be found in Gelb (1974). Therefore, in practice, for MEMS grade sensors, only the bias in-run instability, SF in-run instability and driving white noise (VRW, ARW) are considered here, all of which are modeled as 1st order Gauss-Markov process. These parameters will be changed accompanying with the KF tuning.

Therefore, we model the inertial sensor errors as

$$\delta\mathbf{f}_{ib}^{b} = \begin{bmatrix} \delta f_x^b \\ \delta f_y^b \\ \delta f_z^b \end{bmatrix} = \begin{bmatrix} ab_x \\ ab_y \\ ab_z \end{bmatrix} + \begin{bmatrix} f_x^b & 0 & 0 \\ 0 & f_y^b & 0 \\ 0 & 0 & f_z^b \end{bmatrix} \begin{bmatrix} asf_x \\ asf_y \\ asf_z \end{bmatrix} + \begin{bmatrix} n_{ax} \\ n_{ay} \\ n_{az} \end{bmatrix} \tag{3.22}$$

$$\delta\boldsymbol{\omega}_{ib}^{b} = \begin{bmatrix} \delta\omega_x^b \\ \delta\omega_y^b \\ \delta\omega_z^b \end{bmatrix} = \begin{bmatrix} gb_x \\ gb_y \\ gb_z \end{bmatrix} + \begin{bmatrix} \omega_x^b & 0 & 0 \\ 0 & \omega_y^b & 0 \\ 0 & 0 & \omega_z^b \end{bmatrix} \begin{bmatrix} gsf_x \\ gsf_y \\ gsf_z \end{bmatrix} + \begin{bmatrix} n_{gx} \\ n_{gy} \\ n_{gz} \end{bmatrix} \tag{3.23}$$

where,

$ab_{x,y,z}$	represent the accelerometer bias along body frame axes;
$asf_{x,y,z}$	represent the SF error to the accelerometer along body frame axes;
$gb_{x,y,z}$	represent the gyro bias along body frame axes;
$gsf_{x,y,z}$	represent the SF error to the gyro along body frame axes;
$n_{ax,ay,az}$	represent the driving white noise that drives a VRW, which presents as an additional velocity error to Equation (3.15);

$n_{gx,gy,gz}$ represent the driving white noise that drives a ARW, which presents as an additional attitude error to Equation (3.21). The approximate parameters for both $n_{ax,ay,az}$ and $n_{gx,gy,gz}$ can be determined by Allan variance method. These parameters as well as the followed correlation time of the white noise will be changed accompanying with the KF tuning.

All the bias and SF error are modeled as 1st GM process, as illustrated as:

$$\dot{x}(t) = -\frac{1}{\beta}x(t) + w(t) \tag{3.24}$$

where,

$w(t)$ is driving white noise that drives the GM process. Allan variance method can determine the variance σ of the GM process. Based on σ, the variance of the driving white noise σ_w is determined by

$\sigma_w = \sqrt{\frac{2\sigma^2}{\beta}}$, and

β is the correlation time of GM. It can be roughly estimated from the auto-correlation function of GM process $R(t)$. $\beta = t$, if $R(t) \approx 0.3678\sigma^2$ (Gelb, 1974; El-Sheimy, 2006).

3.4.2 INS Doppler Measurement and Pseudorange Measurement

As mentioned in section 3.1, tightly coupled INS/GPS integration involves the use of more raw measurement data, namely GPS and INS pseudorange and Doppler. This section shows how to map the INS position/velocity information on l-frame to pseudorange/Doppler domain. The Doppler shift reflects the relative movement along the line-of-sight between the satellite and the receiver antenna; i.e. the LOS movement between satellite and INS (if the level arm is compensated). The INS derived Doppler to the *k-th* satellite can be expressed simply as the velocity of the INS relative to this satellite

$$f_{INSdopp,k} = \mathbf{e}_k^T \cdot \frac{\mathbf{V}_{INS} - \mathbf{V}_{SV,k}}{\lambda_{L1}} \tag{3.25}$$

where

λ_{L1} is the L_1 carrier wavelength, $\lambda_{L1} \approx 0.19m$;

$\mathbf{e}_k = [e_{kx} \quad e_{ky} \quad e_{kz}]^T$ is the unit vector along the line-of-sight from the INS to the *k-th* satellite. e_{kx}, e_{ky}, e_{kz} are the projected components of $\mathbf{e}$ along x-axis, y-axis and z-axis in ECEF, respectively;

$\mathbf{V}_{INS} = \begin{bmatrix} v_{INS,x} & v_{INS,y} & v_{INS,z} \end{bmatrix}^T$ is the INS velocity in ECEF. It has a relation with the vehicle's true velocity (v_x, v_y, v_z), illustrated as

$$\begin{bmatrix} v_{IMU,x} \\ v_{IMU,y} \\ v_{IMU,z} \end{bmatrix} = \begin{bmatrix} v_x + \delta v_x \\ v_y + \delta v_y \\ v_z + \delta v_z \end{bmatrix} \tag{3.26}$$

where $(\delta v_x, \delta v_t, \delta v_z)$ is the INS estimated position error expressed in ECEF. Since the INS velocity mechanization is established on the ENU l-frame, $\mathbf{V}_{INS}$ is calculated by

$$\mathbf{V}_{INS} = \mathbf{R}_l^e \mathbf{V}^l \tag{3.27}$$

where $\mathbf{R}_l^e$ is the rotation matrix between the l-frame and the e-frame, expressed by Equation (2.3).

$\mathbf{V}_{SV,k} = \begin{bmatrix} v_{SV,xk} & v_{SV,yk} & v_{SV,zk} \end{bmatrix}^T$ is the *k-th* satellite's velocity in ECEF. The $\mathbf{V}_{SV,k}$ can be acquired based on the satellite's position.

In Equation (3.25), the LOS vector $\mathbf{e}$ between the *k-th* satellite and the vehicle (receiver/INS) is calculated as followed

$$\mathbf{e}_k = \begin{bmatrix} e_{kx} \\ e_{ky} \\ e_{kz} \end{bmatrix} = \begin{bmatrix} \dfrac{\partial r_k}{\partial x} \\ \dfrac{\partial r_k}{\partial y} \\ \dfrac{\partial r_k}{\partial z} \end{bmatrix} = \begin{bmatrix} \dfrac{x - x_{s,k}}{r_k} \\ \dfrac{y - y_{s,k}}{r_k} \\ \dfrac{z - z_{s,k}}{r_k} \end{bmatrix} \tag{3.28}$$

where,

(x, y, z) represents the vehicle's true position in ECEF, and

$(x_{s,k}, y_{s,k}, z_{s,k})$ represents the *k-th* satellite position in ECEF. It can be computed from the ephemeris data step by step. ICD-GPS-200C (2000) and Kaplan (1996) give all the details.

r_k is the true distance between the *k-th* satellite and the receiver. It is written as

$$r_k = \sqrt{(x - x_{s,k})^2 + (y - y_{s,k})^2 + (z - z_{s,k})^2} \tag{3.29}$$

Therefore, we have the INS Doppler measurement about the *k-th* satellite as

$$f_{INSdopp,k} = \frac{1}{\lambda_{L_1}} \left[e_{kx} \cdot (v_{INS,x} - v_{SV,xk}) + e_{ky} \cdot (v_{INS,y} - v_{SV,yk}) + e_{kz} \cdot (v_{INS,z} - v_{SV,zk}) \right] \tag{3.30}$$

and the INS pseudorange measurement as

$$\rho_{INS,k} = \sqrt{(x_I - x_{s,k})^2 + (y_I - y_{s,k})^2 + (z_I - z_{s,k})^2} \tag{3.31}$$

where

(x_I, y_I, z_I) is the INS estimated position in ECEF. It has a relation with the vehicle's true position (x, y, z), illustrated as

$$\begin{bmatrix} x_I \\ y_I \\ z_I \end{bmatrix} = \begin{bmatrix} x + \delta x \\ y + \delta y \\ z + \delta z \end{bmatrix}$$

where $(\delta x, \delta y, \delta z)$ is the INS estimated position error expressed in ECEF.

3.4.3 State Vector and Observables for EKF

In tightly-coupled INS/GPS system, the error states of the EKF include two parts. The first part is the INS error state. Its system dynamic equation is given as

$$\delta\dot{\mathbf{x}}_I = \mathbf{F}_I \delta\mathbf{x}_I + \mathbf{G}_I \mathbf{w}_I \tag{3.32}$$

If the inertial sensor errors are augmented in the error state vector, $\delta\mathbf{x}_I$ can be expressed as

$$\delta\mathbf{x}_{I,21\times 1} = \begin{bmatrix} \delta\mathbf{r}^l{}_{1\times 3} \\ \delta\mathbf{V}^l{}_{1\times 3} \\ \boldsymbol{\varepsilon}_{1\times 3} \\ \mathbf{gb}_{1\times 3} \\ \mathbf{ab}_{1\times 3} \\ \mathbf{gsf}_{1\times 3} \\ \mathbf{asf}_{1\times 3} \end{bmatrix} \tag{3.33}$$

Section 3.4.1 gives the detailed description of the elements in $\delta\mathbf{x}_I$. The corresponding elements in the dynamic matrix $\mathbf{F}_I$ are listed in the Appendix A. In Equation (3.32), $\mathbf{w}_I = [w_1 \ \cdots \ w_{21}]^T$, of which the elements all comply with the assumptions of zero-mean, Gauss distribution white noise and uncorrelated with each other. Thus, the corresponding $\mathbf{G}_I$ is a unit matrix with a rank of 21.

The second part of the error states in the tight integration EKF is the GPS error state. Typically, two error states are used to model GPS receiver at the pseudorange and Doppler level (Parkinson and Spiller, 1996; Godha, 2006). They are the receiver clock bias δt_u and the clock drift δt_{ru}, both of which are modeled as a random walk process (Parkinson and Spiller, 1996). The clock error states are defined in the units of range and range rates, by multiplying by the speed of light C, for compatibility with position and velocity states. Their differential equations can be written as followed,

$$C\delta\dot{t}_u = C\delta t_{ru} + Cw_u \tag{3.34}$$

$$C\delta\dot{t}_{ru} = Cw_{ru} \tag{3.35}$$

The system dynamic equation of GPS errors is given as

$$\delta\dot{\mathbf{x}}_G = \mathbf{F}_G \delta\mathbf{x}_G + \mathbf{G}_G \mathbf{w}_G \tag{3.36}$$

In the above equation,

$$\delta\mathbf{x}_G = \begin{bmatrix} \delta t_u \\ \delta t_{ru} \end{bmatrix} \tag{3.37}$$

$$\mathbf{F}_G = \begin{bmatrix} 0 & 1 \\ 0 & 0 \end{bmatrix} \tag{3.38}$$

$$\mathbf{G}_G = \begin{bmatrix} 1 & 0 \\ 0 & 1 \end{bmatrix} \tag{3.39}$$

$$\mathbf{w}_G = \begin{bmatrix} w_u & 0 \\ 0 & w_{ru} \end{bmatrix} \qquad \mathbf{w}_G = \begin{bmatrix} w_u \\ w_{ru} \end{bmatrix} \tag{3.40}$$

w_u and w_{ru} are assumed as the white noise.

Combining equations (3.32) and (3.36), we have the followed the system dynamic equation for INS/GPS

$$\begin{bmatrix} \delta\dot{\mathbf{x}}_I \\ \delta\dot{\mathbf{x}}_G \end{bmatrix} = \begin{bmatrix} \mathbf{F}_I & 0 \\ 0 & \mathbf{F}_G \end{bmatrix} \begin{bmatrix} \delta\mathbf{x}_I \\ \delta\mathbf{x}_G \end{bmatrix} + \begin{bmatrix} \mathbf{G}_I & 0 \\ 0 & \mathbf{G}_G \end{bmatrix} \begin{bmatrix} \mathbf{w}_I \\ \mathbf{w}_G \end{bmatrix}$$

i.e. $$\delta\dot{\mathbf{x}} = \mathbf{F}\,\delta\mathbf{x} + \mathbf{G}\mathbf{w} \tag{3.41}$$

The pseudorange and Doppler differences between GPS measurements and INS measurements are used as the observation vector $\delta\mathbf{Z}$ in the tight integration EKF. Assume there is number of m satellites in-view, the observables can be written as

$$\delta\mathbf{Z} = \begin{bmatrix} \delta\mathbf{Z}_\rho \\ \delta\mathbf{Z}_f \end{bmatrix} = \begin{bmatrix} \delta Z_{1,\rho} \\ \vdots \\ \delta Z_{m,\rho} \\ \delta Z_{1,f} \\ \vdots \\ \delta Z_{m,f} \end{bmatrix} = \begin{bmatrix} \rho_{INS,1} - \rho_{GPS,1} \\ \vdots \\ \rho_{INS,m} - \rho_{GPS,m} \\ f_{INSdopp,1} - f_{GPSdopp,1} \\ \vdots \\ f_{INSdopp,m} - f_{GPSdopp,m} \end{bmatrix} \tag{3.42}$$

where $\rho_{INS,k}$ and $f_{INSdopp,k}$ are the INS estimated pseudorange and Doppler that are determined based on the Equation (3.31) and (3.30); $\rho_{GPS,k}$ and $f_{GPSdopp,k}$ are the $k-th$ GPS satellite's pseudorange and Doppler measurements.

The GPS pseudorange measurement to the $k-th$ satellite can be written as (after compensations of the tropospheric delay and the ionospheric delay, GPS satellite orbit error and GPS satellite clock error) (Misra and Enge, 2001)

$$\rho_{GPS,k} = r_k + C\delta t_u + n_{\rho k} \tag{3.43}$$

The GPS Doppler measurement to the $k-th$ satellite can be written as (Misra and Enge, 2001)

$$f_{GPSdopp,k} = \frac{1}{\lambda_{L_1}}\left[e_{kx}\cdot(v_x - v_{SV,xk}) + e_{ky}\cdot(v_y - v_{SV,yk}) + e_{kz}\cdot(v_z - v_{SV,zk})\right] + \frac{C}{\lambda}\delta t_{ru} + n_{dk} \tag{3.44}$$

$n_{\rho k}$ and n_{dk} are mainly thermal noise from code tracking loop and carrier tracking loop, respectively. Although the magnitude of thermal noise is associated with tracking loop noise bandwidth, GPS signal strength, pre-detection bandwidth, correlator spacing, and so on, which will be revealed in the next chapter, they are assumed as the white noise in Equation (3.36). According to the principle of the receiver tracking loop, they are uncorrelated. In addition, a receiver uses parallel channels with a set of tracking loops to track each satellite (Lachapelle, 2005), therefore, the measurement noises of different satellites are uncorrelated.

Combining the Equation (3.43) and the Equation (3.31) and considering the number of m satellites being tracked, we have

$$\delta\mathbf{Z}_\rho = \begin{bmatrix} \rho_{INS,1} - \rho_{GPS,1} \\ \rho_{INS,2} - \rho_{GPS,2} \\ \vdots \\ \rho_{INS,m} - \rho_{GPS,m} \end{bmatrix} = \begin{bmatrix} e_{1x} & e_{1y} & e_{1z} \\ e_{2x} & e_{2y} & e_{2z} \\ \vdots & \vdots & \vdots \\ e_{mx} & e_{my} & e_{mz} \end{bmatrix}_{m\times 3} \begin{bmatrix} \delta x \\ \delta y \\ \delta z \end{bmatrix} + \begin{bmatrix} \delta t_u \\ \delta t_u \\ \vdots \\ \delta t_u \end{bmatrix}_{m\times 1} + \begin{bmatrix} n_{\rho 1} \\ n_{\rho 2} \\ \vdots \\ n_{\rho m} \end{bmatrix}_{m\times 1}$$

$$= \mathbf{G}_{m\times 3}\begin{bmatrix} \delta x \\ \delta y \\ \delta z \end{bmatrix} + \delta t_{u,m\times 1} + \mathbf{n}_{\rho,m\times 1} \tag{3.45}$$

Linearization of the Equation (2.2),

$$\begin{bmatrix} \delta x \\ \delta y \\ \delta z \end{bmatrix} = \begin{bmatrix} -(R_N + h)\sin\varphi\cos\lambda & -(R_N + h)\cos\varphi\sin\lambda & \cos\varphi\cos\lambda \\ -(R_N + h)\sin\varphi\sin\lambda & (R_N + h)\cos\varphi\cos\lambda & \cos\varphi\sin\lambda \\ 0 & [R_N(1-e^2)+h]\cos\varphi & \sin\varphi \end{bmatrix}\begin{bmatrix} \delta\varphi \\ \delta\lambda \\ \delta h \end{bmatrix} \tag{3.46}$$

$$= \mathbf{M}_{3\times 3}\begin{bmatrix} \delta\varphi \\ \delta\lambda \\ \delta h \end{bmatrix}$$

Substitute (3.46) into (3.45)

$$\delta\mathbf{Z}_\rho = \mathbf{G}_{m\times 3}\mathbf{M}_{3\times 3}\begin{bmatrix} \delta\varphi \\ \delta\lambda \\ \delta h \end{bmatrix} + \delta t_{u,m\times 1} + \mathbf{n}_{p,m\times 1}$$

$$= \mathbf{H}_{\rho,m\times 3}\begin{bmatrix} \delta\varphi \\ \delta\lambda \\ \delta h \end{bmatrix} + \delta t_{u,m\times 1} + \mathbf{n}_{p,m\times 1} \tag{3.47}$$

Combining the Equation (3.44) and the Equation (3.30) and considering the number of m satellites being tracked, we have

$$\delta\mathbf{Z}_f = \begin{bmatrix} f_{INSdopp,1} - f_{GPSdopp,1} \\ f_{INSdopp,2} - f_{GPSdopp,2} \\ \vdots \\ f_{INSdopp,mm} - f_{GPSdopp,m} \end{bmatrix} = \begin{bmatrix} e_{1x} & e_{1y} & e_{1z} \\ e_{2x} & e_{2y} & e_{2z} \\ \vdots & \vdots & \vdots \\ e_{mx} & e_{my} & e_{mz} \end{bmatrix}_{m\times 3}\begin{bmatrix} \delta v_x \\ \delta v_y \\ \delta v_z \end{bmatrix} + \begin{bmatrix} \delta t_{ru} \\ \delta t_{ru} \\ \vdots \\ \delta t_{ru} \end{bmatrix}_{m\times 1} + \begin{bmatrix} n_{d1} \\ n_{d2} \\ \vdots \\ n_{dm} \end{bmatrix}_{m\times 1}$$

$$= \mathbf{G}_{m\times 3}\begin{bmatrix} \delta v_x \\ \delta v_y \\ \delta v_z \end{bmatrix} + \delta t_{ru,m\times 1} + \mathbf{n}_{d,m\times 1} \tag{3.48}$$

According to the definition of the rotation matrix $\mathbf{R}_l^e$, illustrated in the Equation (2.3), we have

$$\begin{bmatrix} \delta v_x \\ \delta v_y \\ \delta v_z \end{bmatrix} = \mathbf{R}_l^e \begin{bmatrix} \delta v_E \\ \delta v_N \\ \delta v_U \end{bmatrix} \tag{3.49}$$

Substitute (3.49) into (3.48)

$$\begin{aligned} \delta \mathbf{Z}_f &= \mathbf{G}_{m\times 3}\mathbf{R}_l^e \begin{bmatrix} \delta v_E \\ \delta v_N \\ \delta v_U \end{bmatrix} + \delta t_{ru,m\times 1} + \mathbf{n}_{d,m\times 1} \\ &= \mathbf{H}_{f,m\times 3} \begin{bmatrix} \delta v_E \\ \delta v_N \\ \delta v_U \end{bmatrix} + \delta t_{ru,m\times 1} + \mathbf{n}_{d,m\times 1} \end{aligned} \tag{3.50}$$

Consequently, the system's measurement equation is written as

$$\delta \mathbf{Z} = \mathbf{H}\delta \mathbf{x} + \mathbf{n} \tag{3.51}$$

where

$\delta \mathbf{Z} = \begin{bmatrix} \delta \mathbf{Z}_\rho \\ \delta \mathbf{Z}_f \end{bmatrix}$ is the observable vector, and

$\mathbf{n}$ is the measurement noise vector, which is expressed as $\mathbf{n} = \begin{bmatrix} \mathbf{n}_\rho^T & \mathbf{n}_d^T \end{bmatrix}^T$, and

$\mathbf{H}$ is the design matrix, which is expressed as

$$\mathbf{H} = \begin{bmatrix} \mathbf{H}_{\rho,m\times 3} & \mathbf{0}_{m\times 18} & \mathbf{H}_{c,m\times 1} & \mathbf{0}_{m\times 1} \\ \mathbf{0}_{m\times 3} & \mathbf{H}_{f,m\times 3} & \mathbf{0}_{m\times 16} & \mathbf{H}_{c,m\times 1} \end{bmatrix}^T \tag{3.52}$$

where $\mathbf{H}_c = \begin{bmatrix} 1 & 1 & \cdots & 1 \end{bmatrix}_{1\times m}^T$.

3.5 Performance Tests and Analysis

A field test was conducted around Springbank, Alberta in December 2005. The data from an ADI MEMS INS and a NovAtel's OEM4 receiver single point positioning were collected. The OEM4 GPS antenna was mounted on the roof of a van. At the same time, a tactical grade INS, LN200, was mounted inside the van to provide the reference trajectory. The trajectory was acquired from the smoothed estimate of the LN200 and differential GPS data processed by Applanix Corporation POSPac™ software. The system setup is shown in Figure 3.5.

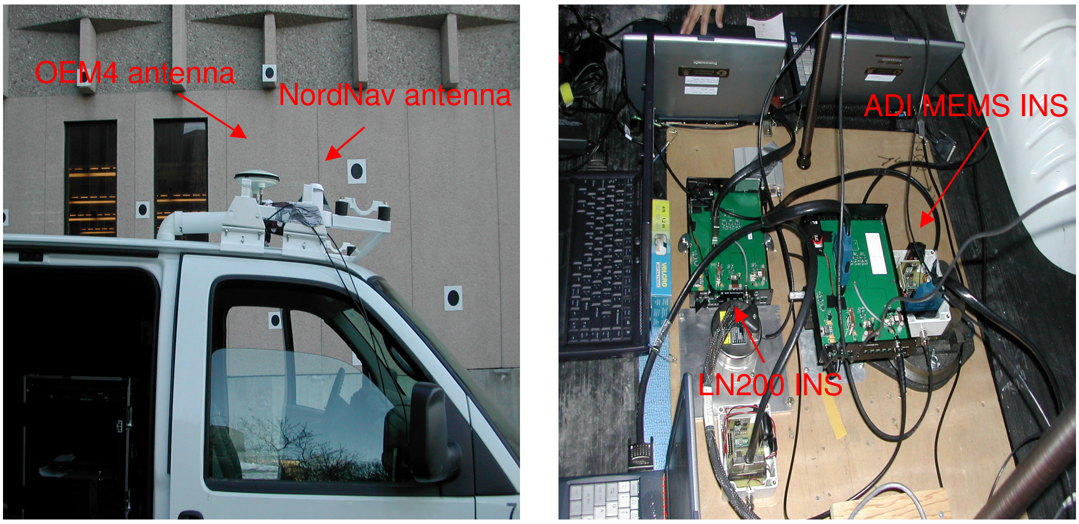

Figure 3.5: Field test setup

The ADI MEMS INS was powered by 9V batteries while the power of LN200 was supplied from an external 24V battery cell. The OEM4 receiver was powered by the 12V outlet in the van. In addition, a NordNav receiver antenna that was connected to the NordNav front-end was also mounted on the roof of the van to record datasets used in the Chapter 5.

The datasets from OEM4 GPS and ADI INS were post-processed by the developed INS/GPS tightly coupled integration software package in this dissertation. An approximate L-shape trajectory was driven in the field test as shown in Figure 3.6, where (a), (b), (c) and (d) show trajectories, velocities, pitch/roll and heading, respectively.

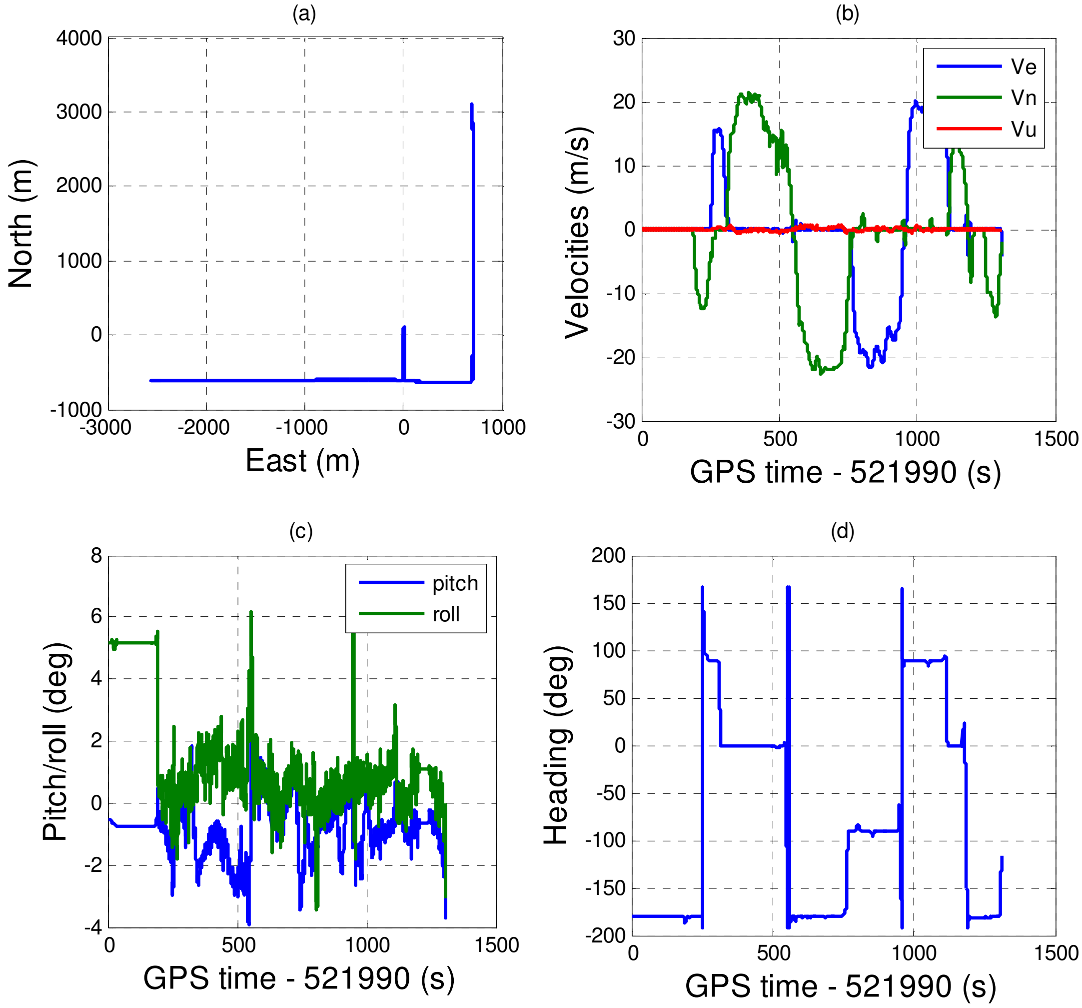

Figure 3.6: Vehicle's trajectory and motions

To check the performance of the tightly coupled integration, ten 30-second GPS signal outage scenarios were simulated. These ten scenarios covered most of the vehicle's dynamics, such as static periods, accelerations, decelerations, turns, U-turns, tilts, and so on. During each outage period, it is assumed that fewer than four GPS satellites are being tracked to simulate the urban canyon environments. The satellite geometry is selected randomly, which means that the PRN of satellites being tracked is not fixed and the signs of the azimuth of satellites might be same (satellites on one side of the vehicle) or different (satellites on both sides of the vehicle). Figure 3.7 and Figure 3.8 show the navigation errors and the receiver clock errors about an example with two satellites being tracked. Table 3.2 lists the results of the 3D position error δr, velocity error δV, and heading error δA during the simulated ten GPS signal outage periods. Table 3.3 compares mean values of the navigation errors for different situations where only 3 satellites, 2 satellites, 1 satellite, or 0 satellite is being tracked, respectively.

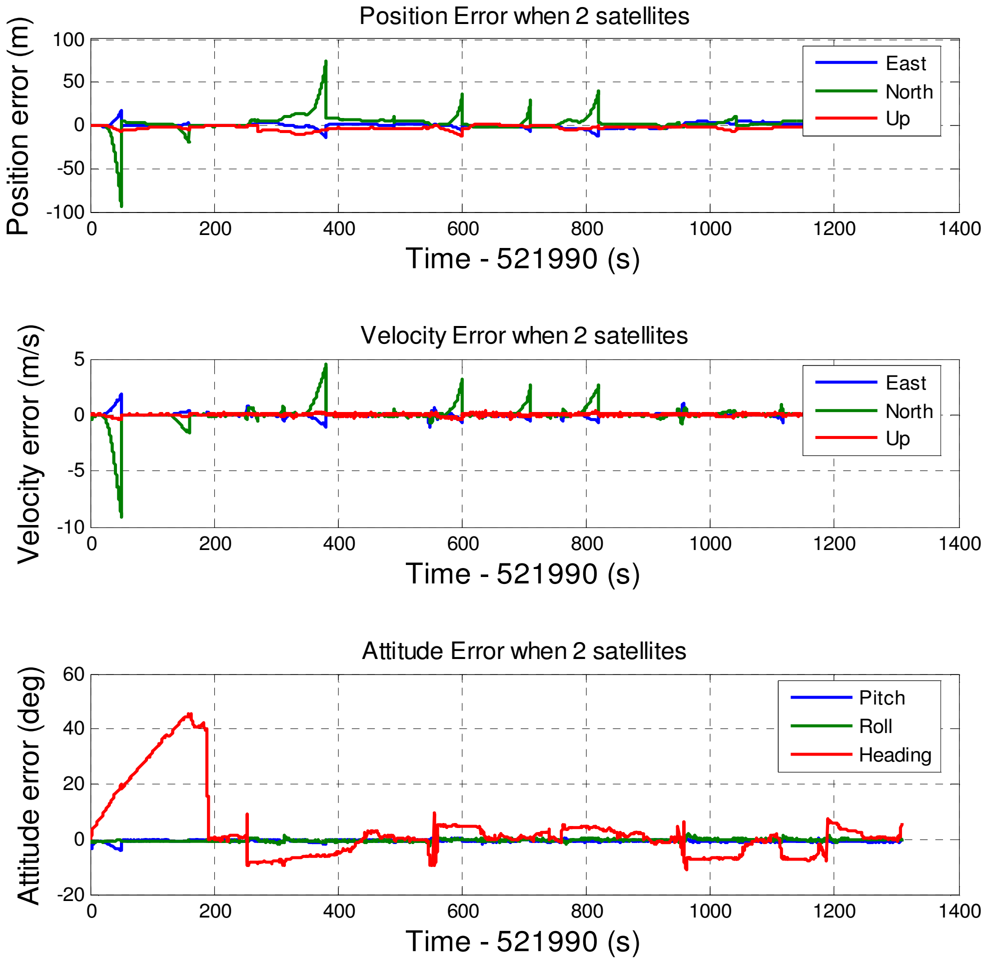

Figure 3.7: PVA errors for 2 satellites case

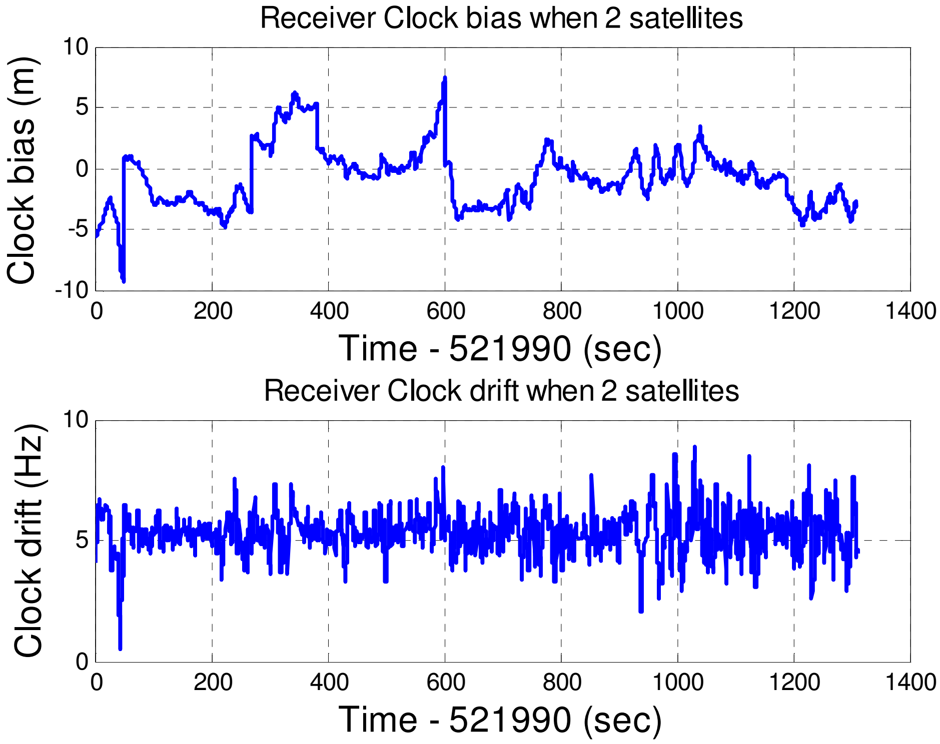

Figure 3.8: Clock errors for 2 satellites case

Table 3.2: Individual errors during 10 GPS signal outage periods

errors	No. of outage periods (2 satellites only)										
	1	2	3	4	5	6	7	8	9	10	Mean / 1σ
$\delta r(m)$	88.4	19.1	5.0	71.8	10.1	36.5	27.4	39.6	3.7	12.9	31.4 (mean)
$\delta V(m/s)$	8.8	1.5	0.4	4.4	0.3	3.2	2.6	2.6	0.1	0.4	2.4 (mean)
$\|\delta A\|$(deg)	19.4	45.5	8.6	6.1	1.0	4.7	0.7	4.4	1.4	6.9	9.4 (mean)

Table 3.3: Errors comparison of different numbers of satellites being tracked

numbers of Satellites	$\delta r(m)$ (mean)	$\delta V(m/s)$ (mean)	$\lvert\delta A\rvert$(deg) (mean)
3	< 7.0	< 0.2	8.4
2	31.4	2.4	9.4
1	40.1	3.2	9.9
0	40.3	3.1	10.1

The results from the above figures and tables reveal that 1) the tightly coupled INS/GPS can work well under the environment with fewer than four satellites, which is superior to the loose couple; 2) the navigation errors increase dramatically during static periods because of the bad observability in EKF; 3) fewer satellites being tracked result in worse navigation performance due to the worse satellites geometry; 4) The navigation errors with 1 satellite in-view are almost the same as that of the case of no satellite available. Its estimation errors are also associated with both the vehicle's dynamics and the satellite geometry. There is a large standard deviation in the clock drift estimation in the case of only one satellite being tracked. The clock drift estimate is to be used for the INS aided GPS tracking loop discussed the Chapter 5 of this dissertation.

3.6 Using Non-holonomic Constraint

For land vehicle navigation, non-holonomic constraint is a popular method to improve the navigation accuracy. Non-holonomic constraint refers to the fact that unless the vehicle jumps off the ground (along z-axis) or slides on the ground (along x-axis), the velocity of the vehicle in the plane perpendicular to the forward direction (along y-axis) is almost zero (Sukkarieh, 2000; Shin, 2001). Therefore, two non-holonomic constraints can be considered as additional measurement updates in addition to the GPS pseudorange and Doppler measurements to the EKF.

Thus, the above concept can be described mathematically by

$$\begin{aligned} V_x^b &\approx 0 + n_{vbx} \\ V_z^b &\approx 0 + n_{vbz} \end{aligned} \tag{3.53}$$

where n_{vbx} and n_{vbz} is the measurement noise value denoting any possible discrepancies in the above stated assumptions for a particular direction (x or z). The magnitude of the noise is chosen to reflect the extent of the expected constraint violations (Sukkarieh 2000; Godha, 2006).

The estimation of the velocity in the b-frame $\hat{\mathbf{V}}_{ib}^b$ can be acquired by

$$\hat{\mathbf{V}}_{ib}^b = \mathbf{V}_{ib}^b + \delta\mathbf{v}^b = \hat{\mathbf{R}}_l^b \hat{\mathbf{V}}_{ib}^l = \mathbf{R}_l^b (\mathbf{V}_{ib}^l + \delta\mathbf{v}_{ib}^l) \tag{3.54}$$

where

$\mathbf{V}_{ib}^b = \begin{bmatrix} V_x^b & V_y^b & V_z^b \end{bmatrix}^T$ is the land vehicle's true velocity in the b-frame;

$\delta\mathbf{v}^b = \begin{bmatrix} \delta v_x^b & \delta v_y^b & \delta v_z^b \end{bmatrix}^T$ is the velocity error vector in the b-frame;

$\hat{\mathbf{R}}_l^b$ is the computed DCM, which is expressed by the Equation (3.16);

$\mathbf{V}_{ib}^l$ is the vehicle's velocity in the b-frame with respect to the i-frame projected in the l-frame, and $\delta\mathbf{v}_{ib}^l$ is its corresponding error vector.

$\mathbf{V}_{ib}^{l}$ can be mathematically expressed as

$$\mathbf{V}_{ib}^{b} = \mathbf{R}_{l}^{b}(\mathbf{V}_{ie}^{l} + \mathbf{V}^{l} + \mathbf{V}_{lb}^{l})$$

where $\mathbf{V}_{ie}^{l}$ represents the Earth's computed rectilinear motions with respect to the i-frame. According to the frame definitions in the Chapter 2, $\mathbf{V}_{ie}^{l}$ should be equal to a zero vector if the Earth's auto-rotation is the only motion considered with respect to the i-frame. $\mathbf{V}_{lb}^{l}$ represents the rectilinear motions between the b-frame and the l-frame. Similarly, $\mathbf{V}_{lb}^{l}$ should be equal to a zero vector due to the same origin according to the frame definitions. Thus, we have $\mathbf{V}_{ib}^{b} = \mathbf{R}_{l}^{b}\mathbf{V}^{l}$ and $\delta\mathbf{v}_{ib}^{l} = \delta\mathbf{V}^{l}$.

So, the Equation (3.53) can be re-written as

$$\mathbf{V}_{ib}^{b} + \delta\mathbf{v}^{b} = \mathbf{R}_{l}^{b}(\mathbf{I} + \mathbf{E})(\mathbf{V}^{l} + \delta\mathbf{V}^{l}) \tag{3.55}$$

Collecting terms to the first order, we have

$$\delta\mathbf{v}^{b} = \mathbf{R}_{l}^{b}\delta\mathbf{V}^{l} - \mathbf{R}_{l}^{b}(\mathbf{V}^{l}\times)\boldsymbol{\varepsilon} \tag{3.56}$$

Using non-holonomic constraint, we have the followed measurements

$$\delta\mathbf{Z}_{non\text{-}hol} = \begin{bmatrix} \delta v_{x}^{b} \\ \delta v_{z}^{b} \end{bmatrix} \tag{3.57}$$

Therefore, the corresponding design matrix $\mathbf{H}_{non\text{-}hol}$ can be written as

$$\mathbf{H}_{non\text{-}hol} = \begin{bmatrix} \mathbf{0}_{2\times3} & \mathbf{H}_{non-1},_{2\times3} & \mathbf{H}_{non-2},_{2\times3} & \mathbf{0}_{2\times14} \end{bmatrix} \tag{3.58}$$

where

$$\mathbf{H}_{non\text{-}1} = \begin{bmatrix} \mathbf{R}_{l}^{b}(1,1) & \mathbf{R}_{l}^{b}(1,2) & \mathbf{R}_{l}^{b}(1,3) \\ \mathbf{R}_{l}^{b}(3,1) & \mathbf{R}_{l}^{b}(3,2) & \mathbf{R}_{l}^{b}(3,3) \end{bmatrix},$$

$$\mathbf{H}_{non\text{-}2} = \begin{bmatrix} \mathbf{V}^U \mathbf{R}_l^b(1,2) - \mathbf{V}^N \mathbf{R}_l^b(1,3) & -\mathbf{V}^U \mathbf{R}_l^b(1,2) + \mathbf{V}^E \mathbf{R}_l^b(1,3) & \mathbf{V}^N \mathbf{R}_l^b(1,1) - \mathbf{V}^E \mathbf{R}_l^b(1,2) \\ \mathbf{V}^U \mathbf{R}_l^b(3,2) - \mathbf{V}^N \mathbf{R}_l^b(3,3) & -\mathbf{V}^U \mathbf{R}_l^b(3,1) + \mathbf{V}^E \mathbf{R}_l^b(3,3) & \mathbf{V}^N \mathbf{R}_l^b(3,1) - \mathbf{V}^E \mathbf{R}_l^b(3,2) \end{bmatrix}$$

where,

$\mathbf{R}_l^b(i,j)$ represents an element of $\mathbf{R}_l^b$ located on the $i-th$ row and the $j-th$ column.

Repeat the tests given in the above section. Figure (3.9) shows the navigation errors for the case of two satellites being tracked and using non-holonomic constraint.

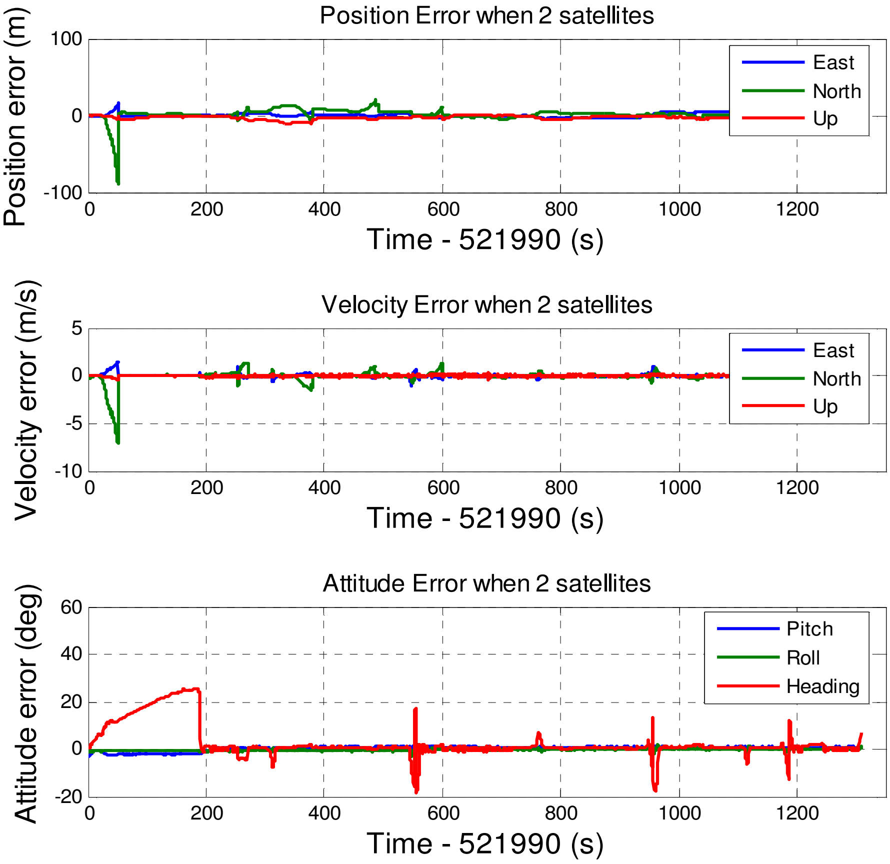

Figure 3.9: PVA errors for 2 satellites case by using non-holonomic constraint

Table 3.4 gives the results and improvements of navigation errors for 3 or 2 or 1 or 0 satellite(s) cases. The results clearly show that the non-holonomic constraint significantly improves the navigation performance for periods of signal outage. It is an attractive technique for land vehicle’s navigation. Normally, such a velocity constraint provides more contributions to fewer satellites case. However, compared Figure 3.9 and 3.7, we should note that the non-holonomic constraint has less improvements during static periods because of the actual zero velocities along the b-frame. Furthermore, the percentage of the improvement to the heading error decreases with the reduction of the number of satellites. That is because that the worse satellite geometry results in the worse velocity measurement update. From the view of the Kalman filter, the system relies more on the prediction rather than the update under the worse geometry. In INS/GPS tight couple integration, the prediction process of EKF is heavily dependent of INS behaviors, where the heading error is weakly coupled with east velocity error due to Schuler effect (El-Sheimy, 2006). Therefore, the non-holonomic constraint contributes less to the heading error improvement in fewer satellites case.

In addition, from the principle of the non-holonomic, the use of this constraint provides limited improvements in the forward direction. To prevent error growth in the forward direction an odometer can be used alongside velocity constraints (e.g. Nassar et al., 2006). Currently, the use of an odometer in a land vehicle is somehow compromised by its cost and complexity.

Table 3.4: Navigation errors and their improvement by using non-holonomic

numbers of Satellites		$\delta r(m)$ (mean)	$\delta V(m/s)$ (mean)	$\lvert\delta A\rvert(\deg)$ (mean)
3	errors	< 7.0	< 0.1	3.5
	improvement	---	50%	58%
2	errors	13.8	1.1	4.6
	improvement	56%	54%	51%
1	errors	15.5	1.3	8.3
	improvement	62%	59%	16%
0	errors	15.2	1.4	8.3
	improvement	62%	55%	18%

3.7 Sub-optimal Tightly Coupled

In the current low-end navigation product markets, it is a trend to integrate a GPS receiver and a low cost MEMS INS into one single application-specific integrated circuit (ASIC) chip. With the development of the MEMS inertial sensor technology, the cost is not a bottleneck, but the size of inertial sensor triads discourages such integration since the pitch gyroscope and the roll gyroscope occupy a relatively large space in an INS. To minimize the size of the INS, we are considering using a sub-optimal INS configuration with one heading gyroscope and two level accelerometers (1G2A) to achieve INS/GPS tightly coupled integration. 1G2A configuration is shown in Figure 3.10.

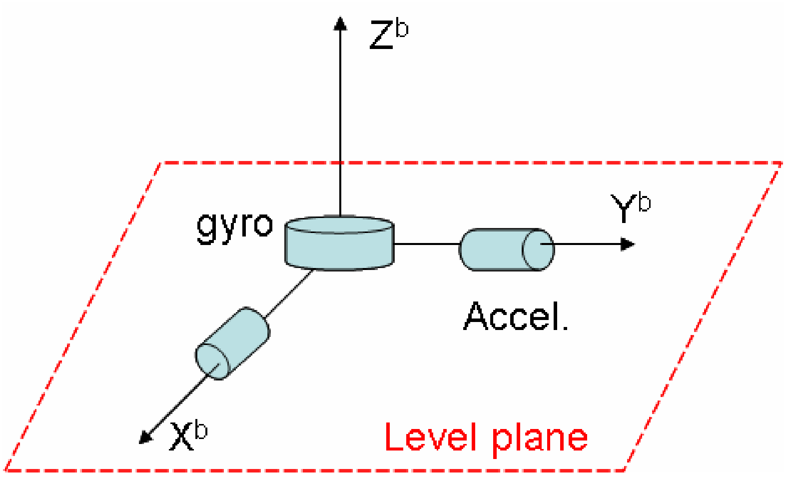

Figure 3.10: 1G2A sub-optimal INS configuration

In this configuration, the raw outputs from INS only include x-axis and y-axis accelerometer measurements in the b-frame (f_x^b and f_y^b) and z-axis gyro measurement in the b-frame (ω_z^b).The pseudo-signals of the missed inertial sensors (f_z^b and ω_x^b, ω_y^b) in 1G2A are generated to approximate a full INS configuration. The basic concept behind pseudo-signals generation algorithm is much similar to the INS simulator, which is described in the chapter 2.

Expanding the Equation (2.15) presented in the chapter 2, we have

$$f_z^b = \mathbf{R}_l^b(3,1)\cdot(-\omega_z^a V^N + \omega_y^a V^U) + \mathbf{R}_l^b(3,2)\cdot(\omega_z^a V^E - \omega_x^a V^U)$$
$$+\mathbf{R}_l^b(3,2)\cdot(\dot{V}^U(t) - \omega_y^a V^E + \omega_x^a V^N + g) + \delta f_z^b \qquad (3.59)$$

where

$\mathbf{R}_l^b(i,j)$ represents an element of $\mathbf{R}_l^b$ located on the $i-th$ row and the $j-th$ column.

g is the normal gravity;

$\begin{bmatrix} \omega_x^a \\ \omega_y^a \\ \omega_z^a \end{bmatrix} = 2\boldsymbol{\omega}_{ie}^l + \boldsymbol{\omega}_{el}^l$;

$\dot{V}^U(t)$ is the upward acceleration in the l-frame. Considering a limited dynamics in the land vehicle $(< g)$, it can be calculated by

$\dot{V}^U(t) \approx \dfrac{V^U(t-dt) - V^U(t-2dt)}{dt}$;

δf_z^b represents the modeled error of z-axis accelerometer pseudo-measurements, which is different from $\delta \mathbf{f}_{ib}^b$ presented in the Equation (2.15). This error comes from the approximation process in the pseudo-signal generation. A 1st order GM is used to model it.

Expanding the Equation (2.21), we have

$$\omega_x^b = \mathbf{R}_l^b(1,1) \cdot \omega_x^g + \mathbf{R}_l^b(1,2) \cdot \omega_y^g + \mathbf{R}_l^b(1,3) \cdot \omega_z^g + \omega_{lb,x}^b + \delta\omega_x^b \tag{3.60}$$

$$\omega_y^b = \mathbf{R}_l^b(2,1) \cdot \omega_x^g + \mathbf{R}_l^b(2,2) \cdot \omega_y^g + \mathbf{R}_l^b(2,3) \cdot \omega_z^g + \omega_{lb,y}^b + \delta\omega_y^b \tag{3.61}$$

where

$\begin{bmatrix} \omega_x^g \\ \omega_y^g \\ \omega_z^g \end{bmatrix} = (\boldsymbol{\omega}_{ie}^l + \boldsymbol{\omega}_{el}^l)$, and

$\delta\omega_x^b, \delta\omega_y^b$ represent the modeled errors of x-axis and y-axis gyros' pseudo-measurements. 1st order GMs are used to model them.

$\boldsymbol{\omega}_{lb}^{b}=\begin{bmatrix}\cos r & 0 & \cos p\sin r\\ 0 & 1 & \sin p\\ \sin r & 0 & \cos p\cos r\end{bmatrix}\begin{bmatrix}\dot{p}\\ \dot{r}\\ \dot{A}\end{bmatrix}$, which is already described in the Equation (2.22), where

$$\dot{r}(t)\approx\frac{r(t-dt)-r(t-2dt)}{dt} \text{ and } \dot{p}(t)\approx\frac{p(t-dt)-p(t-2dt)}{dt}.$$

To further explain the general algorithm of the pseudo-signal generation for 1G2A, Figure (3.11) presents the flow chart of 1G2A used in INS/GPS. It takes 100Hz INS and 1Hz GPS as an example. According to the flow chart, the algorithm implementation of 1G2A INS/GPS has the followed nine steps: 1) use the initial PVA information and zero attitude rate and zero vertical velocity rate to generate the first set of pseudo-signals based on the Equation (3.59) – (3.61); 2) combine the generated pseudo-signals and the measured real INS signals to form a full INS measurement; 3) perform INS mechanization to derive INS PVA; 4) predict state errors through EKF prediction and then correct INS PVA errors; 5) calculate attitude rate and vertical velocity rate by time differential based on the current PVA and the previous PVA; 6) generate the next epoch pseudo-signals based on the Equation (3.59) – (3.61); 7) repeat step 2 to step 6 till GPS measurement is ready; 8) EKF update using GPS information and correct INS PVA errors; 9) repeat step 7 and step 8.

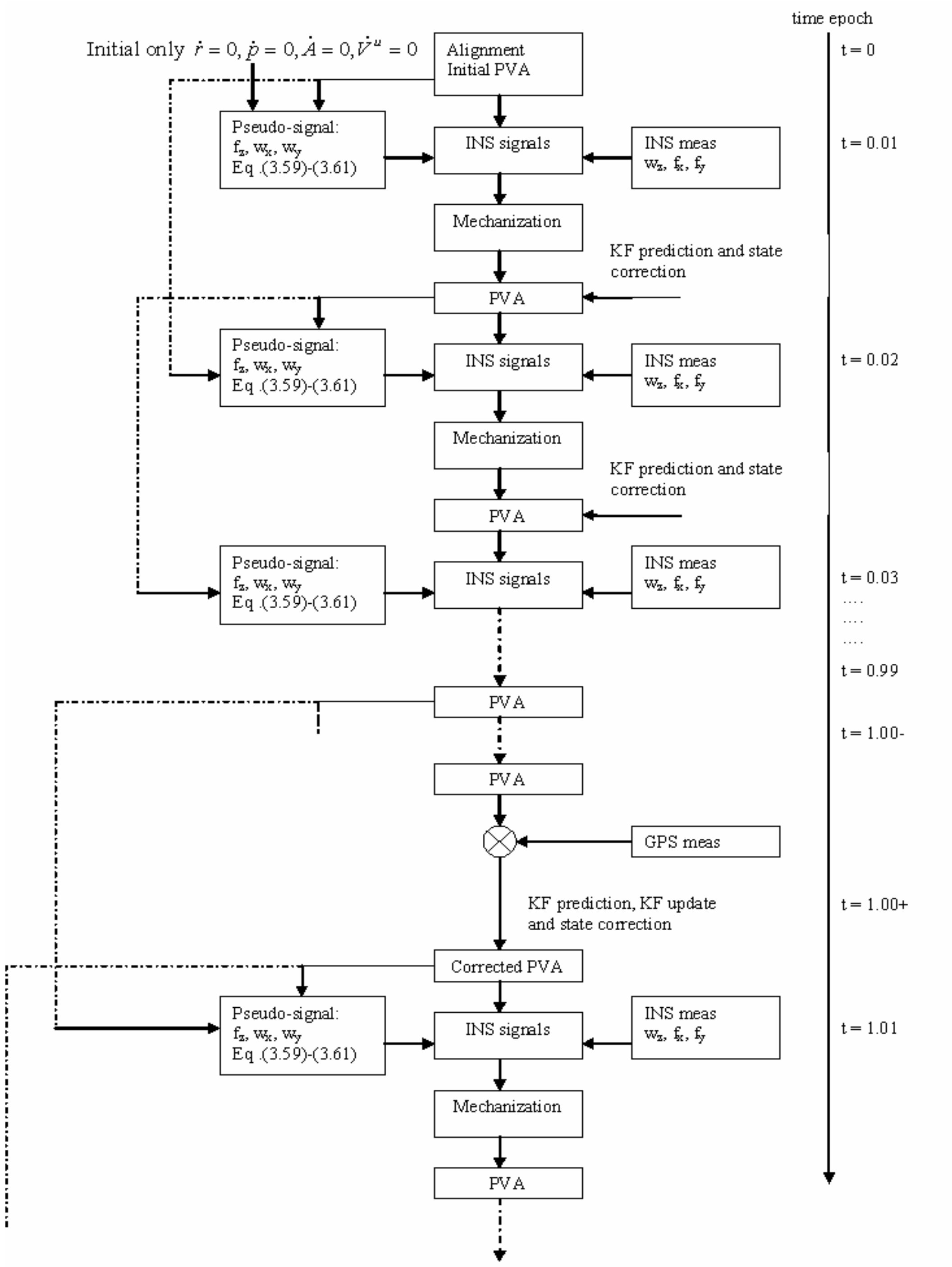

Figure 3.11: Flow chart of 1G2A INS/GPS using INS pseudo-signals

It should be noted that a very basic assumption of the above signal generation is that there are no dramatic change in pitch angle and roll angle during one GPS update cycle, so pitch rate and roll rate are small. In addition, the large noise covariance matrix for the pseudo-signals is recommended in the algorithm implementation because of the time differential approximation and the correlated signals.

Figure 3.12 shows the navigation errors of 1G2A sub-optimal INS configuration for the case of two satellites being tracked with non-holonomic constraint. Comparing Figure (3.12) with Figure (3.9), we should note that 1G2A has larger navigation errors during static periods than full-INS configuration. That is because 1) the attitude is hard to be observed directly through position and velocity measurements. The EKF converges slowly during the static periods due to the weak observability so that no sufficient correction information can be provided to the attitude drift; 2) in addition, the non-holonomic constraint takes effect on the level directions, but it does nothing along the vehicle's vertical axis. The errors of pitch and roll are smaller because there are coupled with the level (east and north) velocities (El-Sheimy, 2006), even though the couplings are weak. But the heading error is large; 3) furthermore, two satellites give a poor geometry. The EKF relies more on the prediction rather than the update under such a situation. The prediction only process for the MEMS grade INS results in large errors. However, combining the Equation (3.60), (3.61) and Equation (2.22) and checking with the vehicle's trajectory/motions shown in Figure (3.6), we can note that the small errors in pseudo signal generation will result in large inertial sensor errors. For example, 1° of heading error with 100Hz INS rate at 5° roll angle in the pseudo-signal generation process is roughly equivalent to a $1.7^{\circ}/s$ bias to the pseudo x-gyro. This bias contributes to the heading errors through $\mathbf{R}_b^l$. That is why a very large heading error is presented in the figure. In addition, similar to the heading error analysis during static periods, from the Equation (3.59), the z-axis accelerometer output is mainly determined by the coupling of the normal gravity and $\mathbf{R}_b^l$. For example, 1° of pitch error at 0° heading angle is roughly equivalent to a $17000\mu g$ bias to the pseudo z-axis, which is huge enough to form a peak at the 600-th second in the figure.

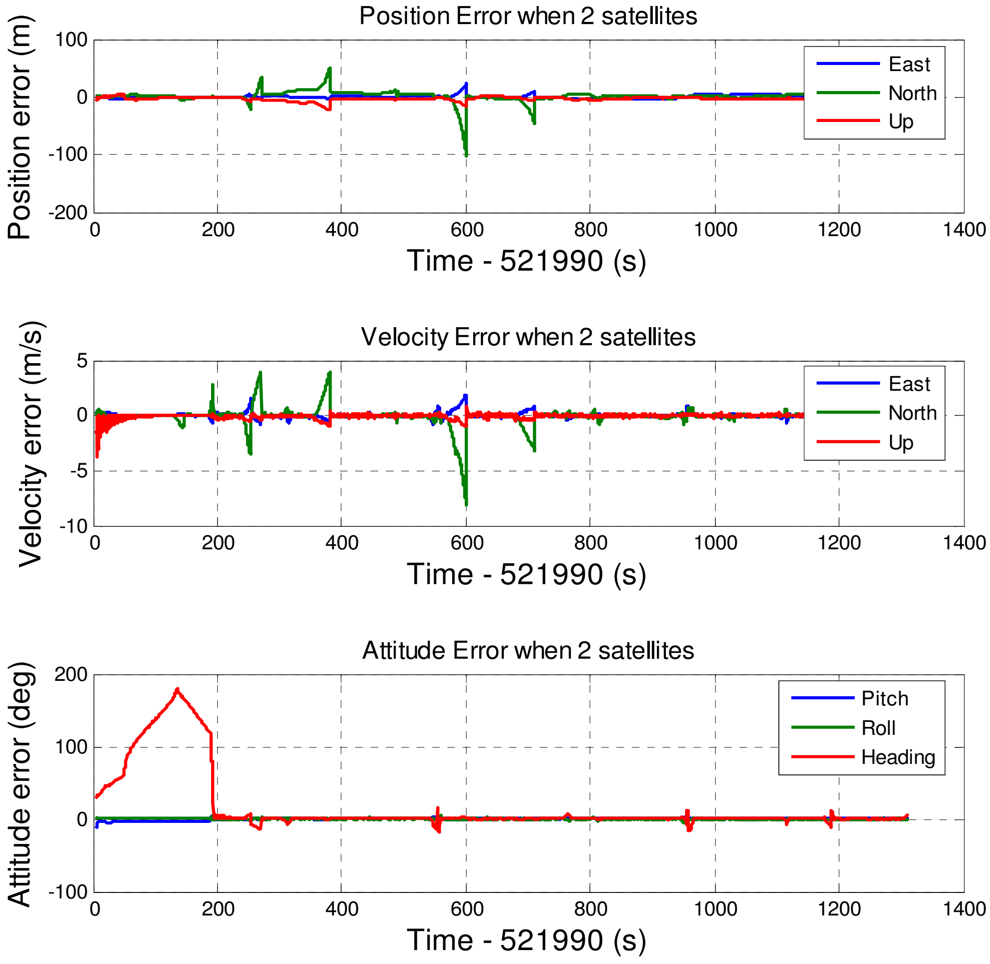

Figure 3.12: PVA errors for 2 satellites case (1G2A, non-holonomic)

Table 3.5: Errors comparison in 1G2A INS configuration with using non-holonomic

numbers of Satellites	$\delta r(m)$ (mean)	$\delta V(m/s)$ (mean)	$\lvert\delta A\rvert$(deg) (mean)
3	<7	<0.2	22.4
2	26.1	1.9	23.1
1	37.3	2.3	42.5
0	39.6	2.3	43.4

3.8 Summary

First, this chapter clearly defines the INS/GPS integration schemes, i.e. loose couple, tight couple and deep couple. Second, the chapter introduces the MEMS inertial sensor based INS and the estimation mathematical tool (discrete EKF) for the integration system. With derivations of INS errors and GPS errors, this chapter develops an EKF based MEMS INS/GPS tightly coupled integration algorithm. The state vector has 23 states related to INS and GPS system errors. The pseudorange and Doppler measurements from both INS and GPS are used as the observables for the EKF. Specifically, to improve the navigation accuracy for land vehicle application, one constraint was derived, namely the non-holonomic constraints. Furthermore, a pseudo-signal generation method is proposed in the last section of this chapter.

The results and analyses based on the field test data set reveal that 1) the tightly coupled INS/GPS can work well under the environment with fewer than four GPS satellites; 2) fewer satellites being tracked result in worse navigation performance due to the worse satellites geometry; 3) the receiver's clock errors' estimation are associated with both the vehicle's dynamics and the satellite geometry; 4) by using non-holonomic constraint for land vehicle application, the position accuracy can be improved by around 60%; 5) suboptimal INS/GPS tight integration with 1G2A INS configuration can maintain the system positioning error smaller than 7m, 27m, 38m, or 40m during 30s GPS signal outage environment, with 3, 2, 1 or 0 satellite(s) in-view, respectively.

Chapter 4 GPS Receiver Tracking Loop and Its Parameters

In a GPS receiver the signal is processed to obtain the required information, which in turn is used to calculate the user position. Therefore, at least two areas of discipline, receiver technology and navigation scheme, are employed in GPS receivers. This chapter investigates the signal processing of a software method based GPS L1 C/A receiver. It focuses on the receiver carrier tracking loop. Section 4.1 gives an overview of the GPS receiver signal processing. The received signals from RF to baseband are mathematically described. Section 4.2 investigates the operations of receiver signal tracking loops including accumulation and dump, discriminators and loop filters. In Section 4.3 the tracking capabilities of a 2nd order PLL are analyzed in details through simulated experiments.

4.1 GPS Receiver Signal Processing

4.1.1 GPS L1 Signals

This research is only about the current L1 C/A code in GPS system. Mathematically, L1 C/A code GPS signals arriving at antenna may be represented by (Raquet, 2006; Lachapelle, 2005):

$$r(t) = \sum_{k=1}^{m} s^k(t) + n(t) \tag{4.1}$$

where

$k = 1,2,\cdots m$ represents the number of satellites in view;

n(t) is the receiver noise;

$s^k(t)$ is the L1 C/A signal from k-th satellite. It can be expressed as:

$$s(t) = \overline{A}\,C(t)D(t)\cos[(\omega_0 + \omega_d)t + \phi_0] \qquad (4.2)$$

where

$\overline{A}$ is signal amplitude;

$C(t)$ is C/A PRN code modulation (±1);

$D(t)$ is 50 bps navigation data modulation (±1);

ω_0 is equal to $2\pi f_0$; carrier frequency $f_0 = 1575.42$ MHz for L1;

ω_d is the angular Doppler frequency due the LOS motions, clock drift and propagation delay;

ϕ_0 is the nominal (but ambiguous) carrier phase.

In order not to interfere with the existing terrestrial wireless communication and broadcast services, the currently received GPS signal power is set very low. The received GPS signals by an antenna combines signals from all satellites in view with noise, and the minimum specified received signal only carries 10^{-16} watts, i.e. -160 dBW, for the satellites located near the zenith or horizon (Lachapelle, 2005). In addition to this characteristically low signal power, the high chipping rate PRN code spreads the signal power over a wide bandwidth, thus resulting in a signal's power spectral density (PSD) below the usual ambient noise PSD level. The ambient noise can be approximately 60 (zenith) to 400 (5° elevation) times stronger than the C/A L1 signal from one satellite (Misra and Enge, 2001). Since the PSD of GPS C/A signals is overwhelmed by that of the noise, the GPS signal cannot be detected directly in L1 band, e.g. using classical tools such as an oscilloscope. The receiver antenna captures this tiny signal and converts it into the voltages and currents that the front-end can process.

Receiver performance is more dependent on a signal-to-noise ratio (SNR) than the absolute signal power (Raquet, 2006). SNR is a ratio of signal power to noise power as shown in Equation (4.3) (Tsui, 2000). The noise power depends on the processing bandwidth of the GPS receiver.

$$SNR = \frac{S}{N_0 2B} \tag{4.3}$$

where,

B is the single bandwidth of the filter in the receiver to remove the out of band noise (Raquet, 2006);

S is the signal power within the bandwidth of B_n;

N_0 is noise power density.

In practice, the ratio of total carrier power to the noise density C/N_0 in dB-Hz is the most generic representation of signal power as it is independent of the implementation of the receiver front-end bandwidth. The relationship of SNR and C/N_0 can be represented as (Lian, 2004):

$$SNR(dB) = C/N_0(dB - Hz) - B(Hz) \tag{4.4}$$

4.1.2 GPS Receiver Technology

The standard GPS receiver components can be broadly classified into one of the three categories (Ledvina, 2004; Lachapelle, 2005) 1) the radio-frequency (RF) front-end section; 2) the core intermediate frequency (IF) signal processing section; 3) the navigation signal processing section. The IF signal processing is the heart of a GPS receiver that performs most demanding tasks, a combination of hardware and software. Navigation processing generates position, velocity and time from pseudorange, phase and/or Doppler measurements. It has additional application specific software.

The generic architecture of a GPS receiver is illustrated Figure 4.1. The signals transmitted from the GPS satellites are gathered by an omni-directional antenna.most antenna are actually more hemi-spherial Through the receiver's FE unit the RF is amplified to proper amplitude and the frequency is down converted, filtered, and digitized to a desired IF signal. Typical GPS receivers have 8 to 12 channels. Each channel uses the same sampled IF data from the RF section. However, each channel locks onto a different satellite. The receiver has high-level executive software that controls which channels track which satellites (via unique C/A PRN code), when to declare if lock has been lost, and when to reacquire. It tracks a particular PRN code and can change tracked PRN while running. Each SV is tracked in one channel, even if more than one signal (C/A code, L1 P-code, L2 P-code) is tracked.

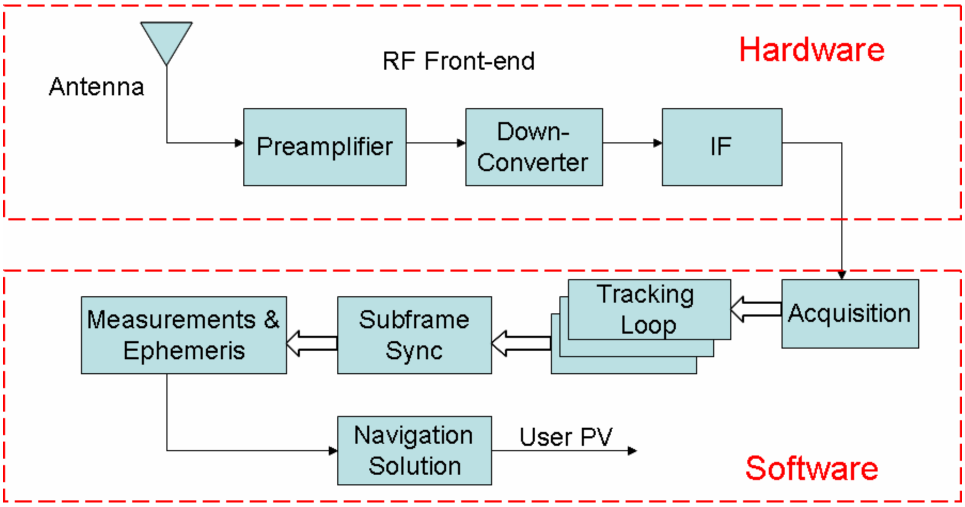

Figure 4.1: Generic diagram of a software based GPS receiver (After Tsui, 2000)

4.1.3 Front-End

An antenna receives the RF GPS signal and filters out the interferences such as signals outside the desired band and reflected signals of left hand circular polarization (Ray 2005). Then the signal is strengthened by a low noise amplifier (LNA) housed in the antenna, and is fed into the FE. The FE down-converts the signal from L band to IF and amplifies the signal to a workable level for digitization.

The FE of the receiver conditions the received signal described by equations (4.1) and (4.2). The FE must down convert the frequency by a factor of 100 to 1000 to a lower one, IF, which is more manageable by the rest of the receiver. Down conversion from RF to IF is mathematically based on the trigonometric identity. It is accomplished by mixing the incoming signal and noise with a local oscillator (LO) signal with the angular frequency of ω_1. This process is illustrated in the first part of Figure 4.2 (Charkhandeh, 2007). The IF signals can be expressed as (Raquet, 2006):

$$s_{IF}(t) = \overline{A}C(t)D(t)\cos[(\omega_{IF} + \omega_d)t + \phi_0] + n_{IF}(t) \quad (4.5)$$

where

$\omega_{IF} = \omega_0 - \omega_1$ is the angular IF frequency, equal to $2\pi f_{IF}$;

f_{IF} is determined by the receiver designer's frequency plan;

$n_{IF}(t)$ is the band-limited ambient/thermal noise with an expression of (Viterbi 1966).

$$n_{IF}(t) = n_c(t)\cos\omega_{IF}t + n_s(t)\sin\omega_{IF}t \quad (4.6)$$

where $n_c(t)$ and $n_s(t)$ are white noise processes inside the bandwidth of f_{IF} Hz.

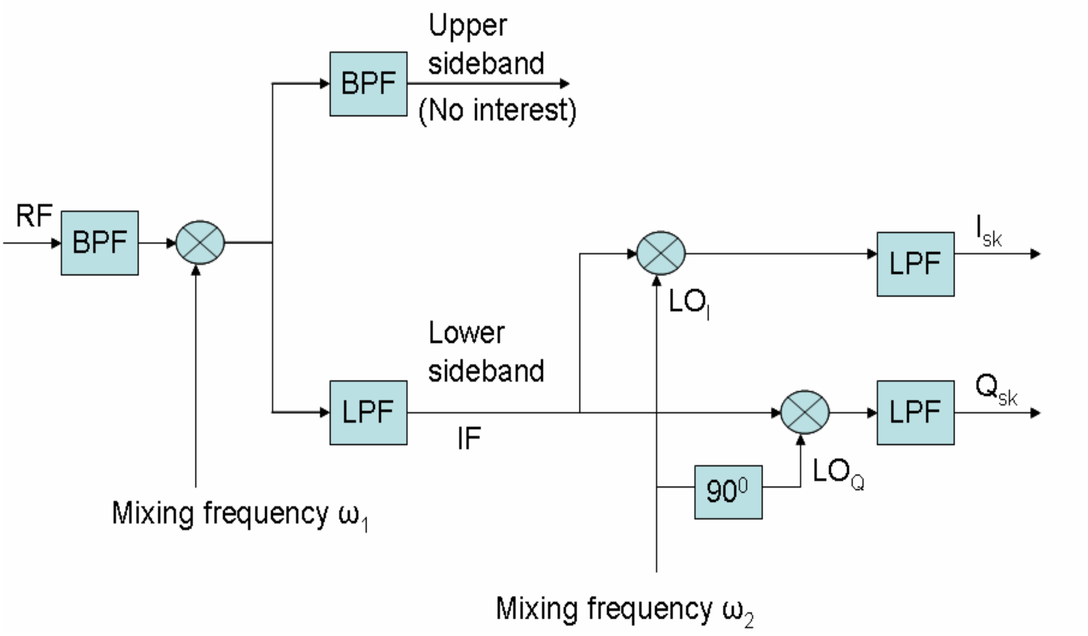

Figure 4.2: Downconvert RF to IF and IF to baseband (After Charkhandeh, 2007)

4.1.4 IF Signal Processing

The overall objectives of GPS IF signal processing is to generate a local signal that exactly matches the incoming signal. If this could be done perfectly, then measurements could be found using the local signal only (since it is known). The received signal described by equation (4.5) is then split into two branches. One branch is multiplied by the in-phase mixing carrier, and the other one is multiplied by a quadrature-phase mixing carrier (shifted by 90°, as compared to the in-phase carrier replica), as shown in the second part of Figure 4.2. This processing wipes off the signal carrier and downconverts the signal to baseband. The in-phase and quadrature-phase mixing signals are $\mathrm{LO_I}$ and $\mathrm{LO_Q}$, respectively, as:

$$LO_I = \sqrt{2}\cos(\omega_2 t) \qquad\qquad LO_Q = \sqrt{2}\cos(\omega_2 t + \pi/2) = -\sqrt{2}\sin(\omega_2 t)$$

Therefore, the sampled in-phase signal and quadrature signal can be written as (Raquet, 2006):

$$I_{sk} = \frac{\bar{A}}{\sqrt{2}} C_k D_k \cos(\phi_k) + n_{Isk} \tag{4.7}$$

$$Q_{sk} = \frac{\bar{A}}{\sqrt{2}} C_k D_k \sin(\phi_k) + n_{Qsk} \tag{4.8}$$

with the phase of

$$\phi_k = (\omega_B + \omega_d)t_k + \phi_0 \tag{4.9}$$

where

ω_B is the baseband angular frequency of the signal, and $\omega_B = \omega_{IF} - \omega_2$

4.1.4.1 Acquisition

The baseband samples are correlated with the local carrier replica (Doppler removal) and the local code replica (correlation), and passed through the accumulation and dump filter to achieve the coherent units, which are fed into the receiver's acquisition and tracking process. Acquisition is the first step in processing the sampled GPS baseband data. This process separates the signals from satellites in view and allocates each satellite's signal in one of receiver's parallel channels since those coherent units include the information for all the visible satellites. The three key parameters to be determined during acquisition are the C/A codes (for the satellites in view), their respective C/A code phases and carrier frequencies (with individual Doppler shifts) (Lachapelle, 2005). Once the presence of signals is detected, the resulting information is used by a bank of signal tracking components to track the signal.

To acquire a signal, the receiver generates a replica of the known C/A code, and attempts to align it with the incoming code by sliding the replica in time and computing the correlation. From the auto-correlation property of the signal, the correlation function exhibits a sharp peak when the code replica is aligned with the code received from the satellite (Dong, 2003; Gregory and Garrison, 2004). The maximum uncertainty in matching the replica with the incoming code is limited to only 1023 code chips. The acquisition fundamentals described in many literatures, e.g. Kaplan (1996), Lin (2000), Psiaki (2004), and the reader can refer to these references for details.

4.1.4.2 Tracking

After signal down conversion and acquisition, the sampled GPS baseband signal is sent into the signal tracking loops for carrier phase and code delay coherent tracking to recover the incoming signal accurately (Kaplan, 1996). Typically, the frequency and range of incoming signals are constantly changing. Satellites dynamics cause Doppler changes up to $0.9 Hz / s$ and code phase offset changes up to $3 chips / s$ (Tsui, 2000). The LOS receiver dynamics between the satellite and receiver antennas cause additional Doppler changes. High accelerations cause faster change in Doppler. In addition, the LO used in the RF front end will have an associated frequency drift. Therefore, the tracking process not only refines the rough estimates from the acquisition, but follows the carrier Doppler and the code offset for each visible satellite due to the LOS motion between the satellite and the receiver and the receiver's clock drift. Unfortunately, a pure PLL can not distinguish the LOS motion and the clock drift.

To track an incoming GPS signal, the replica of the local carrier frequency and code offset needs to be matched with that. There are two or three tracking loops in each channel: the DLL that tracks the spreading code delay; the PLL that synchronizes the carrier phase, and/or the frequency-locked loop that tracks the signal Doppler. These loops are normally coupled together, as shown in Figure 4.3.

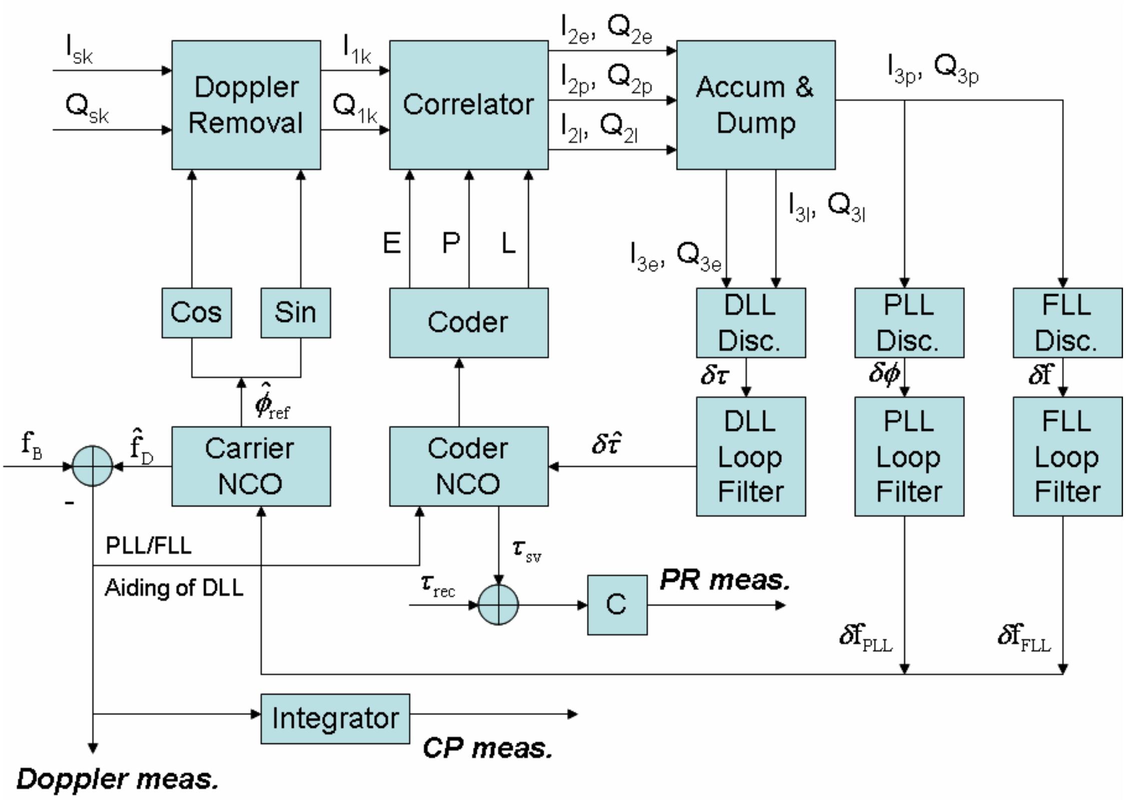

Figure 4.3: Block diagram of tracking Loops (After Raquet, 2006)

As shown in the Figure 4.3, the inputs at Doppler removal unit are the baseband samples I_{sk} and Q_{sk} described in Equations (4.7) and (4.8). Doppler removal is actually a process of carrier removal since it removes the entire Doppler plus carrier at baseband frequency. The output signals of Doppler removal can be written as,

$$I_{1k} = \frac{\overline{A}}{\sqrt{2}} C_k D_K \cos(\phi_k - \hat{\phi}_{ref}) + n_{I1k} \tag{4.10}$$

$$Q_{1k} = \frac{\overline{A}}{\sqrt{2}} C_k D_K \sin(\phi_k - \hat{\phi}_{ref}) + n_{Q1k} \tag{4.11}$$

Based on the Figure 4.3 and Equation (4.9), we know that the output frequency after Doppler removal is the difference between the true Doppler (f_D) and the receiver's best estimated Doppler ($\hat{f}_D$). If $\hat{f}_D$ is accurate enough, we have $\hat{\phi}_{ref} \approx \phi_k$ (ignoring nominal phase error temporary). Therefore,

$$I_{1k} = \frac{2}{\sqrt{A}} C_k D_K + n_{I1k} \tag{4.12}$$

$$Q_{1k} = 0 + n_{Q1k} \tag{4.13}$$

It indicates that the navigation data are only presented on the in-phase signal when the signal is well tracked. In a traditional receiver, $\hat{f}_D$ is acquired by the PLL or FLL. However, as we shall soon discover, it is always difficult to obtain an accurate $\hat{f}_D$ in the weak signal environment. $\hat{f}_D$ with large errors will result in a degraded tracking performance, even loss-of-lock of GPS signals. Therefore, an external $\hat{f}_D$ with high accuracy from INS is considered aiding PLL during weak GPS signal period to maintain the small difference between the local generate phase $\hat{\phi}_{ref}$ and the incoming signal phase ϕ_k. That is the theoretical motive of this research work.

After Doppler removal, I_{1k} and Q_{1k} are still overwhelmed by the noise and modulated by C/A code. The power of the signals is distributed over a rather wide bandwidth of 1.023 MHz. They can provide us none of the useful information. Correlators in Figure 4.3 simply multiply I_{1k} and Q_{1k} by receiver generated codes to produce I_{2km} and Q_{2km} (Ma, 2004)

$$I_{2km} = \frac{\overline{A}}{\sqrt{2}} C_k C_{kr,m} D_K \cos(\phi_k - \hat{\phi}_{ref}) + n_{I2k} \tag{4.14}$$

$$Q_{2km} = \frac{\bar{A}}{\sqrt{2}} C_k C_{kr,m} D_K \sin(\phi_k - \hat{\phi}_{ref}) + n_{Q2k} \tag{4.15}$$

where

$C_{kr,m}$ are the local generated codes; m can be e (early), p (prompt) and l (late).

The cross-correlation function of codes is

$$\mathbf{E}[C_k C_{kr,m}] = R(\tau_{km}) \approx \begin{cases} 1-|\tau_{km}|, & |\tau_{km}| \le 1 \\ 0, & |\tau_{km}| > 1 \end{cases} \tag{4.16}$$

The precise pseudorange and carrier phase measurements can be derived from the tracking loops. At the same time, good tracking ensures correct demodulation of ephemeris which inherits the satellites' position and velocity information. Once a receiver keeps tracking the carrier phase and code offset of the incoming signal, it starts to detect the bit boundary in a process named bit synchronization and to estimate C/N_0. The estimation of C/N_0 is necessary because the C/N_0 is associated with the quality of tracking. The estimated C/N_0 decreases rapidly once the receiver loses lock. Measurement errors, satellite motion and receiver motion all contribute to making the tracking process more difficult (Lachapelle, 2005). The tracking section of a receiver tries to minimize the tracking errors over time by monitoring them and adjusting how the internal signal is generated.

4.1.4.3 Measurement Derivation

The carrier Doppler and phase measurements can be acquired from PLL directly. The pseudorange measurement has to be derived after the navigation data decoding. The pseudorange measurement derivation is to find the transmission time at the time of measurement.

Assuming that the tracking loops are locked (i.e. in steady state), the navigation data will be present in the in-phase arm of the Costas PLL (Kaplan, 1996). Demodulated navigation data recovered from the in-phase arm of the carrier tracking loop PLL combined with the code tracking loop measurements provide the necessary components to compute a navigation solution. However, bit and frame synchronization operations are required before any useful navigation information can be extracted from the raw navigation data. There are several methods that are used for data bit synchronization. One of the most common approaches is the histogram method (Lachapelle, 2005). The decoded data bits must be searched for a possible preamble and if successful, a parity check is performed, and data words are decoded and used in the calculation of a navigation solution. The parity check is to confirm that the demodulation process is free from errors. Once the resulting data passes through the check successfully, it is compiled into a set of meaningful parameters necessary for positioning computation.

4.1.5 Navigation Solution

In a GPS receiver, a navigation algorithm combines GPS raw measurements from the signal processing with the GPS satellite orbit data to estimate position related parameters. Fundamentally, a navigation solution is an estimate of the user's position and any other required parameters. Normally at least 4 satellites are necessary for three-dimension (3D) positioning. An estimator is used to estimate the required parameters. The typical estimated states of a GPS receiver are three position components, the receiver clock bias and the clock drift. The velocity is often added in dynamic applications.

In a tight INS/GPS integration system, as the INS provides most navigation information, only the receiver clock bias and the clock drift are needed for the estimator.

4.1.6 Receiver Oscillator

The oscillator (OSC) is a core component to drive the receiver to operate properly. OSCs can be classified into quartz crystal and atomic standard. Allan (1987) and Gierkink (1999) have described the OSCs' behaviour in detail. Compared with crystal OSCs, the atomic OSCs demonstrate an improvement in accuracy by about 2 to 3 orders and in aging by about 1 to 2 orders (Vig, 1992).

OSC provides a basic reference frequency, on which a frequency synthesizer generates all the local frequencies for both the RF FE and the signal processor. The frequency synthesizer is a PLL that forces the feedback frequency to lock on the reference frequency. The output frequency relates with the feedback frequency by a frequency divider; therefore by adjusting the parameters of the divider, one can generate the required output frequency. In conclusion, a high quality OSC can shorten the time to acquisition, improve the tracking capability and ambiguity resolution, and increase the reliability and redundancy (Gebre-Egziabher et al, 2005; Yu, 2006). However the significant cost and power consumption restricts the use of high quality OSC in commercial applications (Parkinson and Spiller, 1996).

The receiver OSC timing jitter, is of particular importance for satellite navigation systems for evaluating and assessing the accuracy, availability, and capability the system can achieve (Chaffee, 1987; Zucca and Tavella, 2005). OSC timing error originates from the oscillator's deviation from clock's nominal frequency. To mitigate the crystal OSC oscillating deviation originating from the fluctuation of temperature, one can either compensate for the temperature variation or mount the OSC in a temperature-stable environment; the former technique is the basis for the temperature controlled crystal OSC (TCXO) and the latter method is used in an oven controlled crystal OSC (OCXO). Oscillators used in GPS receivers must be reasonably accurate and inexpensive. To this end, GPS receivers usually employ TCXO. The OSC's frequency fluctuation is classified into systematic (deterministic) and random variations. Systematic variation of the OSC's periodicity is associated with the fluctuations external to the OSC circuit and can be minimized by applying appropriate circuit techniques (Chaffee, 1987; Yu 2006).

The random variations result from the noise, produced in active and passive components of the OSC circuit that modulates the frequency of oscillation. The random fluctuations of the receiver's clock are accommodated in the received IF signal. The Allan variance is commonly used to evaluate the random part of the frequency stability of an OSC. The oscillator's instability can be suitably modeled by the random processes satisfying stochastic differential equation (Davis et al., 2005; Zucca and Tavella, 2005); this model is of particular importance to evaluate the impact of clock noise on the receiver's tracking performance, to predict and characterize clock behavior, and to replicate clock data using filtering techniques (e.g. the KF). Yu (2006) uses an KF based method characterizing the OSC behaviors. According to the results in Yu (2006), the stability of an OSC can be evaluated over short-, medium-, and long-term intervals. Although oscillator performances for long-term intervals are significantly different for different oscillators, the stability performance of TCXO is the same or better than that of atomic standards for short-term intervals. The carrier tracking update rate for a GPS receiver is always less than 20 ms; as a result, the tracking jitter by phase noise is associated with the short-term stability of the operating oscillator. The root of Allan variance of a TCXO over 0.1s is typically 10^{-10} (Raquet, 2006).

4.2 Tracking Loops

4.2.1 Accumulation and Dump

After the correlator, the correlated in-phase signal I_{2km} and quadrature-phase signal Q_{2km} are still buried in noise. They should pass through the accumulation and dump filter to achieve the coherent units. Accumulation and Dump, shown in Figure 4.3, effectively filters out additional noise as a lowpass filter actually to increase the ratio between the signal strength and noise. It is also named pre-detection integration. Pre-detection integration, discriminator and loop filter typically characterize the receiver tracking loops (Kaplan, 1996). In pre-detection integration, a total of M_E samples are accumulated over T_{COH} seconds. This integration is normally the first point in the receiver where the signal is finally higher than the noise.

The pair of I and Q takes the analytical form of (Raquet, 2006; Yu, 2006)

$$I_{v,k} = \frac{\overline{A}}{\sqrt{2}} M_E \frac{\sin(\pi\delta f_k \cdot T_{COH})}{\pi\delta f_k \cdot T_{COH}} R_v(\tau_k) D_{m,k} \cos(\pi\delta f_k \cdot T_{COH} + \Delta\phi_k) + n_{I,v,k} \qquad (4.17)$$

$$Q_{v,k} = \frac{\overline{A}}{\sqrt{2}} M_E \frac{\sin(\pi\delta f_k \cdot T_{COH})}{\pi\delta f_k \cdot T_{COH}} R_v(\tau_k) D_{m,k} \sin(\pi\delta f_k \cdot T_{COH} + \Delta\phi_k) + n_{Q,v,k} \qquad (4.18)$$

where

v	could be early (*e*), prompt (*p*), and late (*l*) version of the locally-generated PRN samples;
T_{COH}	represents the COH accumulation interval;
M_E	is number of samples per COH accumulation segment, equal to T_{COH} / T_s, where $T_s = 1/(sampling\ rate)$ is the sampling period;
$D_{m,k}$	is the data bit, ± 1, over the k-th correlation interval. $m = \lfloor t_j / T_b \rfloor$ indicates the index of the data bit, where T_b is the data bit period of 20 ms and t_j is the start sample time for the k-th COH accumulation. $\lfloor x \rfloor$ is the maximum integer number no greater than x and $k = \lfloor t_j / T_{COH} \rfloor$ is the index of the COH accumulation interval;
δf_k	denotes the frequency error between the incoming samples and the local carrier replica over the *kth* correlation interval, and assuming constant frequency error over integration interval;
$R_v(\cdot)$	is the filtered normalized autocorrelation for the v correlator, depicted by the Equation (4.16);
τ_k	is the timing error over the correlation interval;
$\Delta\phi_k$	is the initial phase misalignment at start of integration, which is equation to $\phi_k - \hat{\phi}_{ref}$ and assumed as a constant over one integration interval;

$n_{I,v,k}$ represents the additive noise at in-phase arm for the v correlator, obeying the $N\left[0,\frac{M_E\sigma_s^2}{2}\right]$ distribution, where $N[\bullet,*]$ represents Gaussian distribution with expectation of $\bullet$ and variance of $*$. σ_s^2 is the variance of the noise released from the analog to digital converter, i.e. $\sigma_s^2 = N_0 / T_s$, N_0 is the received noise density;

$n_{Q,v,k}$ is additive noise at quadrature-phase arm for the v correlator, which shares the same distribution as $n_{I,v,k}$, but is independent of $n_{I,v,k}$;

$R_v(\tau_k)$ and $\frac{\sin(\pi\delta f_k \cdot T_{COH})}{\pi\delta f_k \cdot T_{COH}}$ each have a maximum amplitude of 1 when τ_k and δf_k take on the value of zero. This pair of equations is frequently used in the followed sections. The performance analysis of PLL is based on these two equations.

4.2.2 Discriminator

Whatever carrier tracking or code tracking method is used, the loop is required to correctly measure the misalignment of code/carrier phase. The discriminator, shown in Figure 4.3 is a key component in measuring the misalignments for both code and carrier tracking loops. COH units are used by the discriminator to measure the local estimation mismatches.

There are two types of DLL discriminators, i.e. coherent and non-coherent (Raquet, 2006). Due to the requirement of phase lock, the coherent discriminator is only used in some simple receivers to reduce the number of correlators. Non-coherent discriminators are typically used in commercial receivers since they do not require phase lock. That means the signal power can be in-phase or quadrature portion of the signal. For this reason, only non-coherent discriminators are discussed and implemented in this dissertation. The code mismatch between the incoming and the local generated is calculated based on DLL discriminator algorithm. The early and late COH I and Q components are variables in calculations. Under perfect code alignment, the early correlation I_E/Q_E is an image of the late one I_L/Q_L with respect to the prompt correlation I_P/Q_P. Early and late samples herein are both 0.5 chip off from the prompt. The difference between the early and late correlation reflects both magnitude and “direction” of the code phase mismatch, which is illustrated by Figure 4.4 according to equation (4.16). In this case, we assume the code phase mismatch is 0.3 chip and that the correlator spacing is 0.5 chip. Obviously, the early and late correlations are not balanced once the code asynchronism occurs. A negative difference controls the coder to lag the phase (Yu, 2006). The early minus late correlation analytically forms the function of the discriminator.

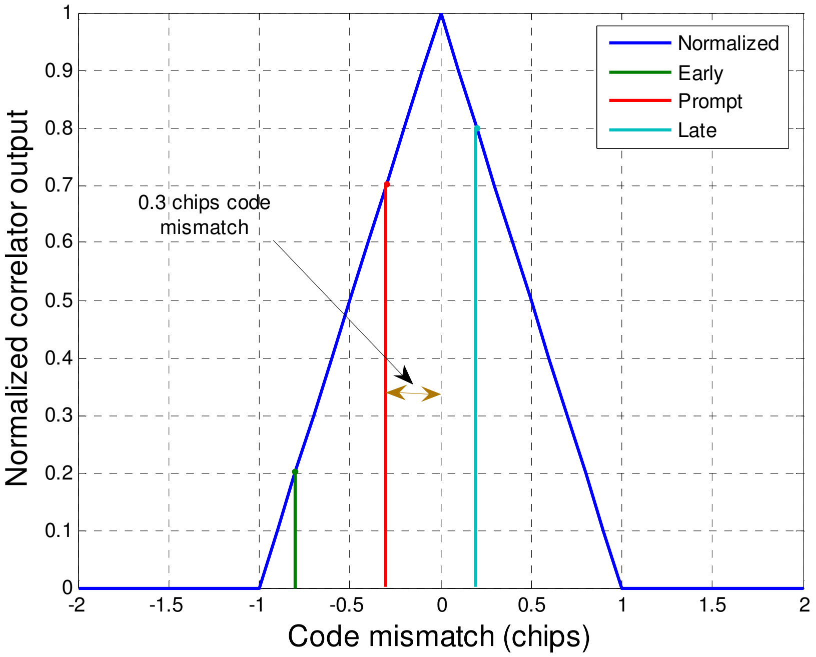

Figure 4.4: Code mismatch vs. early, prompt, and late correlations

Table 4.1 gives four well-known DLL discriminator recommended by Kaplan (1996) and Raquet (2006). $\delta\tau$ is the input code error of discriminator in this table. Figure 4.5 presents the comparison of four types of discriminators. The normalized E-L envelope discriminator described below is selected as the default one since it is good within +/- 1.5 chips errors for a early-late Correlator spacing of 1 chip, and its linear operation region is wider than other types of discriminators.

Table 4.1: DLL Discriminator

Discriminator Algorithm	Output code error ($\lvert\delta\tau\rvert \le 0.5$)
Dot product power $(I_E - I_L)I_P + (Q_E - Q_L)Q_P$	$2\delta\tau(1-\lvert\delta\tau\rvert)$
Early minus late power $\frac{1}{2}\left[(I_E^2+Q_E^2)-(I_L^2+Q_L^2)\right]$	$\delta\tau$
Early minus late envelope $\frac{1}{2}\left[\sqrt{I_E^2+Q_E^2}-\sqrt{I_L^2+Q_L^2}\right]$	$\delta\tau$
Normalized early minus late envelope $\frac{1}{2}\frac{\sqrt{I_E^2+Q_E^2}-\sqrt{I_L^2+Q_L^2}}{\sqrt{I_E^2+Q_E^2}+\sqrt{I_L^2+Q_L^2}}$	$\delta\tau$

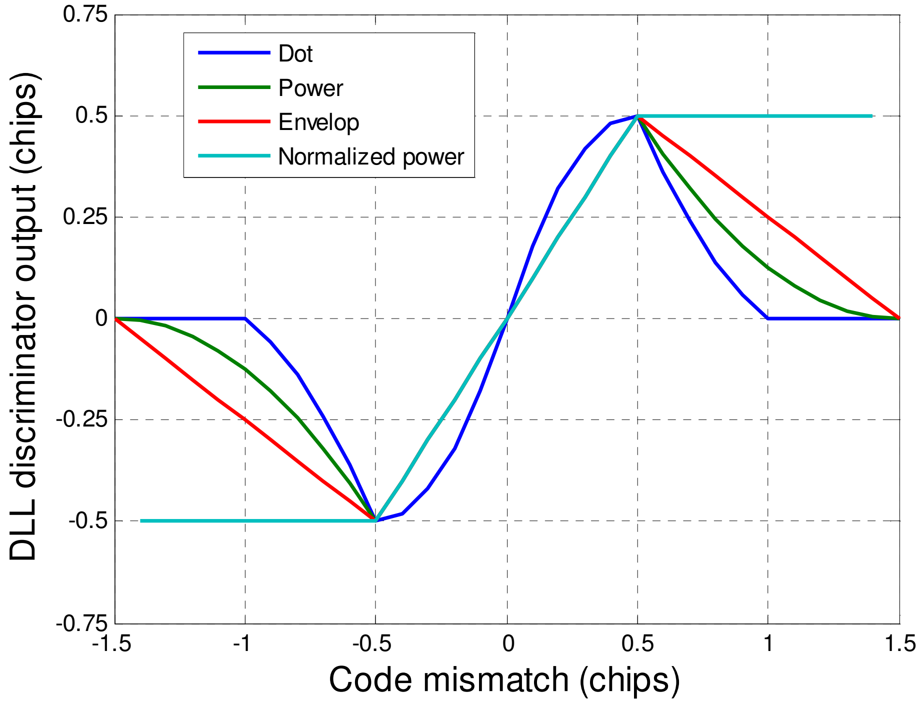

Figure 4.5: DLL discriminator comparisons

The carrier loop discriminator defines the type of tracking loop as a PLL, a Costas PLL or a FLL. PLL and Costas loops generate the phase error while FLL produces the frequency error. The FLL is easier to acquire lock, but the tracking result of the FLL is much noisier than that of the PLL (Yu, 2006). PLL and Costas PLL loops are more accurate, with the cost of being more sensitivity to dynamics. The Costas PLL loop is insensitive to 50-Hz data modulation in GPS signal therefore it is commonly used in GPS receivers. Costas PLL loops can be used to detect the bits in satellite data message stream. The in-phase prompt samples COH I_P can be accumulated for the duration of one data bit (20 ms) and the sign of the result is the data bit. The 180° phase ambiguity in Costas PLL can be corrected during the frame synchronization process (Tsui, 2000; Charkhandeh, 2007). The following PLLs are all referring to the Costas PLL. To produce the phase misalignment, the prompt correlations for current and previous epochs are used in following Costas PLL discriminators (Kaplan, 1996) that are listed in Table 4.2. $\delta\phi$ is the input phase error of discriminator in this table. Figure 4.6 presents the comparison of four types of PLL discriminators. Results reveal that all outputs repeat at 180° degree interval so as to insensitive to 180° phase reversals from navigation data. Most discriminators are approximately linear within $\pm 30^{\circ}$. The arctangent discriminator described below is selected as the default one since it its linear operation region is wider than other types of discriminators and it is optimal at high and low SNR (Raquet, 2006).

Table 4.2: PLL Discriminator

Discriminator Algorithm	Output phase error
$sign(I_P)\cdot Q_P$	$\sin(\delta\phi)$
$I_P \cdot Q_P$	$\sin(2\cdot\delta\phi)/2$
Q_P / I_P	$\delta\phi$
$a\tan(Q_P / I_P)$	$\delta\phi$

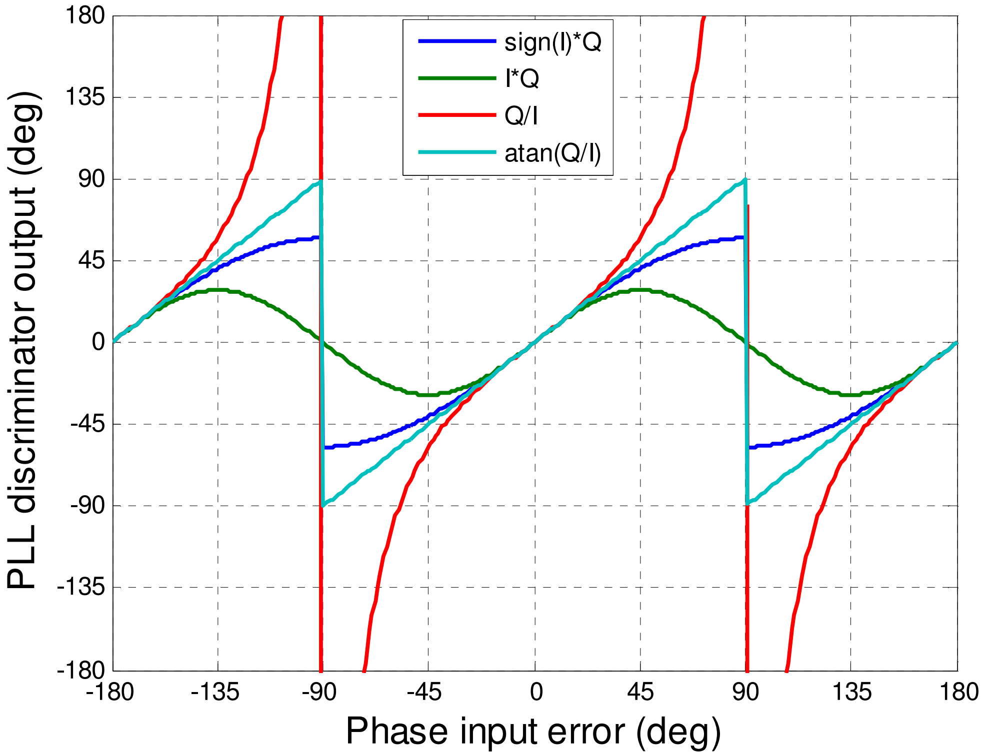

Figure 4.6: PLL discriminator comparisons

4.2.3 Loop Filter

To improve the accuracy of the error estimates, the raw measurements output by the discriminator are fed into a low pass filter. This low pass filter is dedicated to reduce noise, generate an accurate estimate of the desired signal. A very brief description of the filters used in typical GPS receivers is given in this section. Table 4.3 (Kaplan, 1996) summarizes the characteristics of some available loop filters. In the table, ω_0 is the loop's nature frequency, and a, b are related parameters and R is the LOS vector.

Table 4.3: Characteristics of loop filters

Loop order	Noise Bandwidth Bn (Hz)	Filter parameters	Characteristics
First	$\frac{\omega_0}{4}$	ω_0 $B_n = 0.25\omega_0$	Used in aided code loops. Unconditionally stable at all noise bandwidths
Second	$\frac{\omega_0(1+a_2^2)}{4a_2}$	$\omega_0^2, a_2 = 1.414$ $B_n = 0.53\omega_0$	Used in aided and unaided carrier loops. Unconditionally stable at all noise bandwidths
Third	$\frac{\omega_0(a_3b_3^2 + a_3^2 - b_3)}{4(a_3b_3 - 1)}$	ω_0^3 $a_3 = 1.1, b_3 = 2.4$ $B_n = 0.7845\omega_0$	Sensitive to jerk. Used in all unaided carrier loops. Remains stable at $B_n \le 18Hz$

The type of loops chosen depends on the desired tracking performance, desired noise bandwidth and anticipated dynamics. An analog filter normally needs to be converted to digital form for real implementation by using bilinear transform. Figure 4.7 gives a pair of a generic 2nd order loop filter's analog and digital forms.

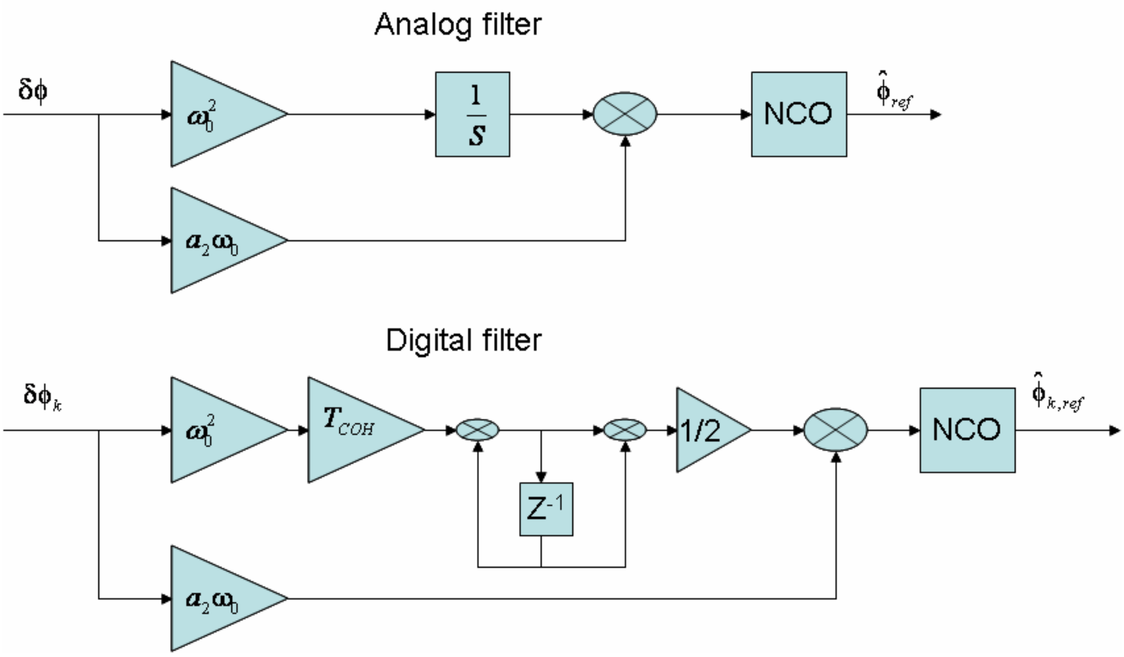

Figure 4.7: Block diagrams of 2nd order loop filter (After Kaplan, 1996)

According to the above figure, the z-domain transfer function of the loop filter can be expressed as

$$D(z) = \frac{(\omega_0 T_{COH}/2 + a_2\omega_0)z + (\omega_0^2 T_{COH}/2 - a_2\omega_0)}{z-1} \tag{4.19}$$

where, ω_0 and a_2 are determined by the loop filter parameters and T_{COH} is the pre-detection integration time (PIT).

4.3 PLL Performance and Its Parameters

Compared with the DLL, the carrier tracking loop is the weaker link in the operation of GPS signal tracking and more vulnerable to loss of lock. That is because the carrier wavelength is much shorter than the chip length. Furthermore, the carrier loop needs to track all dynamics while the code loop needs only to track the dynamic difference between carrier loop and code loop when carrier aiding is applied to code loop (Lian, 2004). We are focusing on the PLL in this section. A typical simplified PLL is illustrated in Figure 4.8.

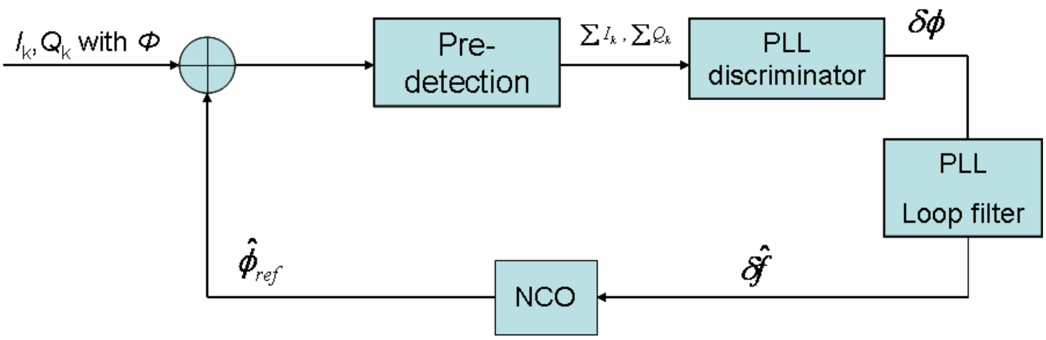

Figure 4.8: Simplified PLL

Simply speaking, the functionality of the pre-detection integration process is to increase the incoming signal strength, which is executed in an "integrate and dump" operation. The discriminator outputs phase errors between the true carrier and the replicated in-phase carrier. As mentioned before, the arctangent discriminator is used herein. The loop filter is to reduce phase error noise with the desired dynamics in order to produce an accurate estimate of the incoming signal at its output. According to the Figure 4.8, the Figure 4.9 presents a linearized loop model implementation.

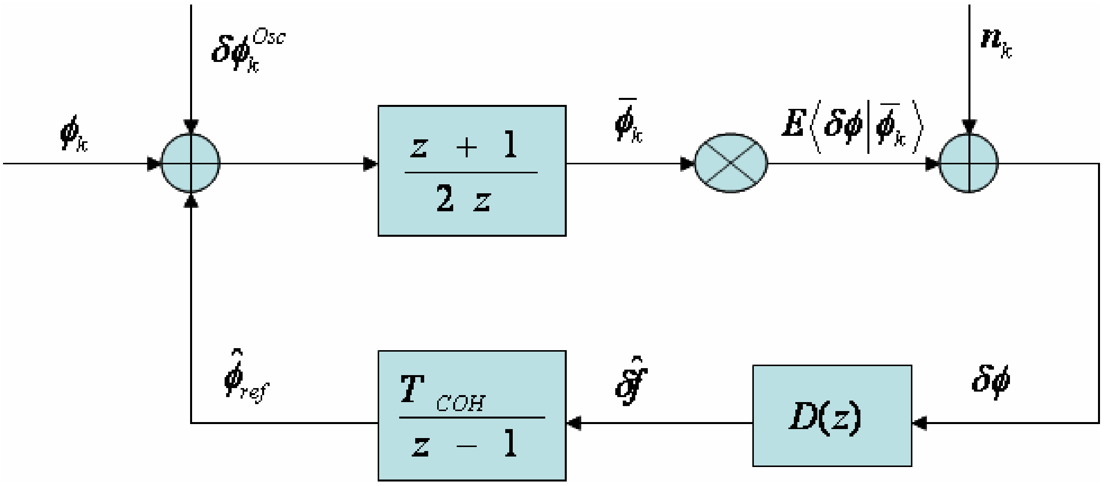

Figure 4.9: Linearized discrete model for a PLL (After Yu, 2006)

where,

ϕ_k	is the carrier phase of the received sample;
$\hat{\phi}_{ref}$	is the local estimate of ϕ_k ;
$\delta\phi_k^{OSC}$	models the phase noise induced by the instability of OSC;
$\frac{z+1}{2z}$	represents the “pre-detection” unit (Humphreys et al., 2005);
$\frac{T_{COH}}{z-1}$	represents the NCO unit since NCO acts as an integrator;
n_k	is noise associated with the normalized additive noise at COH I and Q, illustrated in equations (4.17) and (4.18). The variance of n_k depends on the type of discriminator. Nonlinear operation of the discriminator amplifies the noise power, and thus excites a larger carrier tracking error;
$E\langle\delta\phi|\bar{\phi}_k\rangle$	denotes the response of the discriminator;

$\delta\phi$ is the raw measured, which is much noisier because of a wider noise bandwidth of $1/T_{COH}$; subsequently this error signal is de-noised by the loop filter $D(z)$ from which the output is used to drive the NCO.

The loop transfer function can be derived as

$$H(z) = \frac{(\frac{Z+1}{2z})(\frac{T_{COH}}{z-1})D(z)}{1+(\frac{z+1}{2z})(\frac{T_{COH}}{z-1})D(z)} \tag{4.20}$$

The loop noise transfer function is

$$H_n(z) = \frac{(\frac{T_{COH}}{z-1})D(z)}{1+(\frac{z+1}{2z})(\frac{T_{COH}}{z-1})D(z)} \tag{4.21}$$

Using $z = 1 + j2\pi f$, we can acquire the analog counterparts, $H(f)$ and $H_n(f)$, for transfer functions by equations (4.20) and (4.21). This linear transform is valid if only $|2\pi f \cdot T| << 1$ can be satisfied (Yu, 2006). The loop bandwidth B_L and loop noise bandwidth B_n take the forms of

$$B_L = \int_0^{\infty} |H(f)|^2 df \tag{4.22}$$

$$B_n = \int_0^{\infty} |H_n(f)|^2 df \tag{4.23}$$

The function of PLL is to maintain the phase error between the replica carrier and the input GPS carrier signals at zero. The accuracy of the frequency and phase synchronization in PLL are affected by a number of factors, such as signal-to-noise power ratio, Doppler frequency shift, and the receiver clock quality. The PLL tracking error can be divided into two parts: the thermal noise and the dynamic stress error (Raquet, 2006).

The standard deviation of the total phase error is described as follows in a basic rule-of-thumb (Kaplan, 1996)

$$\sigma_{PLL} = \sqrt{\sigma_t^2 + \theta_A^2} + \frac{\theta_e}{3} \tag{4.24}$$

In the above equation, σ_t^2 is the thermal noise with an equation of

$$\sigma_t = \frac{360}{2\pi}\sqrt{\frac{B_n}{c/n_0}\left(1 + \frac{1}{2T_{COH}\cdot c/n_0}\right)} \qquad \text{(deg)} \tag{4.25}$$

where c/n_0 is the carrier to noise power expressed as a ratio or expressed by $10^{\frac{CN_0}{10}}$ in dB-Hz. The $\frac{1}{2T_{COH}\cdot c/n_0}$ results from the product of noise at I and Q arms, termed squaring loss.

In equation (4.24), θ_e is the steady state dynamics stress error. For a 2nd order loop, it equals to

$$\theta_e = \frac{0.2809\cdot \ddot{R}}{B_n^2} \tag{4.26}$$

where $\ddot{R}$ represents the maximum LOS acceleration in $\deg/s^2$.

In equation (4.24), the Allan deviation oscillator phase noise θ_A for a 2nd loop can be expressed as (Raquet, 2006; Gao, 2007),

$$\theta_A = \frac{360}{2.5}\cdot\frac{\sigma_A(\tau)\cdot f_L}{B_n} \tag{4.27}$$

f_L is L1 frequency. $\sigma_A(\tau)$ is the root of Allan variance for the short-term gate time τ, which is equal to $1/B_n$.

A simulation case is presented to check the performance of a 2nd order PLL in order to reveal the relations and the trade-off among PLL parameters. In this case, the motions of a land vehicle are generated by the INS signal simulator, which is given in details in the Chapter 2. Figure 4.10 shows the simulated trajectories of 4400 seconds, which are almost same as the example used in Chapter 2. The only difference is that the GPS start time tag is from GPS week 1352 and GPS seconds 516866 instead of from GPS seconds 0. The zoomed-in 20-second trajectory of interest is shown there as well. The correspondingly vehicle's velocities along ENU and heading change in the 20-second period are presented in Figure 4.11 (a) and (b), respectively. The vehicle is turning with a maximum forward acceleration of $3m/s^2$ during this period.

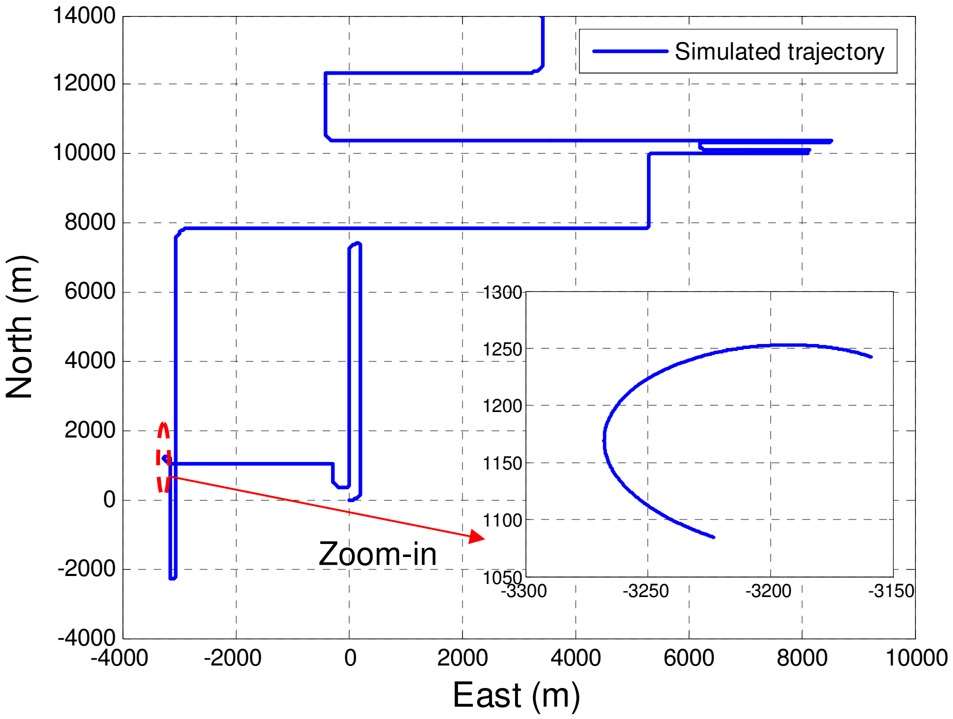

Figure 4.10: Simulated trajectories and zoom-in 20s of interest

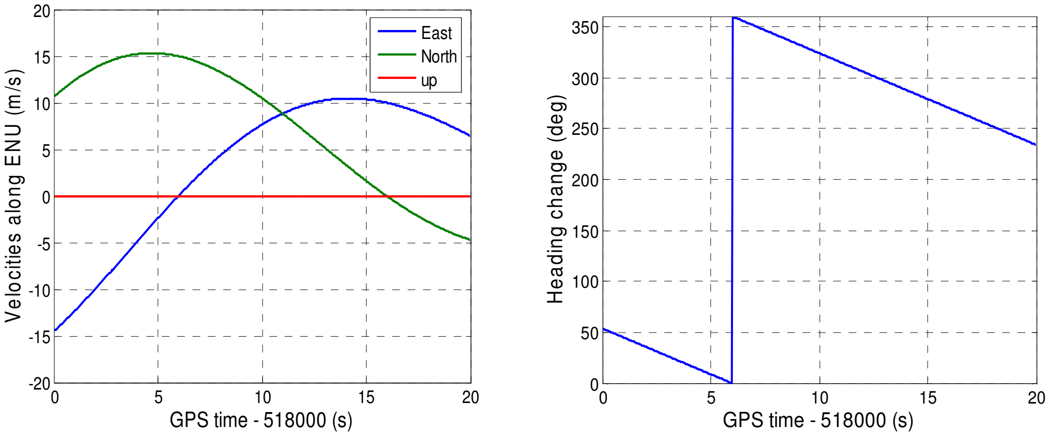

Figure 4.11-a: Simulated velocities of 20s Figure 4.11-b Simulated heading of 20s

The GPS satellite's position and velocity information of GPS satellite PRN13 is calculated based on the real ephemeris corresponding to the simulated GPS time and an assumption of 70 ms signal propagation time. The dynamic information combining both satellite and land vehicle provides the error-free reference Doppler frequency shift in the simulation case, as shown in the Figure 4.12.

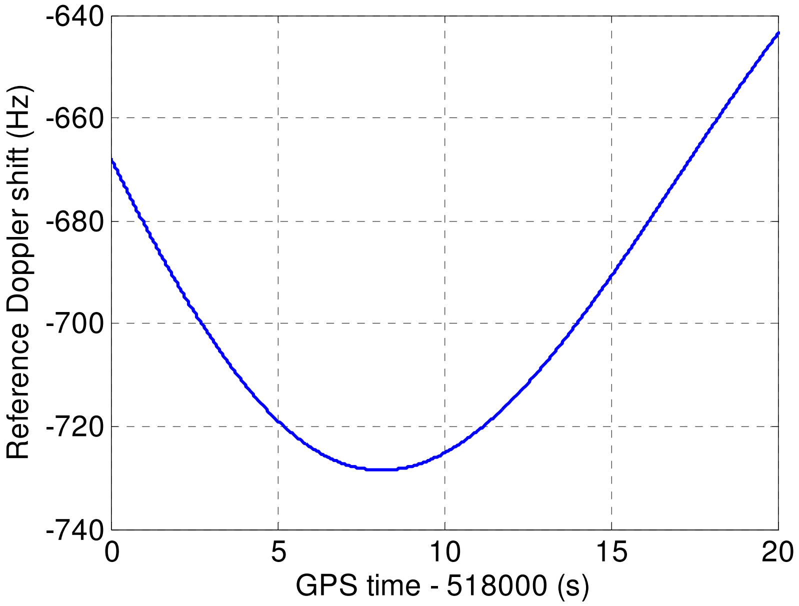

Figure 4.12: Calculated reference Doppler shift

As mentioned before, the inputs of the PLL are the COH I and Q samples, as mathematically described in Equations (4.17) and (4.18). The PLL implementation complies with the process depicted in Figure 4.9 with the arctangent discriminator presented in Table 4.2 and Figure 4.6.

Figure 4.13 gives an example of the loop's behaviour of the tracked Doppler frequency, the estimated frequency error and the phase tracked error. A 40 dB-Hz incoming signal's C/N_0, 1ms PIT and 15 Hz noise bandwidth are used in this example.

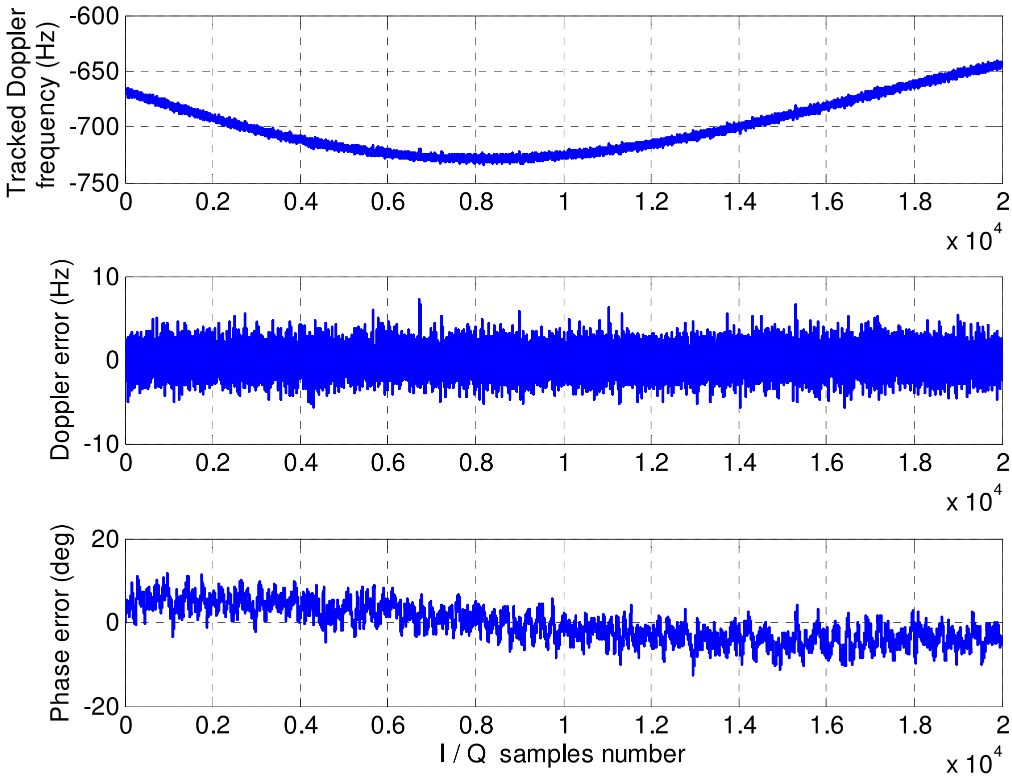

Figure 4.13: An example of 2nd order PLL behaviour of the simulation case

$$(C / N_0 = 40dB - Hz \quad B_n = 15Hz \quad PIT = 1ms \ )$$

From Figure 4.13, it is obvious that the PLL can lock the incoming signal carrier and the frequency change well since the phase tracking error (1σ) is far beyond the threshold of loss-lock, rule-of-thumb 15^{o} (Kaplan, 1996; Raquet, 2006). In addition, as motioned before, the signal power should be concentred on the in-phase component if the incoming signal is correctly tracked. Figure 4.14 gives an example of 1000 COH I_p and Q_p of the PRN 13 after 1ms accumulation from the above case. It clearly shows that the Q component is noise-like signal and the I component contains almost all the signal power.

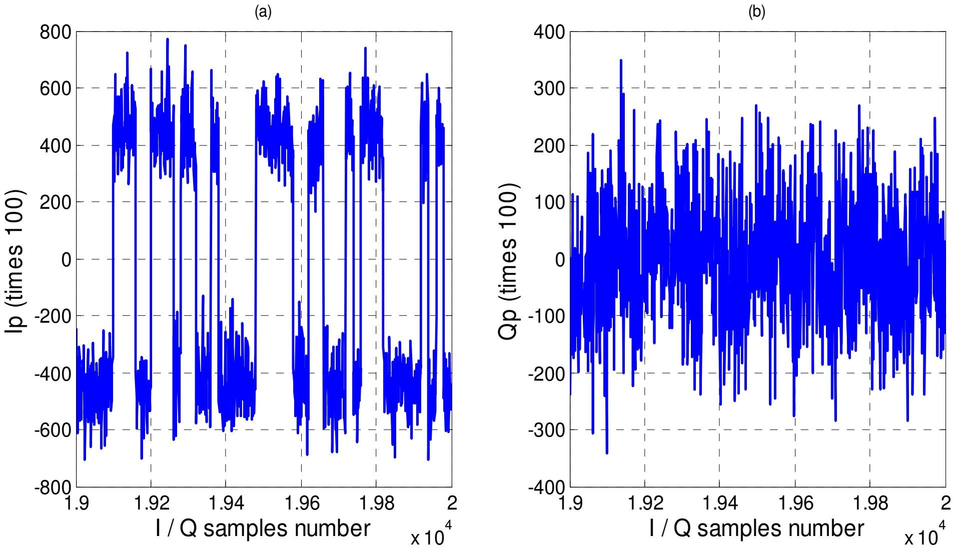

Figure 4.14: In-phase and quadrature-phase components

It should be also noted that the lock status is required to indicate the tracking status of PLL. In theory, we should use the C/N_0 to determine if the receiver remains lock status. The estimation of C/N_0 is necessary because it decreases rapidly once the receiver loses lock. The C/N_0 can be estimated by comparison of the signal power in two different bandwidths. We can typically select the wideband WBP_k as $1/PIT$ and the narrow band NBP_k as $1/20ms$. The estimation of C/N_0 is given as (Pakinson and Spiller, 1996),

$$C/N_0 = 10\lg\left(\frac{\mu P - 1}{(20 - \mu P)\cdot PIT}\right) \tag{4.28}$$

where,

$$\mu P = \frac{NBP_k}{WBP_k};$$

$$NBP_k = \left(\sum_{i=1}^{m} I_{P,i}\right)^2 + \left(\sum_{i=1}^{m} Q_{P,i}\right)^2;$$

$$WBP_k = \sum_{i=1}^{m} \left(I_{P,i}^2 + Q_{P.i}^2 \right);$$

m is typical satisfied with $m \times PIT = 20ms$.

Furthermore, the C/N_0 estimation can be improved by averaging several estimations with number of *K*, because the standard deviation of C/N_0 estimation is reduced by a factor of $\sqrt{K}$. A total of 50 estimations is used here to get the final C/N_0 estimation. Therefore, the output rate of C/N_0 is 1Hz since the average time is $K \times m \times PIT = 1s$. For the above example, the C/N_0 estimation is shown in Figure 4.15.

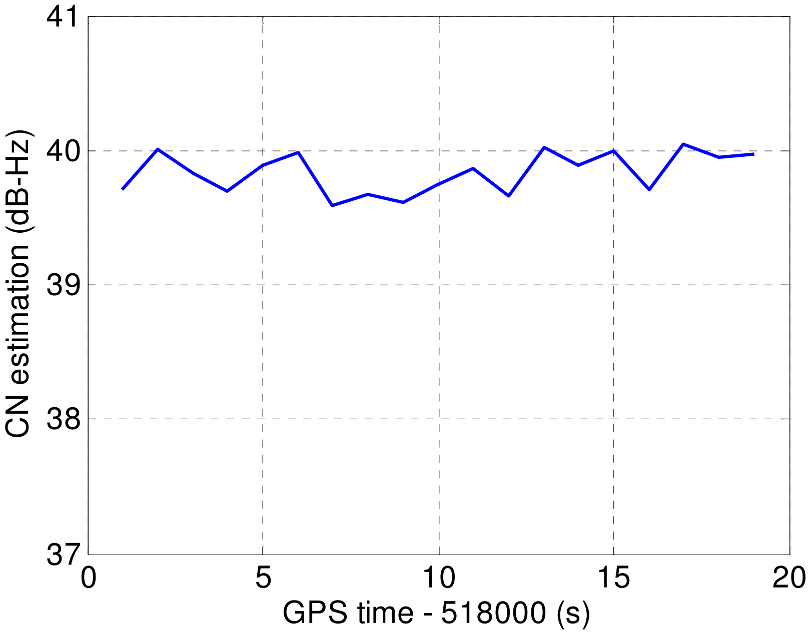

Figure 4.15: C/N_0 estimation

The estimation of C/N_0 according to equation (4.28) is time consuming. Furthermore, the bit-sync is pre-requirement for that. Therefore, typically, a PLL lock detector is used to check the lock status instead of such estimation. The value of lock detector directly reflects the quality of C/N_0 (Ma et al, 2004). Parkinson and Spiller (1996) give the calculation details of the lock detector $L\_C2\phi_k$, as briefly summarized below.

$$L\_C2\phi_k = \frac{NBD_k}{NBP_k} \approx \cos(2\delta\phi_k) \tag{4.29}$$

where,

$$NBD_k = \left(\sum_{i=1}^{m} I_{P,i}\right)^2 - \left(\sum_{i=1}^{m} Q_{P,i}\right)^2$$

Obviously, the PLL lock detector is a function of the phase tracking error. It will approach 1 when the phase tracking error is small enough. The threshold of $L\_C2\phi_k$ is selected by the receiver designer. Since the percentage of the incoming signal powers on I_P can be roughly expressed as $I_p^2/(I_p^2+Q_p^2) \approx \cos^2 \delta\phi_k$, a threshold of 0.7 is selected in this study to assure at least 85% of the signal power still on the in-phase component. The tracking will be assumed failure if the value of lock detector is smaller than this threshold. For the above example, Figure 4.16 shows the output of lock detector. Both Figure 4.16 (calculated) and Figure 4.13 (observed) conclude that the incoming signal carrier and the frequency change described by Figure 4.10 to Figure 4.11 with signal strength of $40dB-Hz$ are well tracked by the designed 2$^{\text{nd}}$ order PLL.

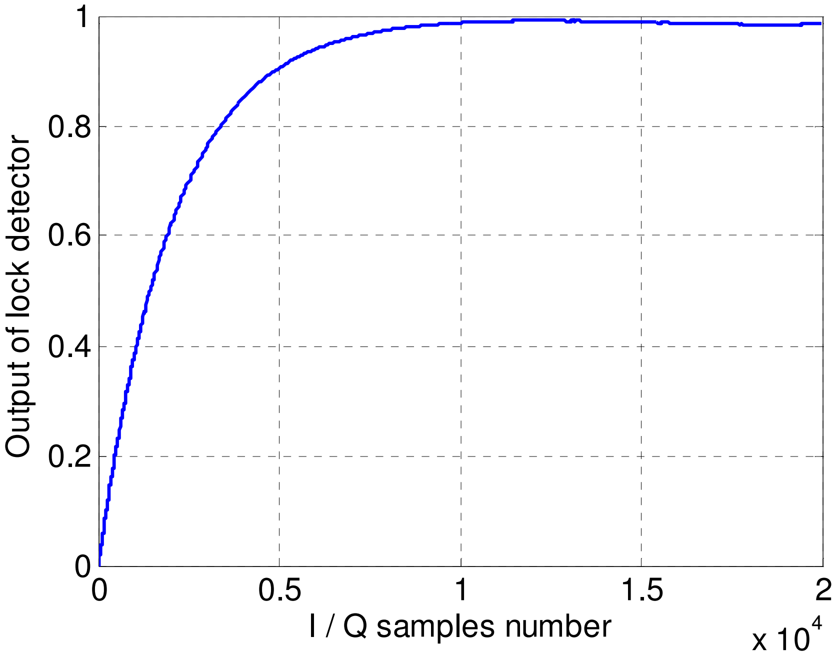

Figure 4.16: PLL lock detector behaviour with strong signal (40dB-Hz)

Table 4.4 compares tracking errors with different loop parameters. The results clearly show that the tracking error is larger when the tracked signal is weaker. For example, when C/N_0 decreased from 40 $dB-Hz$ to 30 $dB-Hz$ with the same bandwidth 15 Hz , the phase error increased from 1.24 degree to 14.05 degree. The narrower bandwidth is helpful to the reduction of the tracking errors, e.g. B_n decreased from 15 Hz to 12 Hz, accordingly, phase error decreased from 14.05 degree to 11.49 degree; however, the bandwidth cannot be narrowed without limits as the PLL has to track the vehicle dynamics as well. Unreasonable value for the noise bandwidth results in the loss-of-lock.

Table 4.4: Tracking errors of different parameters

(GPS week = 1352, GPS time = 518000~518020, PRN 13)

B_n (Hz)	C/N_0 $dB-Hz$	PIT ms	Tracking error $(1-\sigma)$		Lock status
			Doppler (Hz)	Phase (deg)	
15	40	1	1.48	1.24	Yes
15	30	1	4.47	14.05	Yes
12	30	1	2.99	11.49	Yes
6	30	1	--	--	No

4.4 Summary

This Chapter 4 investigates the operation of GPS receiver. The tracking loop and its tracking performance associated with its parameters are explained in details. The first section in this chapter describes the GPS receiver signal processing technology, which involves GPS signals, receiver FE, acquisition, tracking, measurement derivation, and navigation solution. Based on the receiver signal flow, tracking loops including accumulator, discriminator, and loop filter are studied.

The simulation tests from a 2nd order PLL with dynamic environment verify that 1) the signal power is concentred on the I (in-phase) component when the incoming signal is correctly tracked; 2) the tracking error is larger when the tracked signal is weaker; 3) the narrower bandwidth is helpful to the reduction of the tracking errors; 4) under a high dynamic environment, the extended integration time leads to an unacceptable phase error.

Chapter 5 INS Doppler Aided Receiver Tracking Loop

To accommodate dynamic stress, the most effective way is to broaden the PLL bandwidth. This gives rise to a dilemma in GPS receiver design. The common method for designing a PLL tracking loop is to choose a loop bandwidth which is primarily determined by the loop filter while considering the worst case of C/N_0 and the highest Doppler frequency caused by the dynamics (Lian, 2004). Usually these designs are robust but not optimal. Fortunately, INS Doppler aiding contributes to the PLL to track much weaker GPS signals continuously by removing most of the dynamic stress, which allows the reduction of the noise bandwidth. Section 5.1 discusses the method and the implementation of INS Doppler aiding to the conventional PLL. The effect of Doppler accuracy on INS aided PLL is analyzed as well. Section 5.2 implements and tests an EKF based INS Doppler aided tracking loop as well as the corresponding INS/GPS integration.

5.1 INS Aided Tracking Loop

5.1.1 Implementation of IPLL

In urban canyon environments, a tightly coupled INS/GPS yields integrated navigation solution continuously even if the situations of fewer than four satellites frequently occur. But the navigation performance is dependent on the satellite geometry, i.e. the number of satellites in-lock and the distribution of the satellites in the sky. GPS signals are not as easy to be locked as in open-sky since the signal strength is attenuated by blockages, reflections, cross-correlation, multipath, etc. INS aiding is helpful to remain the PLL in-lock under weak signal environments by removing the loop's dynamic stress.

From the Figure 4.9, we learn that the carrier frequency deviation (f_{PLL}) from the baseband frequency is primarily comprised of three components: the Doppler frequency (f_{doop}) due to the relative motion between the receiver and the satellite; frequency errors due to the OSC (f_{osc}); and errors due to thermal noise (f_{noise}), which can be expressed as

$$f_{PLL} = f_{dopp} + f_{osc} + f_{noise} \tag{5.1}$$

The main idea of INS aiding is to add the external Doppler frequency estimate ($\hat{f}_{INSdopp}$) from INS to the output of the loop filter in order to narrow the loop's noise bandwidth. As described before, the PLL can not distinguish the dynamics between the actual LOS motions and OSC instability. Whereas, the INS with Doppler measurements only detects the LOS relative motions between the INS and the satellite. Therefore, the dynamics due to the receiver clock drift should be considered in an IPLL. Based on the Equations (4.25) and (4.27), Figure 5.1 compares the phase errors introduced by thermal noise and by the receiver clock (e.g. TCXO), both as a function of loop bandwidth. The results indicate that in the low noise bandwidth range, especially for weaker signals, the clock dynamics dominate the tracking errors.

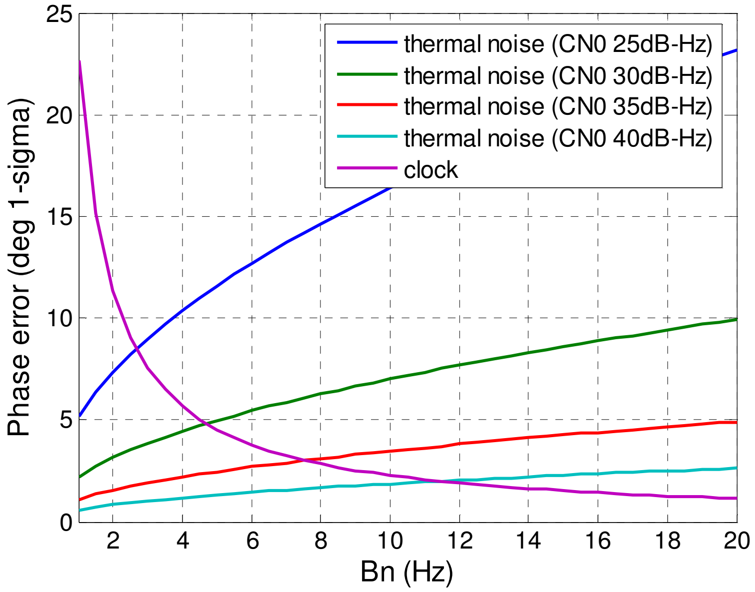

Figure 5.1: Phase errors due to signal strength and clock drift vs. bandwidth

Thus, a complete INS aiding is implemented by adding both $\hat{f}_{INSdopp}$ and the OSC estimate ($\hat{f}_{osc}$) to the output of the loop filter. The NCO, therefore, can be restructured as shown in Figure 5.2.

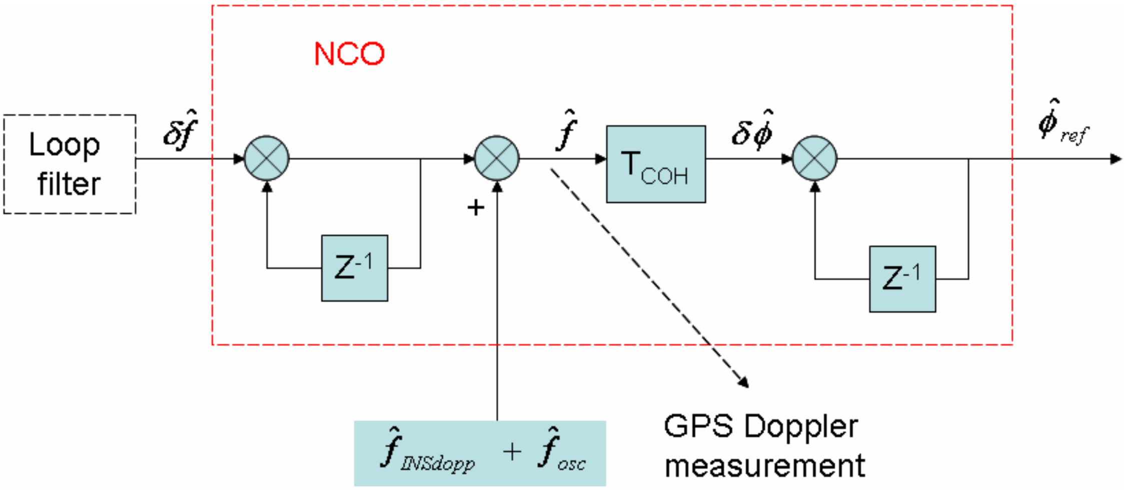

Figure 5.2: Restructured NCO in IPLL

If the receiver dynamics are removed by using external estimates of INS Doppler with very high precision, the error of PLL is mainly determined by thermal noise which is a function of B_n, T_{COH} and C/N_0. Based on the rule-of-thumb Equation (4.25), Figure 5.3 gives the phase error variations with the different C/N_0 and B_n (with 1ms PIT). Furthermore, the simulation experiment presented in Section 4.3 is repeated here except that the bandwidth of IPLL is narrowed to $3Hz$ in order to track the incoming signal as weak as $30dB-Hz$. Figure 5.4 shows the IPLL behaviour of the tracked Doppler frequency, the estimated frequency error and the phase tracked error. The tracked Doppler error (1σ) is 0.87Hz and the phase error (1σ) is 3.1 degrees. Both Figures 5.3 and 5.4 clearly show the advantages of external INS aiding, of which the narrower noise bandwidth help PLL to track the weaker signal.

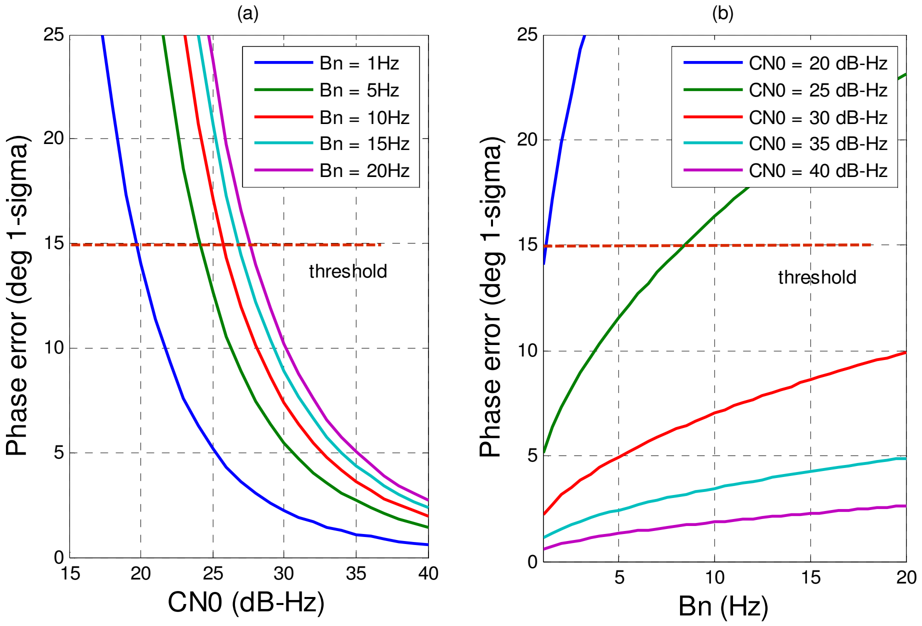

Figure 5.3: Phase errors vs. C/N_0 and B_n with error-free aiding information

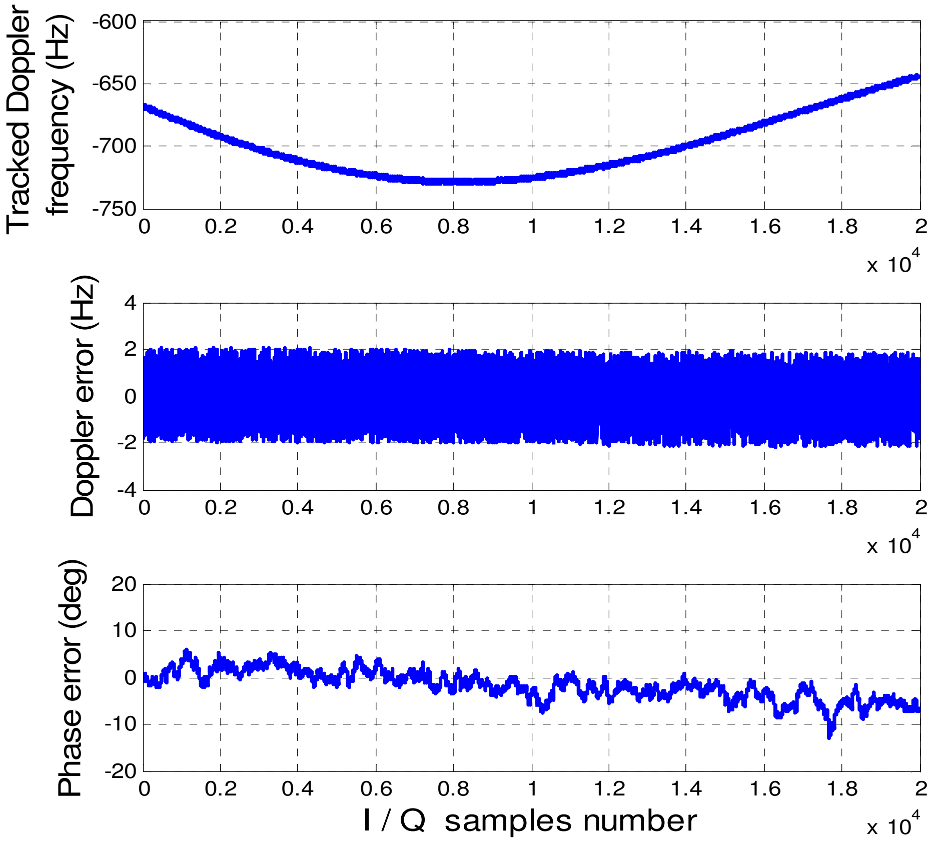

Figure 5.4: IPLL behaviour of the simulation case

$(C/N_0 = 30dB-Hz \quad B_n = 3Hz \quad PIT = 1ms\ )$

5.1.2 Effect of INS Doppler Accuracy

Although, owing to the removal of the loop's dynamic stress, the weaker signal can be tracked by virtue of INS Doppler aiding, the use of perfect aiding information in the above cases is only an ideal case. In practice, the external INS Doppler estimate and clock drift estimate are not always accurate. External aiding may introduce a different form of dynamics stress in the form of errors from the Doppler and clock drift estimates

(Yang and El-Sheimy, 2006; Chiou, 2005). Therefore, the IPLL must be designed to track phase dynamics due to the INS Doppler estimate errors ($\delta\hat{f}_{INSdopp}$) and the receiver clock drift error ($\delta\hat{f}_{osc}$). The receiver clock drift is modeled as a process of random walk in this research. As a result, the value of the loop filter's output for IPLL can be written as

$$f_{PLL} = f_{noise} + \delta\hat{f}_{INSdopp} \tag{5.2}$$

Assuming that the dynamics of the INS Doppler estimate errors are slower than the vehicle's dynamics, from the above equation, the use of INS Doppler aiding allows for noise bandwidth reduction in IPLL when compare to a traditional PLL.

After removal of the dynamics, with a random constant assumption of the aiding frequency error, the rule-of-thumb equation of phase error (4.25) can be re-written as the following

$$\sigma_{PLL} = 360 \cdot \delta\hat{f}_{INSdopp} \cdot T_{COH} + \frac{360}{2\pi}\sqrt{\frac{B_n}{c/n_0}\left(1+\frac{1}{2T_{COH}\cdot c/n_0}\right)} \quad \text{(deg)} \tag{5.3}$$

As illustrated in the Equation (3.25) in the Chapter 3, the INS Doppler frequency of the carrier signal can be expressed as the velocity of the INS relative to the satellite, projected onto the LOS vector. Computing the value of the INS Doppler error requires performing a covariance analysis. Based on that equation, we have the 1σ standard deviation in the INS Doppler estimate with respect to the $k-th$ satellite as following,

$$\lambda_{L_1}^2 \sigma_{f_{INSdopp,k}}^2 = \left(\frac{\partial\hat{f}_{INSdopp,k}}{\partial \mathbf{e}_k}\right)^{\mathbf{2}} \sigma_{\mathbf{e}_k}^2 + \left(\frac{\partial\hat{f}_{INSdopp,k}}{\partial \mathbf{V}_{INS}}\right)^2 \sigma_{\mathbf{V}_{INS}}^2 + \left(\frac{\partial\hat{f}_{INSdopp,k}}{\partial \mathbf{V}_{SV,k}}\right)^2 \sigma_{\mathbf{V}_{SV,k}}^2 \tag{5.4}$$

Compared the LOS vector change rate of the $k-th$ satellite with the INS rate, it is reasonable to assume $\sigma_{\mathbf{e}_k} = \mathbf{0}$. In addition, the satellite velocity errors determined by the broadcast ephemeris errors are always supposed to be much smaller than the velocity errors from INS, especially for MEMS grade INS. Thus, the Equation (5.4) can be expanded and re-written as

$$\sigma^2_{f_{INSdopp,k}} = \frac{\mathbf{e}_k^T E\left(\delta\mathbf{V}_{INS}\delta\mathbf{V}_{INS}^T\right)\mathbf{e}_k}{\lambda_{L_1}^2}$$

$$= \frac{1}{\lambda_{L_1}^2}\begin{bmatrix} e_{kx} & e_{ky} & e_{kz} \end{bmatrix}\mathbf{R}_l^e \begin{bmatrix} \sigma^2_{\delta v_E} & 0 & 0 \\ 0 & \sigma^2_{\delta v_N} & 0 \\ 0 & 0 & \sigma^2_{\delta v_U} \end{bmatrix}\mathbf{R}_e^l \begin{bmatrix} e_{kx} \\ e_{ky} \\ e_{kz} \end{bmatrix} \tag{5.5}$$

where

$E(\cdot)$ represents the expectation operation;

$\sigma^2_{\delta v_E}, \sigma^2_{\delta v_N}, \sigma^2_{\delta v_U}$ are the variances of the ENU velocity errors, respectively.

To establish the relations between INS Doppler aiding error and the INS ENU velocity errors, an upper bound on the magnitude of the aiding error is considered here. Assume that $\sigma^2_{\delta v_E} = \sigma^2_{\delta v_N} = \sigma^2_{\delta v_U} = \sigma^2 = \max\left\{\sigma^2_{\delta v_E}, \sigma^2_{\delta v_N}, \sigma^2_{\delta v_U}\right\}$ and the INS velocity vector along ECEF ($\mathbf{V}_{INS}$) is aligned with the LOS vector. With these bound assumptions, from the Equation (5.5), we have

$$\max(\sigma^2_{f_{INSdopp,k}}) = \sigma^2 / \lambda \tag{5.6}$$

The above equation indicates that the maximum Doppler aiding error is determined by the INS ENU velocity error. Thus, combining the Equation (5.2), the objective of narrowing the loop bandwidth in IPLL is actually an effort to control the INS ENU velocity error drift.

Without error control, i.e. by INS direct aiding, the IPLL performance heavily depends on the quality of the INS since there is no bound of INS velocity error drift. Repeat the simulation experiment presented in Section 4.3 again. In order to track the incoming signal as weak as $30dB-Hz$, INS direct aiding is used to narrow bandwidth to $3Hz$. Figure 5.5 (a) and (b) compares the aiding Doppler shifts and their errors for different grade INSs, respectively. Given that all the INSs operate 20s only without alignment errors and the only inertial sensor error source of each INS is the heading gyro bias, e.g. in run bias of 1deg/hr, 10deg/hr, 50deg/hr and 200deg/hr (MEMS grade). Table 5.1 lists the tracking errors for different grade INSs aiding.

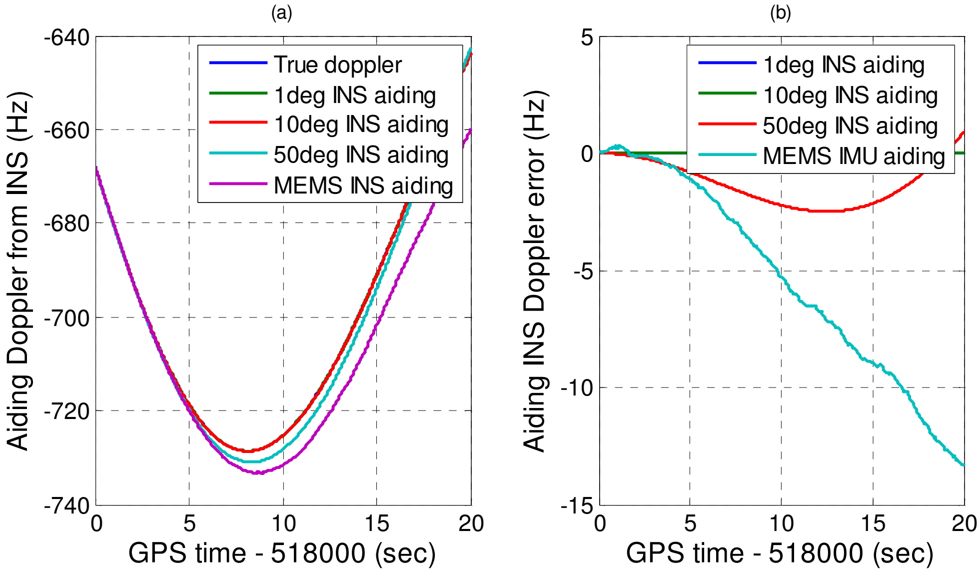

Figure 5.5: Aiding Doppler and errors with different grade INSs

Table 5.1: Tracking error with different grade INS aiding

INS	Tracking errors $(1-\sigma)$		Lock status
	Doppler (Hz)	Phase (deg)	
1 deg/hr	1.94	6.9	Yes
10 deg/hr	1.94	8.6	Yes
50 deg/hr	1.98	11.8	Yes
MEMS based INS	--	--	No

Both the above results and the Equation (5.5) indicate that, without velocity error control, the performance of IPLL not only is associated with its parameters but also heavily depends on the quality of the INS. MEMS based INS direct aiding can not present the advantages of an IPLL; on the contrary, it will destroy the operation of an IPLL. Another simulation example about INS direct aiding which is presented in Appendix B confirms the above results.

5.2 EKF based MEMS INS Aided Tracking Loop

5.2.1 EKF based IPLL

An EKF is used to fuse the MEMS based INS and receiver measurements (pseudorange and Doppler) to control the errors of INS aiding Doppler to the IPLL. At the same time, this EKF also provides INS/GPS tightly coupled navigation solution. Figure 5.6 gives the proposed system configuration with IPLL and INS/GPS tightly coupled navigation solution.

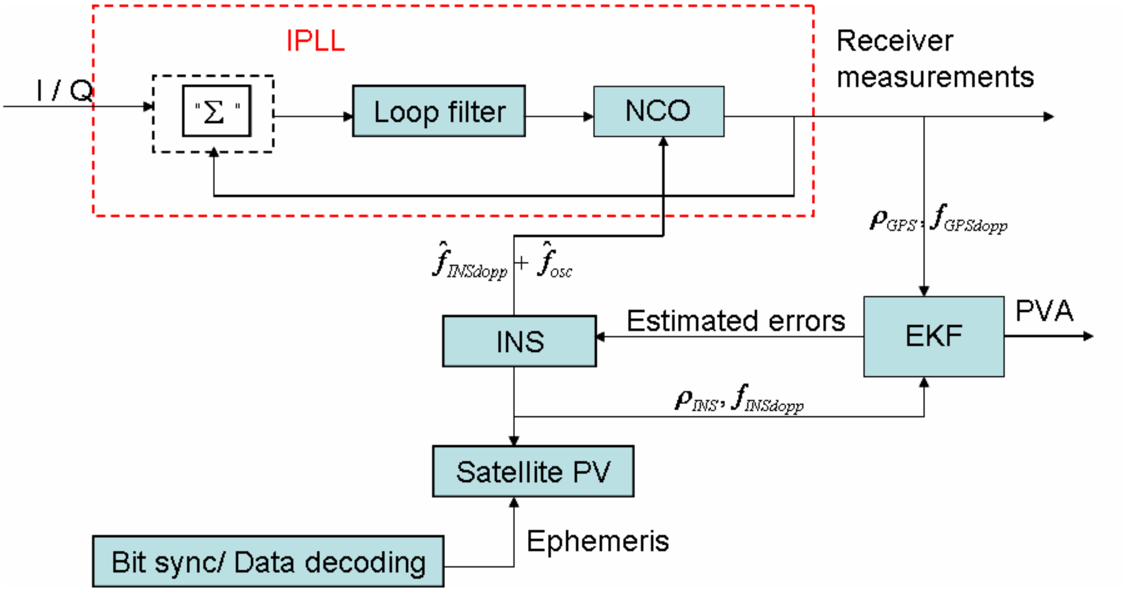

Figure 5.6: Proposed system configuration of INS/GPS integration with IPLL

In the above figure, the NCO details of the IPLL are depicted in the Figure 5.2. The aiding information is calculated from the INS/GPS tight integration filter. The code loop (not shown in this figure) aided by the IPLL carrier, as normal receiver does, provides the receiver pseudorange measurements. In this configuration, the IPLL starts in normal PLL mode until the ephemeredes are decoded and a first position/velocity/clock drift estimate is available. It should be noted that the first clock drift estimate is assumed as a "constant bias" during IPLL operation in this research. Therefore, the clock drift information to IPLL is a combination of the above bias and an estimated value from EKF, in which the clock drift is considered as a random walk. In most cases, the value of first clock drift is not zero, so the clock drift aiding information $\hat{f}_{osc}$ is mainly determined by its first estimate, which comes from PLL. There are 23 error states in the EKF. The state vectors and observables for EKF are thoroughly described in the Section 3.4.3. The INS Doppler calculation is described in the Section 3.4.2.

According to the proposed INS aiding scheme, some modules in a conventional receiver need to be changed, as illustrated in the Figure 5.7. The required changes in the INS-aided receiver can be fulfilled through the software method in a software receiver.

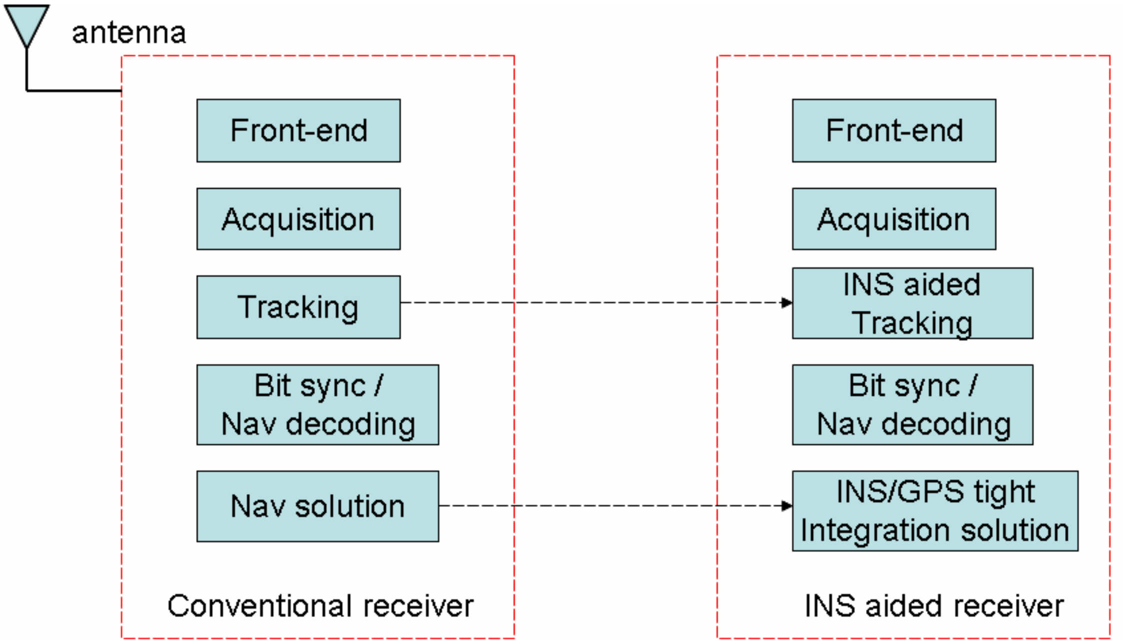

Figure 5.7: Module comparison of the conventional and INS-aided receivers

5.2.2 Performance Tests and Analyses

To test the IPLL and the INS aided receiver performance, a field test was conducted around Springbank, Alberta in December 2005, which has been described in Chapter 3. The system setup was shown in Figure 3.4. The data from an ADI MEMS INS and NordNav software GPS receiver were collected. The LN200 INS data and differential GPS data are processed to generate the reference trajectory. The ADI MEMS INS and the front-end of the NordNav receiver are shown in the Figure 5.8. The front-end was driven by a laptop's USB. The front-end of the receiver down-converts the L_1 GPS signal to an

IF of $4.1304 MHz$. The sampling rate is $16.3676 MHz$.

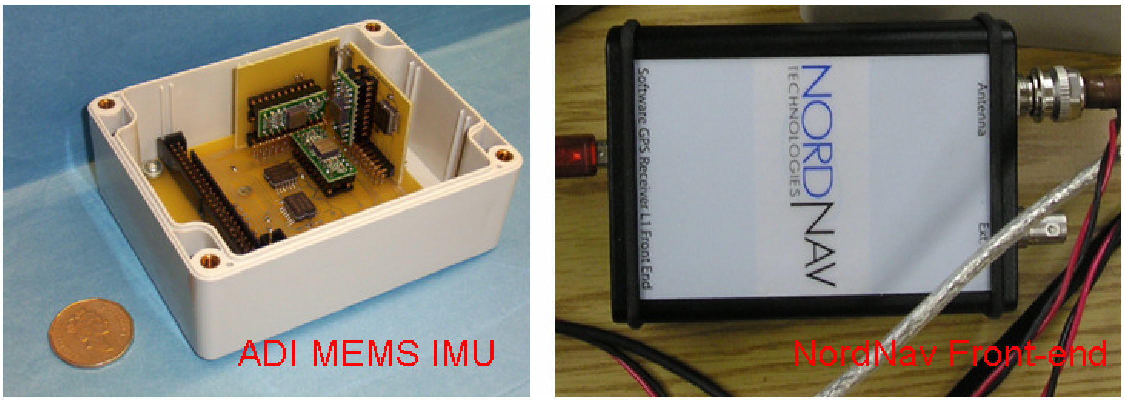

Figure 5.8: ADI MEMS IMU and NordNav Front-end

The datasets from the software GPS and ADI INS were post-processed. Due to the lack of full access to this receiver, the post-processing procedure consisted of the following five steps:

1) Record receiver pseudorange and Doppler measurements then synchronize them with INS data manually. Since the pseudorange measurements are associated with bit/frame sync process and INS aiding mainly executes on the carrier tracking, we assume only GPS Doppler measurements are changed by INS aiding.

2) The NordNav software provides two types of accumulator (after pre-integration) messages. One is the standard early-prompt-late correlator (correlator spacing 1 chip) message and the other is the multiple-correlator message, which is mainly used for anti-multipath. To simplify the data processing, we only set parameters for the standard correlator before running the receiver. The corresponding accumulator messages are recorded. Then, synchronize the recorded accumulator data with the INS data manually by virtue of a message header contained in each GPS message. This header includes a

receiver run time and a GPS time. The GPS time will indicate zero unless the receiver tracks four or more satellites and computes a position. Combining the GPS time, the receiver run time and measurements, it is easy to manually synchronize INS data and accumulator data and select the accumulator data (I and Q samples after pre-integration) during tracking process.

3) Tune the level of signal strength (C/N_0) by injecting various power levels of white Gaussian noise into the collected I and Q samples (Chiou, 2005), which generates the new I and Q samples (I_d/Q_d) under the degraded signal environments. The relations between the injected white noise and C/N_0 can be expressed by the Equation (5.7).

$$\sigma_{w,add}^2 = \frac{M_E}{2T_s} N_0 (10^{0.1\Delta C/N_0} - 1) \tag{5.7}$$

where

$\sigma_{w,add}^2$ is the noise variance of the injected white noise;

M_E is number of samples per COH accumulation segment, equal to T_{COH}/T_s, where T_s is the sampling period, $T_s = 1/(16.3676\times10^6)$ for NordNav front-end;

N_0 is the received noise density and the typical value of N_0 is $-205 dBW/Hz$ (Lachapelle, 2005);

$\Delta C/N_0$ is the signal strength difference between the collected signal and the desired signal for degraded signal simulation.

4) I_d and Q_d samples pass through the developed IPLL module (or conventional PLL) and the developed INS/GPS tight integration navigation module to verify the

performance of tracking loop and navigation solution. Meanwhile,

5) Due to the limited access to the FE LO, I_d and Q_d samples are reconstructed by multiplying a coefficient of normalized sinc function in each IPLL step to simulate the NCO adjustments approximately. The sinc function is illustrated in the Equation (5.8).

$$A_{coef} = \frac{\sin[\pi(f_{open} - f_{\deg r})T_{COH}]}{\pi(f_{open} - f_{\deg r})T_{COH}} \tag{5.8}$$

where

A_{coef}	is the coefficient multiplied to I_d and Q_d samples;
f_{open}	is the tracked frequency under the strong signal environment, which is acquired in this section by using the collected I and Q samples from the NordNav accumulator directly since the signal environment is always open sky during the Springbank field test;
$f_{\deg r}$	is the tracked frequency from the IPLL (or conventional PLL) under the simulated degraded signal environment.

An approximate L-shape trajectory was driven in the field test, same as shown in the Figure 3.6. Figure 5.9 shows the satellites tracked by the NordNav receiver in the field tests between GPS time 521990s to 523300s in 1352-th GPS week. According to the receiver default setting, the cutoff elevation for the satellites is 5^0. Figure 5.10 gives the corresponding signal strength during the test. Since it is always open sky during the test, four or more than four satellites are well tracked. We will use the Equation (5.7) to simulate the signal degrade environments based on the field test data.

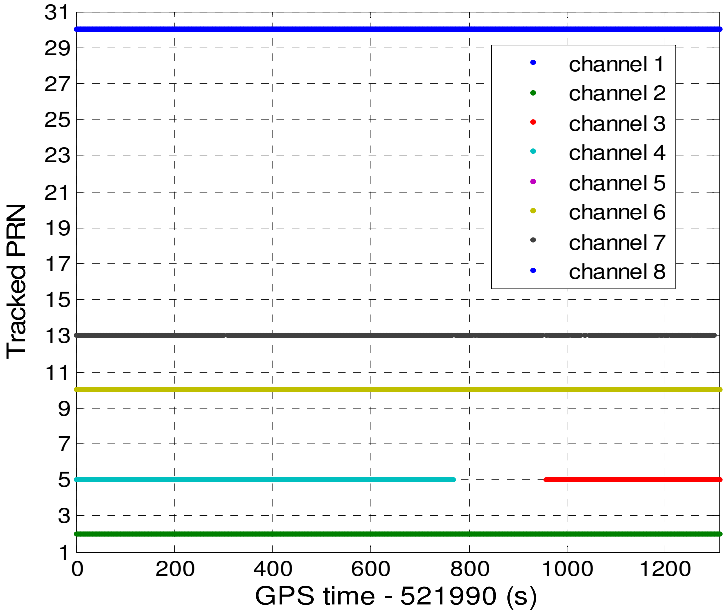

Figure 5.9: Satellites tracked in the field test

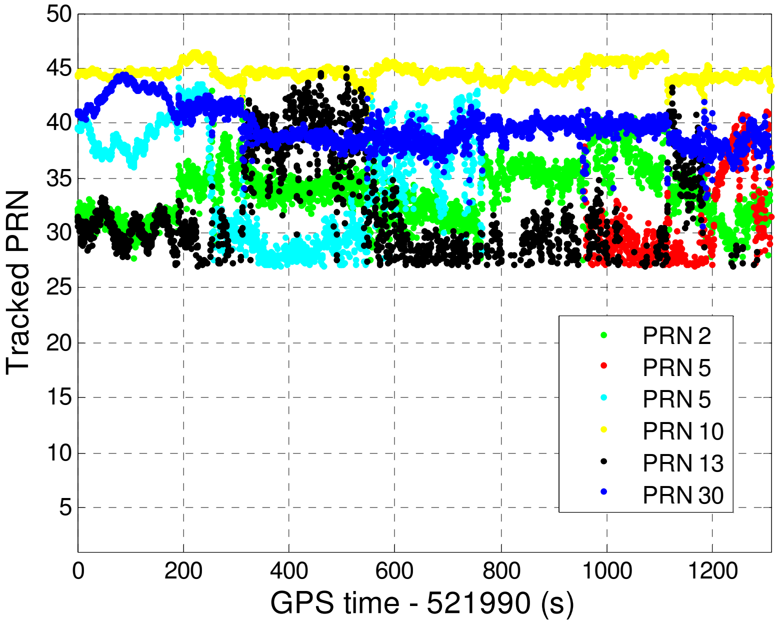

Figure 5.10: The signal strength during the test y-axis should C/N

Similar to the previous method, 20 seconds trajectory and motions of interest are selected to analyze the IPLL thoroughly. Figure 5.11 (a) and (b) show the 20s zoom-in trajectories and C/N_0 of interest (522730s to 522750s), when the vehicle was steering toward north with a maximum acceleration of $2.8 m/s^2$. Most of C/N_0 for each satellite are above $30 dB-Hz$. To simplify the problem, we can simulate a signal outage case for PRN 2 by using the Equation (5.7).

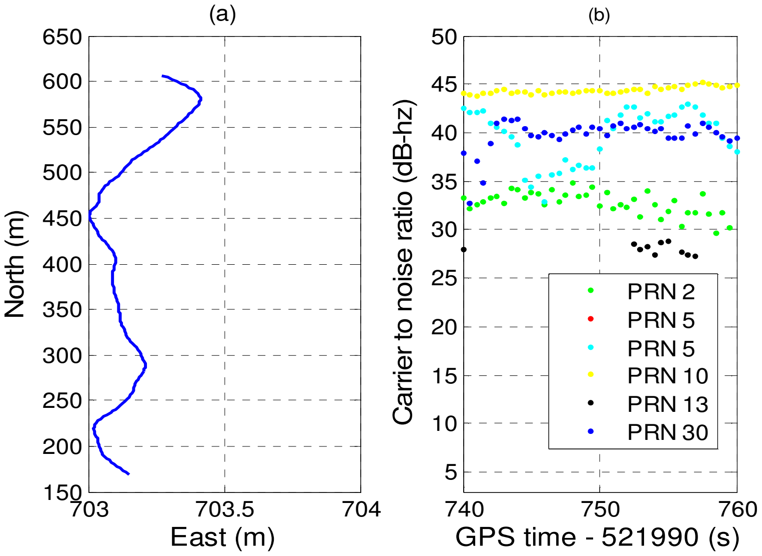

Figure 5.11: 20s trajectories and signal strength of interest

Given that C/N_0 of PRN 2 is degraded to $26 dB-Hz$. Figure 5.12 gives the lock detector output of a conventional receiver PLL. It is obvious that the PLL loses the lock of the carrier frequency, which results in fewer than four satellites being tracked during this period of interest.

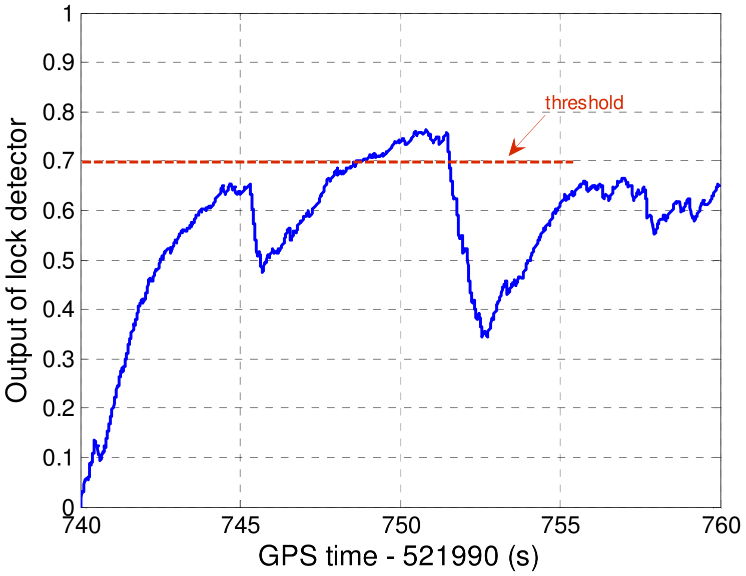

Figure 5.12: Lock detector output of conventional PLL with $C/N_0 = 26 dB-Hz$

Under the same signal conditions, IPLL instead of conventional PLL is used to track the PRN 2. The external Doppler and the estimate of the receive clock drift are fed into PLL NCO. The aiding information is from ADI MEMS INS/NordNav GPS tightly integrated system. As noted before, 1G2A suboptimal INS configuration is used for aiding. Figure 5.13 shows the aiding Doppler at 100Hz including both the INS Doppler estimate and the clock drift estimate for the IPLL in the Channel 2 of the receiver, where the PRN 2 was being tracked.

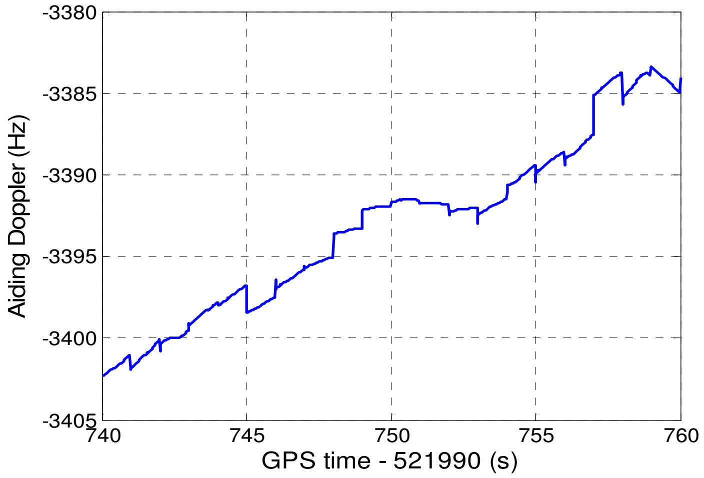

Figure 5.13: Aiding Doppler to IPLL

By using the above adding Doppler information, Figure 5.14 (a) and (b) show the outputs of the IPLL discriminator and the loop filter, respectively, which are the indicators of the IPLL tracking quality. The output of the IPLL discriminator (ATAN discriminator) is actually the phase difference between the incoming signal and the generated local signal. From the figure, the phase difference (not phase error) is around 48 degrees (1σ). These differences result from both the vehicle's dynamic motions and the phase tracking errors. As mentioned before, the Costas ATAN discriminator remains linear at a range of $-90^{\circ} \sim 90^{\circ}$. Thus, the Figure 5.14 (a) indicates the IPLL discriminator remains in a good status to produce the difference between the incoming and replicated phases.

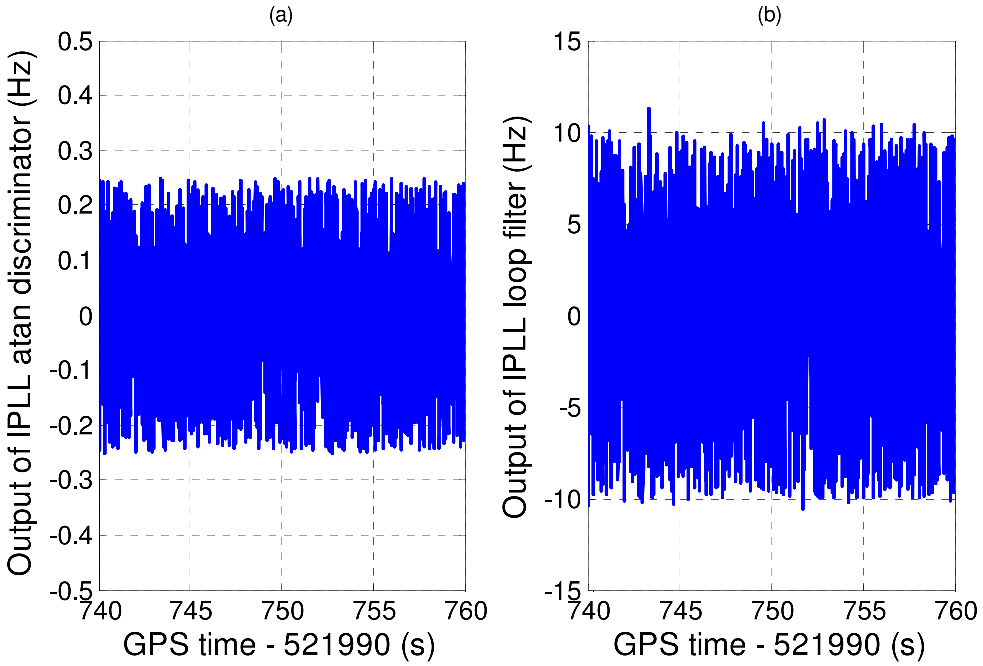

Figure 5.14: Outputs of IPLL discriminator and loop filter

In addition, by INS Doppler aiding, the LOS dynamics is removed from the tracking loop. According to the Equation (5.2), the output of IPLL only includes the frequency of aiding Doppler error and the errors due to thermal noise, all of which are relatively small values. The theoretical Equation (5.2) is qualitatively verified in the Figure 5.14 (b).

Figure 5.15 (a) gives the lock detector output of IPLL. Compared with the Figure (5.12), it is obvious that the carrier frequency of PRN 2 is locked by using MEMS INS Doppler aiding, which is superior to the conventional PLL. Figure 5.15 (b) shows the receiver's corresponding estimation of C/N_0 based on the Equation (4.28). There is no rapid change of C/N_0, which indicates the channel with IPLL is well tracking the satellite. Both (a) and (b) of the Figure 5.15 indicate the IPLL can track weak signal as low as

$26dB-Hz$.

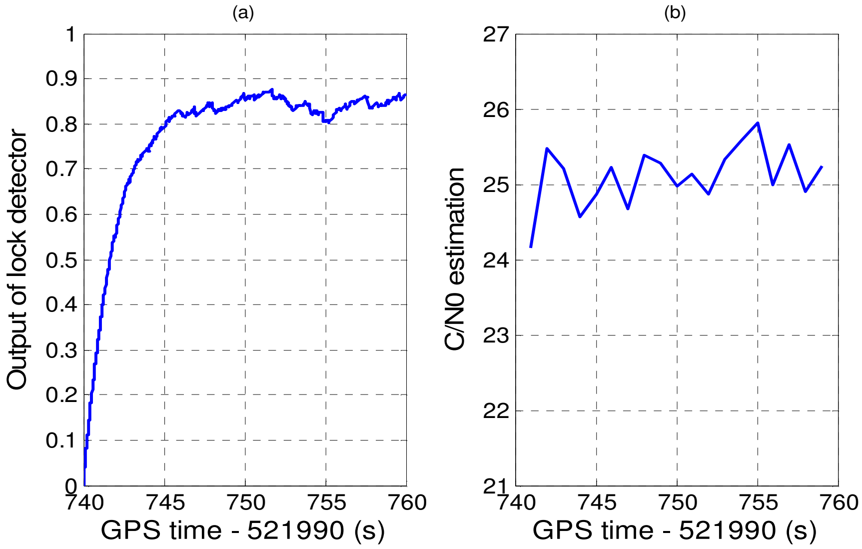

Figure 5.15: Lock detector output and C/N_0 estimation from IPLL

To search for the margin of the signal strength that could be tracked by IPLL for the same case, Figure 5.16 compares the lock detector outputs with different signal strength (but with the same loop bandwidth $14Hz$ same as before). It clearly shows the IPLL can track the weak signals of approximate $24dB-Hz$. In a receiver with conventional PLLs, loss of lock typically occurs at a signal power equal to approximately $27dB-Hz$ (Gebre-Egziabher et al., 2005; Ma et al, 2004). Figure 5.16 indicates that, with Doppler aiding, an additional $3dB-Hz$ margin can be achieved, allowing signals with power as low as $24dB-Hz$. Another test of 20s based on the real dataset presented in Appendix C confirms the above results.

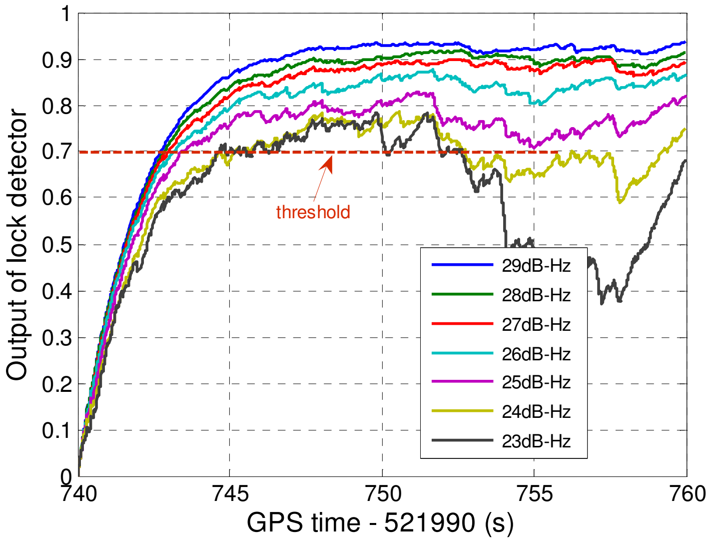

Figure 5.16: Output of IPLL lock detector vs. different signal strength

It should be noted that the further margin can not be obtained simply by reducing the loop noise bandwidth. As described previously, the normalized noise variance is inversely proportional to C/N_0. According to Equation (5.3), it is no doubt that reducing the loop noise bandwidth can mitigate the effect of this error; nevertheless, doing such increases the tracking errors. The rule-of-thumb equation is based on two important assumptions: small phase tracking errors and steady state. But in the real case, especially for dynamic environment with low C/N_0 condition, the above two assumptions can not always be satisfied. Figure 5.17 compares the lock detector outputs with different loop noise bandwidths (but with the same signal strength $26dB-Hz$), which indicates that too narrow bandwidth results in unstable loop locks even loss-of-lock. That is because the IPLL has to track the residual dynamics caused by thermal noise, Doppler aiding and clock aiding; and the thermal noise error starts to dominate the total phase error at lower

C/N_0 range (Chiou, 2005). A reasonable bandwidth should be selected to guarantee that the discriminator operates within a linear region (Yu, 2006). A KF based carrier tracker instead of conventional tracking loops can be used because the bandwidth chosen by this estimator is optimal in the sense of minimum mean square error (Psiaki and Jung, 2002). However, that topic is beyond the scope of this dissertation and will not be discussed further.

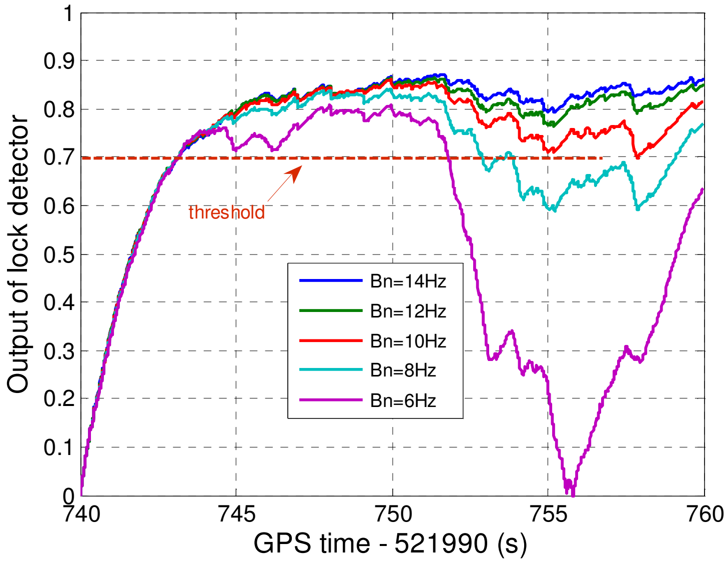

Figure5.17: Output of IPLL lock detector vs. different bandwidth

After INS aiding, the Doppler output from IPLL and pseudorange measurements from DLL (assumed no changes), together with MEMS INS measurements, are used as observables to the MEMS INS/GPS tight integration EKF, Figure 5.18 compares the navigation errors between tight integration with PLL and that with IPLL. We assume that there is no GPS pseudorange and Doppler measurements available in the GPS channel where the tracking loop loses satellite lock. The comparison takes place under weak signal environment, e.g. $C/N_0 = 26dB-Hz$, of which two satellites suffer (PRN 2 and PRN 30) loss in the conventional PLL while IPLL locks them. Again, the 1G2A suboptimal ADI MEMS INS configuration is used in the tightly coupled navigation.

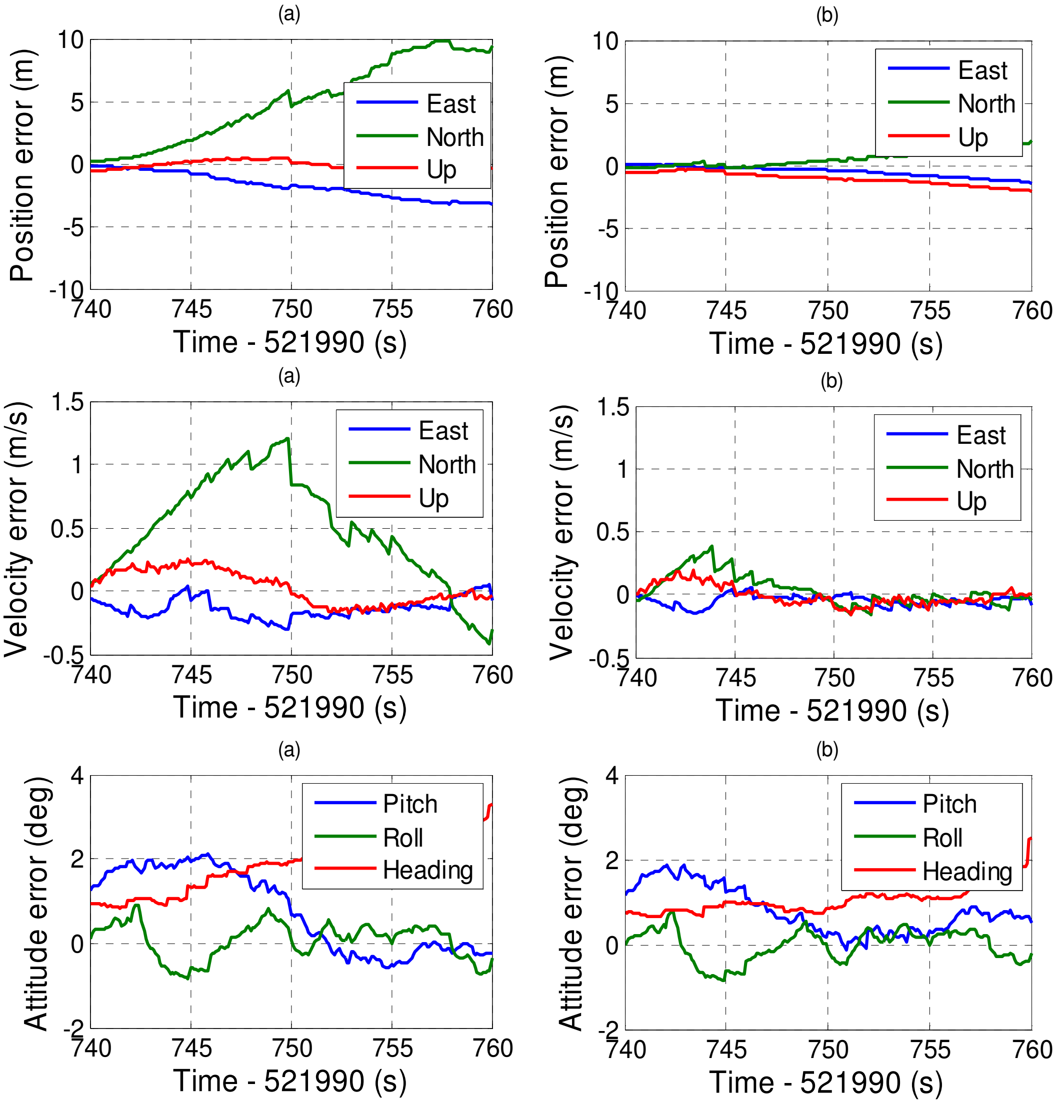

Figure 5.18: Comparison of navigation errors by using PLL and IPLL

During this 20s of interest, the vehicle traveled $178m$, known from reference trajectory provided by LN200 and DGPS. In Figure 5.18, (a) shows the errors of integrated navigation solution using PLL in the receiver. By contrast, (b) shows those using IPLL. In (a), two satellites lose lock since the conventional PLL can not track weak signals as low as $C/N_0 = 26dB - Hz$. Only the other two satellites (PRN 10 and PRN 5) provide raw GPS measurements, which results in the degraded satellite geometry. As analyzed before, the navigation performance is for sure degraded because of the geometry degradation. The errors, especially for the velocity errors, are also from the INS pseudo-signal in 1G2A configuration due to the vehicle's dynamics. However, the 3D position error is less than $11m$ ($< 6\%$ of the travel distances), which is acceptable for MEMS INS based land vehicle navigation system thanks to the advantages of INS/GPS tightly coupled integration scheme.

Compared with (a), Figure 5.18 (b) clearly shows that the tightly coupled navigation performance is improved by using IPLL. Another test result presented in Appendix C shows a similar improvement. Totally four satellites are being tracked under weak signal environments because of the use of IPLL, which improves the satellite geometry. In addition, during this 20s, the tight couple EKF has a good observability due to the relatively high dynamics, which mitigates errors caused by INS pseudo-signal in some extent. The position error is reduced to $< 2\%$ of the travel distances $(4m)$, which is 67% improvement compared with the previous one.

5.3 Summary

This chapter implements the INS Doppler aided GPS receiver tracking loop. INS aided tracking is implemented by adding both INS Doppler and the receiver clock drift estimate to the NCO. The IPLL can track weaker GPS signals continuously compared with the convention PLL as it only needs to track the residual dynamics after aiding. The relations between INS Doppler aiding error and the INS ENU velocity errors are established as well as the effect of Doppler accuracy on IPLL is analyzed. In addition, this chapter proposes a system configuration of INS/GPS integration with IPLL and future modules for an INS aided receiver.

Simulation tests show that MEMS based INS direct aiding can not present the advantages of an IPLL; on the contrary, it will destroy the operation of an IPLL. Therefore, an EKF with INS/GPS tight scheme is used to control the INS aiding error as well as provide navigation solution. Results based on the field test datasets indicate that, with MEMS INS Doppler aiding, an additional $3dB-Hz$ margin can be achieved, allowing signals with power as low as $24dB-Hz$ to be successfully tracked. Compared with the results of conventional PLL in a tight INS/GPS integration, the position accuracy of IPLL is significantly improved.

Chapter 6 Conclusions and Recommendations

This chapter contains a summary of the research work presented in this dissertation, the conclusions drawn from the theoretical developments and test results, and recommendations for future research and developments in this field.

6.1 Summary

The main objective of this research was to develop a tightly coupled MEMS INS/GPS integration with INS aided GPS receiver tracking loops. To accomplish the dissertation objective and test the proposed methods, four sub-topics were investigated and presented in four Chapters. They are INS signal simulator, MEMS INS/GPS tight integration, GPS receiver tracking loops, and INS aided carrier tracking loop.

The INS signal simulator is a methodical combination of the inverse INS mechanization and various inertial sensor errors. The concepts of the INS simulator were used in the pseudo-signal generation of the sub-optimal INS configuration for INS/GPS tight integration. The simulator was also used in the performance analyses of unaided PLL and aided PLL by different quality INSs under weak signal environment. This was followed by investigations of INS/GPS integration schemes and the error models of INS and GPS, an INS/GPS tight integration algorithm based on an EKF of 23 states which was developed for this task. The pseudorange and Doppler measurements from both INS and GPS were used as the observables for the EKF. Specially, MEMS INS/GPS tightly coupled integration with a sub-optimal INS configuration of one gyro and two accelerometers were proposed. The tightly coupled algorithm and the sub-optimal INS configuration were used to implement the INS aided GPS receiver carrier tracking loop. The GPS receiver tracking loop and its parameters were investigated. After a review of the process of GPS receiver signal processing, the PLL behaviors in the presence of the main error sources including thermal noise and dynamics stress were examined based on the simulations. INS Doppler aiding contributes to the PLL to track much weaker GPS signals continuously by removing most of the dynamic stress, which allows the reduction of the noise bandwidth. The method of INS Doppler aiding to the conventional PLL was discussed. An EKF-based MEMS INS Doppler aided tracking loop is implemented. The aiding performances were presented and analyzed on both GPS receiver tracking loop level and INS/GPS integrated system navigation solution level.

Two software packages, i.e. INS simulator (named INSS) and INS/GPS tight integration (named TIG), were developed. They are not only used for this dissertation, but used for other related works as both of them are integral and independent software written in C language. IPLL algorithm was implemented in MATLAB for the dissertation research purpose.

6.2 Conclusions

Analyses of the results lead to the following conclusions in terms of the objectives set out in Chapter 1.

INS Signal Simulator

1. The INSS is an effective, economical and flexible tool for research related to

inertial navigation system. The simulator provides much similar INS signals to that of a hardware INS. It can speed up the algorithm development on INS/GPS integration;

Tightly Coupled INS/GPS

2. The tightly coupled INS/GPS can work well under the environment with fewer than four satellites. The position errors are less than 7m, 31m, 40m or 41m during 30s GPS signal outage environment, i.e. 3, 2, 1, or 0 satellite(s) in-view, respectively; Furthermore, by using non-holonomic constraint for land vehicle application, the position accuracy can be improved by around 60%.
3. The performance of tightly coupled system is associated with both the vehicle dynamics and satellites geometry. Fewer satellites being tracked result in worse navigation performance due to the worse satellites geometry;
4. Suboptimal INS/GPS tight integration with 1G2A INS configuration can maintain the system positioning error at an acceptable level, i.e. smaller than 7m, 27m, 38m, or 40m during 30s GPS signal outage environment, with 3, 2, 1 or 0 satellite(s) in-view, respectively.

GPS Receiver Tracking Loops

5. The tracking error is larger when the tracked signal is weaker. The narrower bandwidth is helpful to the reduction of the tracking errors. The signal power is concentred on the in-phase component when the incoming signal is correctly tracked.

INS Aided Carrier Tracking

6. INS aiding can effectively improve a standard GPS receiver tracking performance in weak signals and high dynamics environments. With the error controlled by an EKF in INS/GPS tightly coupled scheme, MEMS INS Doppler aiding, can achieve an additional $3dB - Hz$ margin for the receiver signal tracking, allowing signals with power as low as $24dB - Hz$ to be tracked.
7. Compared with the conventional tight integration, the position accuracy of the tight INS/GPS integration with IPLL is improved under attenuated signal environments.

6.3 Recommendation for Future Work

Due to the experiment limitations, current IPLL tests presented in Chapter 5 comply with an open loop manner with several assumptions. The complete operation from signal acquisition to tracking, maintaining tracking, loss of tracking, and re-acquisition is a closed loop manner (Dong, 2003). To achieve a close loop test, it is necessary to complete the other GPS receiver processing functions involving acquisition/re-acquisition, bit/frame sync, and measurements derivation. A software receiver would speed up the research work. In addition, a software receiver makes it possible to implement the proposed receiver modules in the Chapter 5. Furthermore, it is recommended to test the algorithms with more data sets, particularly in real urban areas environment instead of simulated urban environment, to represent broader ranges of vehicle dynamics and satellite geometries.

In the current aiding scheme, the aiding rate of INS information is expected be as high as possible since this information derives the NCO directly and is considered as a constant frequency during the IPLL accumulation and dump. However, aiding at a high rate, e.g. 100 Hz, brings hard tasks for the NCO hardware implementation. In addition, the problem of time synchronization increases the complexity of the IPLL. Further work is recommended to test if low aiding rate, e.g. 1 Hz, can achieve similar benefits.

Although the Chapter 5 concludes that the narrower loop noise bandwidth using INS Doppler aiding enhances the receiver carrier tracking capability, it has not solved the problem of “how many hertz the IPLL bandwidth should be”. Constant bandwidths are used for all the tests. The Equation (5.5) sets up a relation between INS Doppler aiding errors and the ENU velocity error variances. The ENU velocity error variances are part of diagonal components in the covariance matrix of EKF. It is recommended to establish the relations between the bandwidth and the covariance matrix of EKF so as to adjust the optimal bandwidth adaptively.

REFERENCES

Akos, D.M., Normark, P. (2001). Global Positioning System Software Receiver (gpSrx) Implementation in Low Cost/Power Programmable Processors. ION GPS 2001, Salt Lake City, UT, US, pp. 2851-2858.

Alban, S., Akos, D. M., Rock, S. M (2003). Performance Analysis and Architectures for INS-Aided GPS Tracking Loops. ION NTM 2003, Anaheim, CA, US, pp. 611-622.

Allan, D.W. (1987), Time and Frequency (Time-Domain) Characterization, Estimation, and Prediction of Precision Clocks and Oscillators, in IEEE Transactions on Ultrasonics, Ferroelectrics, and Frequency Control, Vol. UFFC-34, No. 6, pp.647-654

Babu, R., and Wang, J. (2005). Analysis of INS-derived Doppler effects on carrier tracking loop. The Journal of Navigation, Vol. 58(3), pp. 1-15.

Barbour, N. and G. Schmidt (2001). Inertial Sensor Technology Trends. IEEE Sensors Journal, vol. 1, no. 4, pp. 332-339.

Beser J., S. Alexander, R. Crane, S. Rounds and J. Wyman (2002) .Trunavtm: A Low-Cost Guidance/Navigation Unit Integrating A SAASM-Based GPS And MEMS IMU In A Deeply Coupled Mechanization. ION GNSS 2002, Portland, OR, US, pp. 545-555.

Betz, J.W. (2002). Binary Offset Carrier Modulations for Radionavigation. The Journal of Navigation, Vol. 48(4), pp. 227-246.

Bian, S., Jin, J., and Fang, Z. (2005). The Beidou Satellite Positioning System and Its Positioning Accuracy. Journal of The Institute of Technology, 52(3), pp. 123-129.

Brenner, M. (1995). Integrated GPS/Inertial Fault Detection Availability. Proceedings of ION GPS 1995, Palm Springs CA, US, pp. 1949-1958.

Brown, A., and Y. Lu. (2004). Performance Test Results of an Integrated GPS/MEMS Inertial Navigation Package. ION GPS 2004, Long Beach CA, U. S, pp. 825-832.

Brown, R. G. and P.Y.C. Hwang (1997). Introduction to Random Signals and Applied Kalman Filtering. John Wiley & Sons.

Carver, C. (2005). Myths and Realities of Anywhere GPS High Sensitivity versus Assisted Techniques. GPS World, Sep 1, 2005. http://www.gpsworld.com/gpsworld.

Chaffee, J. W.,(1987). Relating the Allan Variance to the Diffusion Coefficients of a Linear Stochastic Differential Equation Model for Precision Oscillators. IEEE Transactions On Ultrasonics, Ferroelectrics, and Frequency control, Vol. UFFC-34, No. 6, pp. 655-658

Charkhandeh, S. (2007). X86-Based Real Time L1 GPS Software Receiver. MSc Thesis, Department of Geomatics Engineering, University of Calgary, Canada, UCGE Report No. 20253.

Chartield, A.B (1997). Fundamentals of High Accuracy Inertial Navigation. AIAA, Reston, VA, USA.

Chiou T. Y., S. Alban, S. Atwater, J., etl (2004). Performance Analysis and Experimental Validation of a Doppler-Aided GPS/INS Receiver for JPALS Applications. ION GNSS 2004, Long Beach, CA, US, pp. 1609-1618.

Chiou, T-Y (2005). GPS receiver performance using inertial-aided carrier tracking loop. ION GNSS 2005, Long Beach, CA, US, pp. 2895-2910.

Davis, J. A., C. A. Creenhall, and P. W. Stacey, (2005), A Kalman filter clock algorithm for use in the presence of flicker frequency modulation noise, Metrologia 42, Institute of

Physics Publishing, pp. 1-10.

Dong, L. (2003). IF GPS Signal Simulator Development and Verification. MSc Thesis, Department of Geomatics Engineering, University of Calgary, Canada, UCGE Report No. 20184.

El-Sheimy, N. (2006). Inertial Techniques and INS/GPS Integration. ENGO 623 Lecture notes, winter, Department of Geomatics Engineering, the University of Calgary, Canada.

El-Sheimy, N. and Niu, X. (2007). The Promise of MEMS to the Navigation Community. Inside GNSS, Invited Paper, , www.insidegnss.com, March/April, pp 26-56.

European Commission (2007). http://ec.europa.eu/dgs/energy_transport/galileo.

Farrell, J. A. and M. Barth (2001). The Global Positioning System & Inertial Navigation. McGraw Hills.

Faulkner, N. M., Cooper, S. J. and Jeary, P. A. (2002). Integrated MEMS/GPS Navigation Systems. Position Location and Navigation Symposium, April, Palm Springs CA, IEEE, pp. 306-313.

FCC (2003). Enhanced 911 (FCC-911) Mandate. http://ww.fcc.gov/Bureaus/Engineering_Technology/Public_Notics.

Ford, T., Hamilton, J. and Bobye,M. (2004). GPS/MEMS Inertial Integration Methodology and Results. ION GNSS 2004, pp1587-1597.

Gao, G. (2007). INS-Assisted High Sensitivity GPS Receivers for Degraded Signal Navigation. PhD Thesis, Department of Geomatics Engineering, University of Calgary, Canada, UCGE Report No. 20252.

Gebre-Egziabher, Razavi, D., Enge, A. P. etl. (2003). Doppler Aided Tracking Loops for SRGPS Integrity Monitoring. ION GPS 2003, pp. 2562-2571.

Gebre-Egziabher, Razavi, D., Enge, A. P. etl. (2005). Sensitivity and performance analysis of Doppler-aided GPS carrier-tracking loops. Journal of the Institute of Navigation, Vol. 52 (2), 2005, pp. 49-60.

Gebre-Egziabher, D., Petovello, M. and Lachapelle, G. (2007). What is the difference between 'loose', 'tight', 'ultra-tight' and 'deep' integration strategies for INS and GNSS? Inside GNSS, www.insidegnss.com, February, 2007, pp 28-33.

Gelb, A. (1974). Applied Optimal Estimation. The Massachusetts Institute of Technology Press, US.

Gierkink, S. L. J. (1999), Control Linearity and Jitter of Relaxation Oscillators, Eindhoven, The Netherlands.

Godha, S. (2006). Performance Evaluation of Low Cost MEMS-Based IMU Integrated With GPS for Land Vehicle Navigation Application. MSc Thesis, Department of Geomatics Engineering, University of Calgary, Canada, UCGE Report No. 20239.

Gold K. and Brown, A. (2004) Architecture and Performance Testing of a Software GPS Receiver for Space-based Applications. Proceeeding s of IEEE AC, 2004, pp.1-12.

Gordon, N. J., Salmond, D. J., and Smith, A. F. M. (1993). Novel approach to nonlinear/non-Gaussian Bayesian state estimation. IEE Proceedings Part F: Communications, Radar, and Signal Processing, 140(2):107–113.

Gregory, W.H. and Garrison, J.L. (2004). Architecture of a Reconfigurable Software Receiver. ION GNSS 2004, Long Beach, CA, US, pp 947-955.

Grewal, M.S. and Andrews, A.P. (1993). Kalman Filtering Theory and Practice. Prentice-Hall, Inc.

Grewal, M. and Andrews, A. P. (2001). Kalman Filtering: Theory and Practice Using Matlab. John Wiley and Sons Inc.

Gustafson D., Dowdle, J., and Flueckiger, K. (2000). A High Anti-Jam GPS based Navigator. ION NTM 2003, Anaheim CA, US, pp. 495-503.

Hide, C. D. (2003) Integration of GPS and Low Cost INS Measurements. PhD Thesis, Institute of Engineering, Surveying and Space Geodesy, University of Nottingham, UK.

Hein, G.W., Godet,J., Issler, J.-L. et al (2001). The GALILEO Frequency Structure and Signal Design. ION GPS 2001, Salt Lake City, UT, US, pp. 1273-1282.

Hou, H. (2003). Inertial sensor errors modeling using Allan Variance. ION GPS/GNSS 2003, September, Portland, OR, US, pp. 2860-2867.

Humphreys, E. D., Psiaki, M. L., and Kinter,P. K. (2005). GPS Carrier Tracking Loop Performance in the Presence of Ionospheric Scintillation. ION GNSS 2005, Long beach CA, pp. 156-166.

ICD-GPS-200C (2000), GPS Interface Control Document, NAVSTAR GPS Space Segment / Navigation User Interfaces, IRN-200C-004. http://www.navcen.uscg.gov/gps.

Julien, O. (2005) Design of Galieo L1F Receiver Tracking Loops. Ph.D. Thesis, Department of Geomatics Engineering, University of Calgary, Canada., UCGE Reports No. 20227.

Kalman, R.E. (1963). New Methods and results in linear filtering and prediction theory. Proceeding of the First Symposium on Engineering Application of Random Function

Theory and Probability. John Wiley.

Kaplan, E.D. (1996). Understanding GPS Principles and Applications. Artech House Publishers, Boston, MA.

Karunanayake, D., M.E. Cannon, G. Lachapelle, G. Cox (2004). Evaluation of AGPS in Weak Signal Environments Using a Hardware Simulator. ION GNSS 2004, Long Beach CA, US, pp. 2416-2426.

Kim, H., Bu, S. and Lee, G. (2003). An Ultra-tightly coupled GPS/INS Integration using Federated Kalman filter. ION GNSS 2004, Portland, OR, US, pp. 2878-2885.

Klukas, R., O. Julien, L. Dong, M.E. Cannon, and G. Lachapelle (2004). Effects of Building Materials on UHF Ranging Signals. GPS Solutions, Vol. 8, No. 1, pp1-8.

Klukas, R. and Fattouche, M. (1998). Line of Sight Angle of Arrival Estimation in the Outdoor Multipath Environment. IEEE Trans. Vehicular Tech., vol. 47, no.1, pp. 342-351.

Knight, D. T. (1999). Rapid Development of Tightly Coupled GPS/INS Systems. in Aerospace and Electronic Systems Magazine, vol. 12, no. 2, IEEE, pp. 14-18.

Kovach, K, and K. Van Dyke (1997). GPS in Ten Years. Proceedings of the US Institute of Navigation GPS Conference, Sept. 16-19, Kansas City, MS, USA, pp. 1251-1259.

Kreye, C., Eissfeller, B., Winkel, J. (2000). Improvements of GNSS Receiver Performance Using Deeply Coupled INS Measurements. ION GPS 2000, Salt Lake City, UT, US, pp. 844-854.

Krumvieda, K. (2001). A Complete IF Software GPS Receiver: A Tutorial about the Details. ION GPS 2001, Salt Lake City, UT, US, pp. 789-811.

Kovach, K, and K. Van Dyke (1997). GPS in Ten Years. ION GPS 1997, Kansas City, MS, US, pp. 1251-1259.

Lachapelle G., H. Kuusniemi and D. T. H. Dao (2003). HSGPS Signal Analysis and Performance under Various Indoor Conditions. ION GNSS 2003, Portland, OR, US, pp. 1171-1184.

Lachapelle,G. (2005). Advanced GPS Theory and Applications. ENGO 625 Lecture notes, Fall, Dept. of Geomatics Engineering, the University of Calgary, Canada.

Ledvina, B. M., Psiaki, M. L. Sheinfeld, D. J. et al. (2004). A Real-Time GPS Civilian L1/L2 Software Receiver. ION GNSS 2004, Long Beach, CA, US, pp. 986-1005.

Lian, P. (2004). Improving Tracking Performance of PLL in High Dynamic Applications. MSc Thesis, Department of Geomatics Engineering, University of Calgary, Canada, UCGE Reports No. 20208.

Lim, D.W., Cho D.J., Lee, S.J. (2005). An Efficient Signal Processing Scheme and Correlator Structure for Software GPS Receiver. ION NTM 2005, San Diego, CA, US, pp. 1026-1032.

Lin, D. M., Tsui, J.B.Y. et al. (2000). Comparison of Acquisition Methods for Software GPS Receiver. ION GPS 2000, Salt Lake City, UT, US, pp. 2385-2390.

Ma, C. (2003). Techniques to Improve Ground-Based Wireless Location Performance Using a Cellular Telephone Network. PhD thesis, Department of Geomatics Engineering, University of Calgary, Canada, UCGE Reports No. 20177.

Ma, C., Lachapelle, G., and Cannon, M.E. (2004). Implementation of a Software GPS Receiver. ION GNSS 2004, Long Beach, CA, US, pp. 956-970.

MacGougan G. D. (2003). High Sensitivity GPS Performance Analysis in Degraded Signal Environments. Master thesis, Department of Geomatics Engineering, University of Calgary, Canada, UCGE Reports No. 20176.

Maybeck, P.S. (1994). Sochastic Models, Estimation, and Control. Navtech Book & Software Store.

Misra, P. and Enge, P. (2001). Global Positioning System Signals, measurements and performance. Ganga-Jamina Press.

Nassar, S. Syed, Z., and Niu, X. etc. (2006). Improving MEMS IMU/GPS Systems for Accurate Land-Based Navigation Applications. ION NTM 2006, Monterey, CA, US, pp. 523-529.

Niu, X. and El-Sheimy, N. (2005). Development of a Low-cost MEMS IMU/GPS Navigation System for Land Vehicles Using Auxiliary Velocity Updates in the Body Frame. ION GNSS 2005, Long Beach, CA, US, pp. 2003-2012.

Noureldin, A., Shin, E., El-Sheimy, N. (2004). Improving the Performance of Alignment Processes of Inertial Measurement Units Utilizing Adaptive Pre-Filtering Methodology. Zeitschrift für Geodäsie, Geoinformation und Landmanagement, Germany, V 6, pp. 407 – 413.

O'Keefe, K. (2001). Availability and Reliability Advantages of GPS/Galileo Integration. ION GPS 2001, Salt Lake City, UT, US, pp. 2096-2104.

Oleynik, E.G., Mitrikas, V.V., Revnivykh, S.G. (2006). High-accurate GLONASS Orbit and Clock Determination for the Assessment of System Performance. ION GNSS 2006, Ford Worth, Tx, US, pp. 2065-2079.

Pany, T., Kaniuth, R. and Eissfeller, B. (2005). Deep integration of Navigation Solution and Signal Processing. ION GNSS 2005, Long Beach, CA, US, pp. 1095-1102.

Pany, T. and Eissfeller, B. (2006). Use of Vector Delay Lock Loop Receiver for GNSS Signal Power Analysis in Bad Signal Conditions. IEEE PLANS 2006, San Diego, CA, US, pp. 893-902

Park, M. (2004). Error Analysis and Stochastic Modeling of MEMS based Inertial Sensors for Land Vehicle Navigation Applications. MSc Thesis, Department of Geomatics Engineering, University of Calgary, Canada, UCGE Report No. 20194.

Parkinson, B.W. and Spiller, J.J., eds. (1996). Global Positioning System: Theory and Applications, Vol. I. American Institute of Aeronautics and Astronautics.

Petovello, M.G. (2003a). Real-Time Integration of a Tactical-Grade IMU and GPS for High-Accuracy Positioning and Navigation. Ph.D. Thesis, Department of Geomatics Engineering, University of Calgary, Canada, UCGE Report No. 20173.

Petovello, M.G., Cannon, M.E. and Lachapelle, G. (2003b). Benefits of Using a Tactical Grade INS for High Accuracy Positioning, Navigation. Journal of Institute of Navigation, 51 (1), pp. 1-12.

Petovello, M.G. and Lachapelle, G. (2006). Comparison of Vector-Based Software Receiver Implementations with Application to Ultra-Tight GPS/INS Integration. ION GNSS 2006, Fort Worth, TX, US, pp. 1790-1799.

Petovello, M.G., Sun, D., Lachapelle,G., Cannon, M.E. (2007). Performance Analysis of an Ultra-Tightly Integrated GPS and Reduced IMU System. ION GNSS 2007, Fort Worth, TX, US.

Poh, E., Koh, A. and Yu, X. (2002). Integration of Dead Reckoning Sensors with MEMS IMU. Proceeding of ION GPS 2002, pp.1148-1152.

Progri, I.F., Bromberg, M.C., Michalson,W.R., Wang, J. (2007). A Theoretical Survey of the Spreading Modulation of the New GPS Signals (L1C, L2C, and L5). ION NTM 2007, San Diego, CA, US, pp. 561-569.

Psiaki, M. L. and Jung, H. (2002). Extended Kalman Filter Methods for Tracking Weak GPS Signals. in the Proceedings of ION GPS/GNSS, Portland, OR, US, pp. 2539-2553.

Psiaki., M.L. (2004). FFT-Based Acquisition of GPS L2 Civilian CM and CL Signals. ION GNSS 2004, Long Beach, CA, US, pp. 457-473.

Raquet, J. (2006). Advanced GNSS Receiver Technology. ENGO 699.45 Lecture Notes, June, Department of Geomatics Engineering, the University of Calgary, Canada.

Ray, J. K. (2005) Advanced GPS Receiver Technology: Lecture Notes ENGO 699.73. Department of Geomatics Engineering, University of Calgary, Canada.

Rogers, R. M. (2000). Applied Mathematics in Integrated Navigation Systems. American Institute of Aeronautics and Astonautics, Inc.

Savage, P.M.(2000). Strapdown Analytics: Part I, Strapdown Associates, Inc., Maple Plain, Minnesota.

Scherzinger, B.M. (2004). Estimation with application to Navigation: Lecture Notes ENGO 699.11. Dept. of Geomatics Eng., The University of Calgary, Calgary, Canada.

Schwarz, K.-P. and Wei, M. (2000). INS/GPS Integration for Geodetic Applications:Lecture Notes ENGO 623. Department of Geomatics Eng., The University of Calgary, Calgary, Canada.

Shin, E. (2001). Accuracy Improvement of Low cost INS/GPS for Land Application., Msc Thesis, Department of Geomatics Engineering, University of Calgary, Canada, UCGE Report No. 20156.

Shin, E.H. and El-Sheimy, N. (2002). Accuracy Improvement of Low Cost INS/GPS for Land Applications. ION NTM 2002, San Diego, CA, US, pp. 146-157

Shin, E., and N. El-Sheimy (2004). An Unscented Kalman Filter for In-Motion Alignment of Low Cost IMUs. in Proceedings of Position Location and Navigation Symposium IEEE, 26-29 April, pp. 273-279.

Shin, E. (2005). Estimation Techniques for Low-Cost Inertial Navigation. PhD Thesis, Department of Geomatics Engineering, University of Calgary, Canada, UCGE Report No. 20219.

Soloviev A., Graas, F. V. and Gunawardena, S. (2004). Implementation of Deeply Integrated GPS/Low-Cost IMU for Acquisition and Tracking of Low CNR GPS Signals. ION NTM 2004, San Diego, CA, US, pp. 923-935.

Sukkarieh, S. (2000). Low Cost, High Integrity, Aided Inertial Navigation Systems for Autonomous Land Vehicles. PhD Thesis, Department of Mechanical and MechatronicEngineering, University of Sydney, Australia.

Titterton, D.H. and Weston, J.L.(2004). Strapdown Inertial Navigation Technology (2nd Edition). The Institution of Electrical Engineers.

Tsui, J.B. (2000). Fundamentals of Global Positioning System Receivers: A Software Approach. John Wiley & Sons, Inc.

Veitsel, A., Lebedinsky, A., Beloglazov, V., Fomin,I. (2007). Investigation and Experimental Receiving of Galileo Signal. ION NTM 2007, San Diego, CA, US, pp. 974-978.

Vig, J. R. (1992). Introduction to Quartz Frequency Standards, http://www.ieee-uffc.org/freqcontrol/quartz/vig/.

Viterbi, A. J. (1966). Principle of Coherent Communication, McGraw-Hall NY.

Watson R., (2005) High-Sensitivity GPS L1 Signal Analysis for Indoor Channel Modelling. MSc thesis, Department of Geomatics Engineering, The University of Calgary, Canada, UGRE Report 20215.

Yang, Y., El-Sheimy, N. (2006). Improving GPS Receiver Tracking Performance of PLL by MEMS IMU aiding. ION GNSS 2006, Forth Worth, TX, US, pp. 2192-2201.

Yang, Y., El-Sheimy, N., Goodall, C., Niu, X. (2007). IMU Signal Software Simulator. ION NTM 2007, San Diego, CA, US, pp. 532-538.

Yu, W. (2006). Selected GPS Receiver Enhancements for Weak Signal Acquisition and Tracking. Msc Thesis, Department of Geomatics Engineering, University of Calgary, Canada, UCGE Report No. 20249.

Syed, Z., Yang, Y., El-Sheimy, N., Goodall, C. (2007). Vehicle Navigation Using Constraints in Tightly Coupled INS/GPS Integration. IGNSS Symposium 2007, Sydney, Australia, 2007 (to be published).

Zucca, C., and P. Tavella, (2005). The Clock Model and Its Relationship with Allan and Related Variances, in IEEE Transactions on Ultrasonics, Ferroelectrics, and Frequency Control, Vol. 52, No. 2, pp. 289-296.

Appendix A

Dynamics Matrix for INS/GPS Tight Couple EKF

The INS/GPS error states can be described by

$$\delta\dot{\mathbf{x}} = \mathbf{F}\delta\mathbf{x} + \mathbf{G}\mathbf{w} \tag{A-1}$$

First of all, we express the position in terms of Cartesian coordinate on ENU (r_E, r_N, r_U) instead of geodetic coordinate (φ, λ, h). The position errors along east, north and up $(\delta r_E, \delta r_N, \delta r_U)$ can be written as

$$\begin{bmatrix} \delta r_E \\ \delta r_N \\ \delta r_U \end{bmatrix} = \begin{bmatrix} \delta\lambda(R_N + h)\cos\varphi \\ \delta\varphi(R_M + h) \\ \delta h \end{bmatrix} \tag{A-2}$$

If the error states are selected as

$$\delta\mathbf{x} = [\delta r_E \quad \delta r_N \quad \delta r_U \quad \delta v_E \quad \delta v_N \quad \delta v_U \quad \delta p \quad \delta r \quad \delta A$$

$$gb_x \quad gb_y \quad gb_z \quad ab_x \quad ab_y \quad ab_z \quad gsf_x \quad gsf_y \quad gsf_z \quad asf_x \quad asf_y \quad asf_z \quad \delta t \quad \delta\dot{t}]^T$$

We have non-zero elements in the F matrix as following:

$$\mathbf{F}(1,2) = \frac{V^E \tan\varphi}{R_N + h}; \qquad \mathbf{F}(1,3) = \frac{-V^E}{R_N + h}; \qquad \mathbf{F}(1,4) = 1$$

$$\mathbf{F}(2,1) = \frac{-V^E \tan\varphi}{R_N + h}; \qquad \mathbf{F}(2,3) = \frac{-V^N}{R_M + h}; \qquad \mathbf{F}(2,5) = 1$$

$$\mathbf{F}(3,1) = \frac{V^E}{R_N + h}; \qquad \mathbf{F}(3,2) = \frac{V^N}{R_M + h}; \qquad \mathbf{F}(3,6) = 1$$

$$\mathbf{F}(4,1) = \frac{g}{R_N + h}; \quad \mathbf{F}(4,5) = 2\omega_e \sin\varphi + \frac{V^E \tan\varphi}{R_N + h}; \quad \mathbf{F}(4,6) = -2\omega_e \cos\varphi - \frac{V^E}{R_N + h};$$

$$\mathbf{F}(4,8) = -f^U; \ \mathbf{F}(4,9) = f^N; \ \mathbf{F}(4,13) = \mathbf{R}_b^l(1,1); \ \mathbf{F}(4,14) = \mathbf{R}_b^l(1,2); \ \mathbf{F}(4,15) = \mathbf{R}_b^l(1,3);$$

$$\mathbf{F}(4,19) = \mathbf{R}_b^l(1,1) f_x; \ \mathbf{F}(4,20) = \mathbf{R}_b^l(1,2) f_y; \ \mathbf{F}(4,21) = \mathbf{R}_b^l(1,3) f_z$$

$$\mathbf{F}(5,2) = \frac{g}{R_M + h}; \quad \mathbf{F}(5,4) = -2\omega_e \sin\varphi - \frac{V^E \tan\varphi}{R_N + h}; \quad \mathbf{F}(5,6) = -\frac{V^N}{R_M + h};$$

$$\mathbf{F}(5,7) = f^U; \ \mathbf{F}(5,9) = -f^E; \ \mathbf{F}(5,13) = \mathbf{R}_b^l(2,1); \ \mathbf{F}(5,14) = \mathbf{R}_b^l(2,2); \ \mathbf{F}(5,15) = \mathbf{R}_b^l(3,3);$$

$$\mathbf{F}(5,19) = \mathbf{R}_b^l(2,1) f_x; \ \mathbf{F}(5,20) = \mathbf{R}_b^l(2,2) f_y; \ \mathbf{F}(5,21) = \mathbf{R}_b^l(2,3) f_z$$

$$\mathbf{F}(6,3) = \frac{2g}{R_N + h}; \quad \mathbf{F}(6,4) = 2\omega_e \cos\varphi + \frac{V^E}{R_N + h}; \quad \mathbf{F}(6,5) = \frac{V^N}{R_M + h};$$

$$\mathbf{F}(6,7) = -f^N; \ \mathbf{F}(6,8) = f^E; \ \mathbf{F}(6,13) = \mathbf{R}_b^l(3,1); \ \mathbf{F}(6,14) = \mathbf{R}_b^l(3,2); \ \mathbf{F}(6,15) = \mathbf{R}_b^l(3,3);$$

$$\mathbf{F}(6,19) = \mathbf{R}_b^l(3,1) f_x; \ \mathbf{F}(6,20) = \mathbf{R}_b^l(3,2) f_y; \ \mathbf{F}(6,21) = \mathbf{R}_b^l(3,3) f_z$$

$$\mathbf{F}(7,8) = \omega_e \sin\varphi + \frac{V^E \tan\varphi}{R_N + h}; \quad \mathbf{F}(7,9) = -\omega_e \cos\varphi - \frac{V^E}{R_N + h};$$

$$\mathbf{F}(7,10) = -\mathbf{R}_b^l(1,1); \ \mathbf{F}(7,11) = -\mathbf{R}_b^l(1,2); \ \mathbf{F}(7,12) = -\mathbf{R}_b^l(1,3);$$

$$\mathbf{F}(7,16) = -\mathbf{R}_b^l(1,1)\omega_x; \ \mathbf{F}(7,17) = -\mathbf{R}_b^l(1,2)\omega_y; \ \mathbf{F}(7,18) = -\mathbf{R}_b^l(1,3)\omega_z$$

$$\mathbf{F}(8,7) = -\omega_e \sin\varphi - \frac{V^E \tan\varphi}{R_N + h}; \quad \mathbf{F}(8,9) = -\frac{V^N}{R_M + h};$$

$$\mathbf{F}(8,10) = -\mathbf{R}_b^l(2,1); \ \mathbf{F}(8,11) = -\mathbf{R}_b^l(2,2); \ \mathbf{F}(8,12) = -\mathbf{R}_b^l(2,3);$$

$$\mathbf{F}(8,16) = -\mathbf{R}_b^l(2,1)\omega_x; \ \mathbf{F}(8,17) = -\mathbf{R}_b^l(2,2)\omega_y; \ \mathbf{F}(8,18) = -\mathbf{R}_b^l(3,3)\omega_z$$

$$\mathbf{F}(9,7) = \omega_e \cos\varphi + \frac{V^E}{R_N + h}; \quad \mathbf{F}(9,8) = \frac{V^N}{R_M + h};$$

$$\mathbf{F}(9,10) = -\mathbf{R}_b^l(3,1); \ \mathbf{F}(9,11) = -\mathbf{R}_b^l(3,2); \ \mathbf{F}(9,12) = -\mathbf{R}_b^l(3,3);$$

$$\mathbf{F}(9,16) = -\mathbf{R}_b^l(3,1)\omega_x; \ \mathbf{F}(9,17) = -\mathbf{R}_b^l(3,2)\omega_y; \ \mathbf{F}(9,18) = -\mathbf{R}_b^l(3,3)\omega_z$$

$\mathbf{F}(10,10) = -1/\beta_{gbx}$; $\mathbf{F}(11,11) = -1/\beta_{gby}$; $\mathbf{F}(12,12) = -1/\beta_{gbz}$;

$\mathbf{F}(13,13) = -1/\beta_{abx}$; $\mathbf{F}(14,14) = -1/\beta_{aby}$; $\mathbf{F}(15,15) = -1/\beta_{abz}$;

$\mathbf{F}(16,16) = -1/\beta_{gsfx}$; $\mathbf{F}(17,17) = -1/\beta_{gsfy}$; $\mathbf{F}(18,18) = -1/\beta_{gsfz}$;

$\mathbf{F}(19,19) = -1/\beta_{asfx}$; $\mathbf{F}(20,20) = -1/\beta_{asfy}$; $\mathbf{F}(21,21) = -1/\beta_{asfz}$;

$\mathbf{F}(22,23) = 1$.

where

φ is the latitude;

ω_{e} is Earth rotation rate;

R_m	is the meridian radius;
R_n	is the prime vertical radius;
g	is the normal gravity;
$[V^E \quad V^N \quad V^U]^T$	is the velocity vector along ENU;
$[f_x \quad f_y \quad f_z]^T$	is the accelerometer measurements on the body frame;
$[f^E \quad f^N \quad f^U]^T$	is the specific force on the LLF;
$[\omega_x \quad \omega_y \quad \omega_z]^T$	is the gyro measurements on the body frame;
$\mathbf{R}_b^l$	is the rotation matrix from body frame to the LLF;
β	is the correlation time in 1st order Gauss Markov model.

Appendix B

INS Direct Aiding – Second Simulation Example

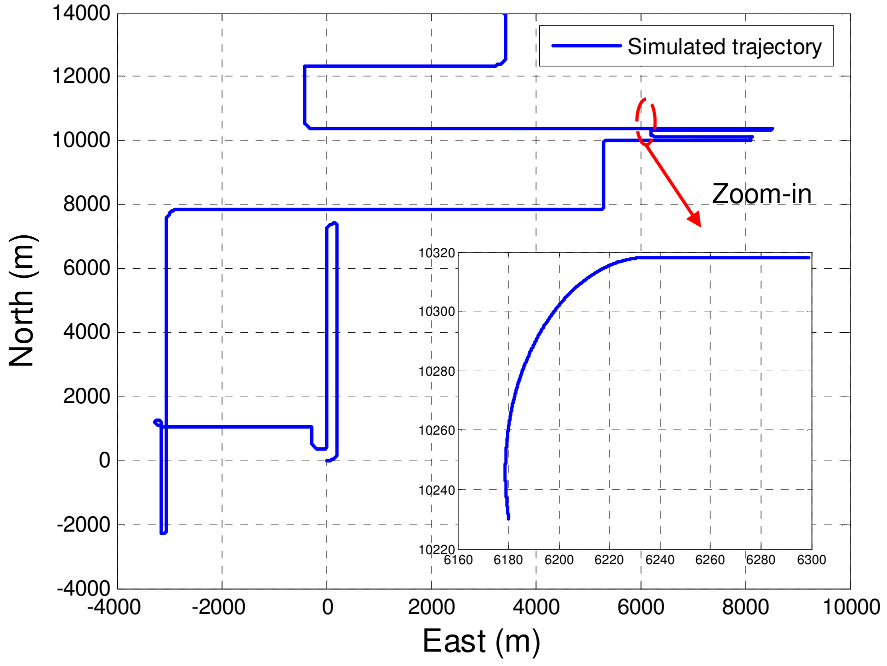

Figure B.1: Simulated trajectories and zoom-in 20s of interest

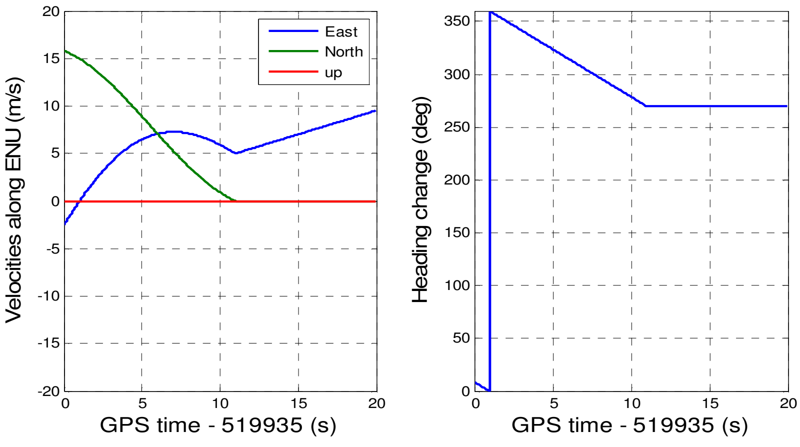

Figure B.2: Simulated velocities and heading of 20s

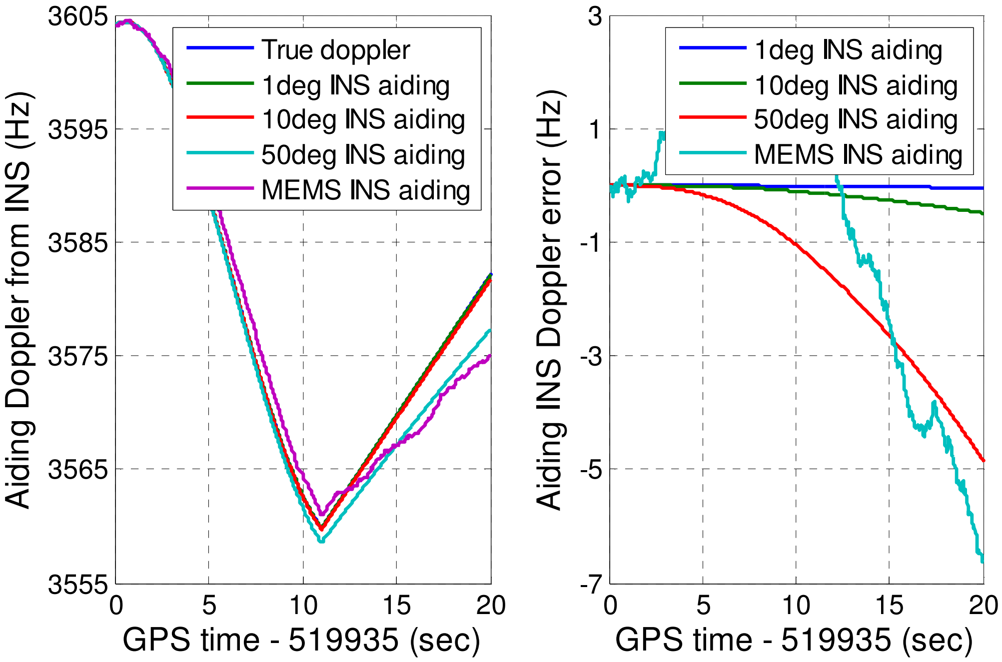

Figure B.3: Aiding Doppler and errors with different grade INSs

Table B.1: Tracking error with different grade INS aiding (PRN 5)

INS	Tracking errors $(1-\sigma)$		Lock status
	Doppler (Hz)	Phase (deg)	
1 deg/hr	1.94	8.1	Yes
10 deg/hr	1.95	8.6	Yes
50 deg/hr	-	-	No
MEMS based INS	--	--	No

Appendix C

Performance Test of EKF based IPLL – Second Data Period

Similar to the previous method, 20 seconds trajectory and motions of interest are selected to analyze the IPLL thoroughly. Figure C.1 (a) and (b) show the 20s zoom-in trajectories and C/N_0 of interest (523000s to 523020s). The maximum acceleration is $1.6m/s^2$ during this period.

Given that C/N_0 of PRN 5 is degraded to $26dB-Hz$. Figure C.2 gives the lock detector output of a conventional receiver PLL. It is obvious that the PLL loses the lock of the carrier frequency.

Figure C.3 shows the aiding Doppler at 100Hz from the 1G2A ADI MEMS INS/GPS integration including both the INS Doppler estimate and the clock drift estimate for the IPLL in the Channel 4 of the receiver, where the PRN 5 was being tracked.

By using the above adding Doppler information, Figure C.4 (a) and (b) show the outputs of the IPLL discriminator and the loop filter, respectively. Figure 5.15 (a) and (b) show the IPLL lock detector output and the corresponding estimation of C/N_0.

Figure C.6 compares the lock detector outputs with different signal strength (but with the same loop bandwidth $9Hz$). It indicates that, with Doppler aiding clock, an additional $3dB-Hz$ margin can be achieved, allowing signals with power as low as $24dB-Hz$.

Figure C.7 compares the positioning errors between tight integration with PLL and that with IPLL. The comparison takes place under weak signal environment, e.g. $C/N_0 = 26dB-Hz$, of which two satellites suffer (PRN 5 and PRN 30) loss in the conventional PLL while IPLL locks them.

During this 20s of interest, the vehicle traveled $220m$. The position error is reduced from $< 4\%$ of the travel distances ($8m$) to $< 2\%$ of the travel distances ($4m$), which is 50% improvement.

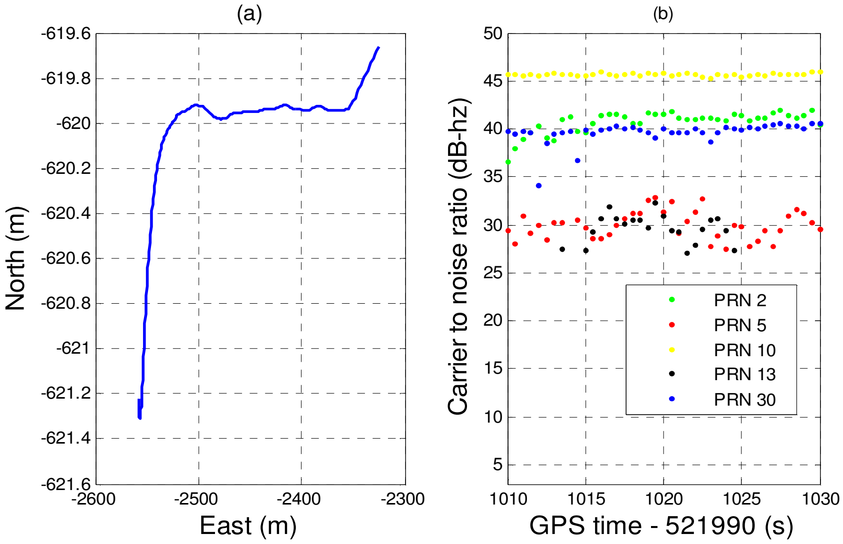

Figure C.1: 20s trajectories and signal strength of interest

Figure C.2: Lock detector output of conventional PLL with $C/N_0 = 26dB - Hz$

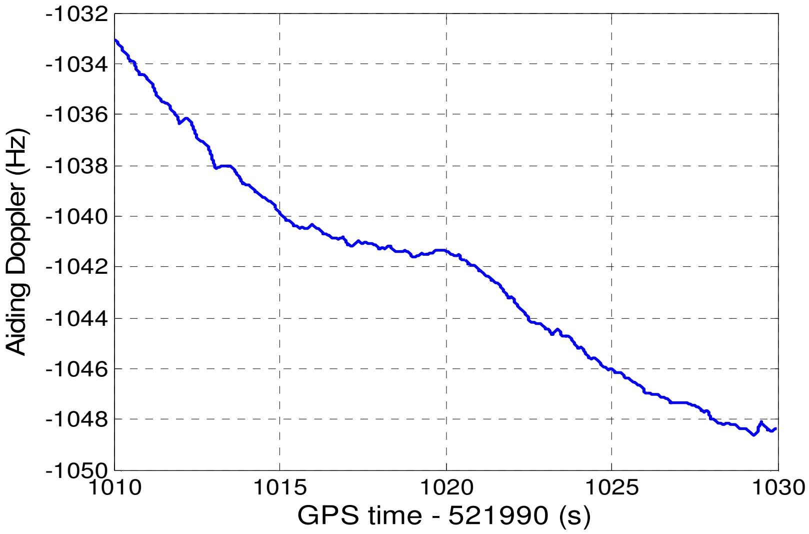

Figure C.3: Aiding Doppler to IPLL

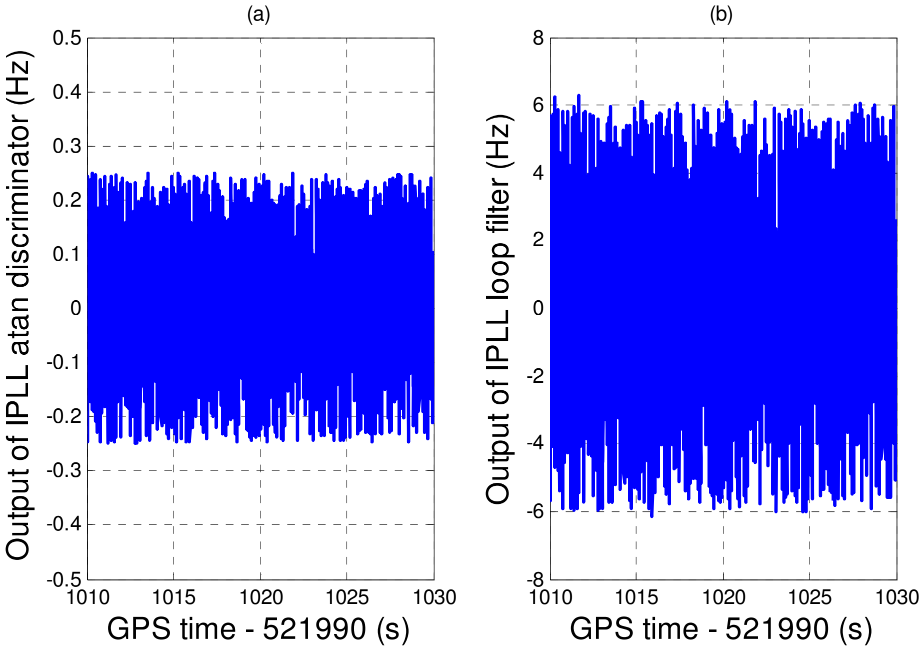

Figure C.4: Outputs of IPLL discriminator and loop filter

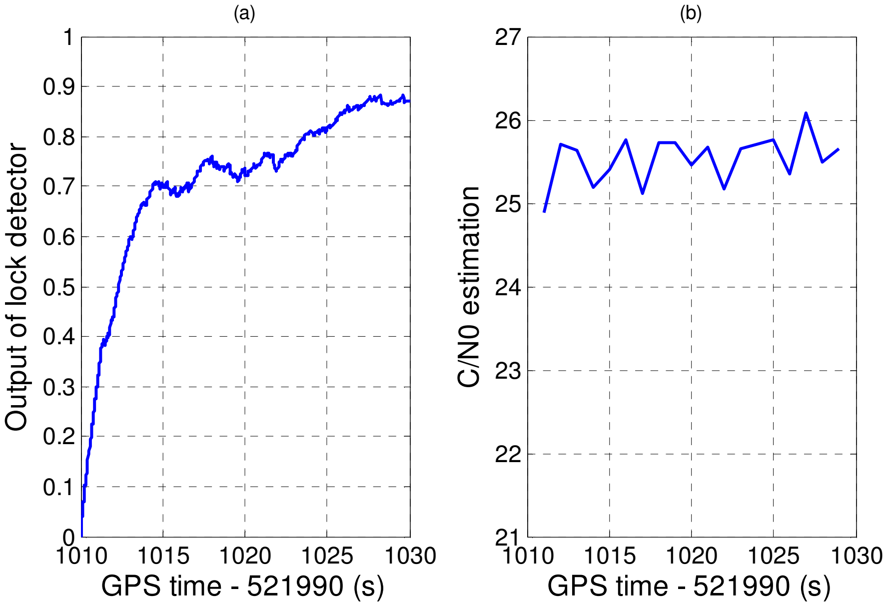

Figure C.5: Lock detector output and C/N_0 estimation from IPLL

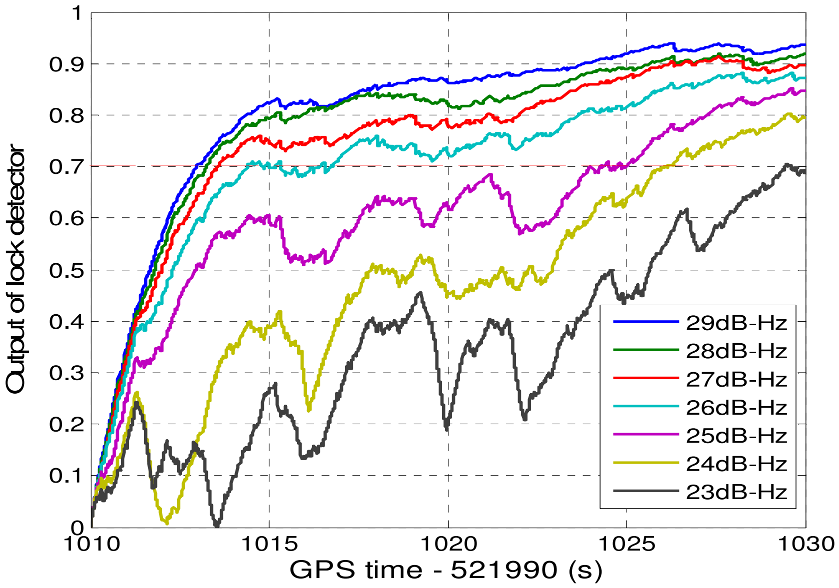

Figure C.6: Output of IPLL lock detector vs. different signal strength

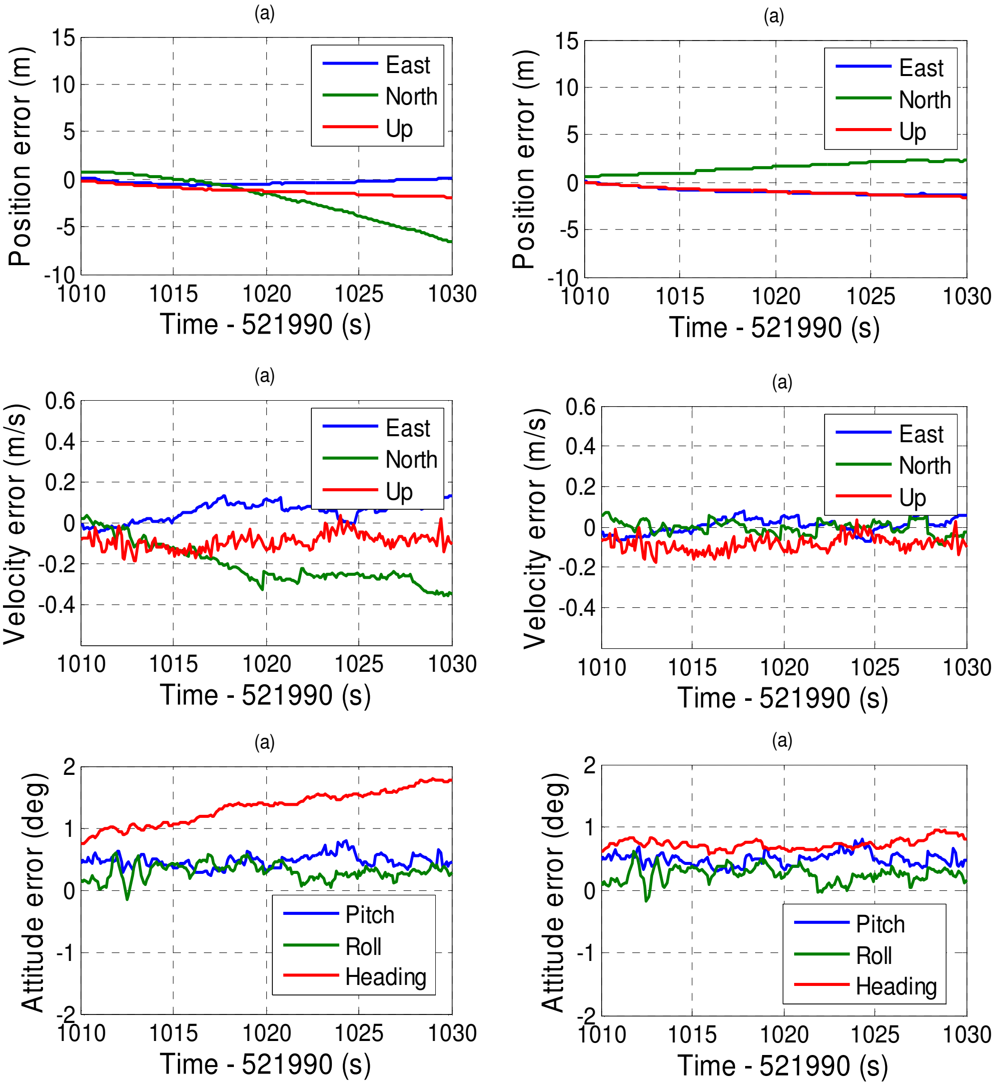

Figure C.7: Comparison of navigation errors by using PLL and IPLL